

Copyright

by

Insun Jo

2012

**The Dissertation Committee for Insun Jo Certifies that this is the approved version  
of the following dissertation:**

**Experimental Investigation of Thermal Transport in  
Graphene and Hexagonal Boron Nitride**

**Committee:**

---

Zhen Yao, Co-Supervisor

---

Li Shi, Co-Supervisor

---

Chih-Kang Shih

---

Allan H. MacDonald

---

Maxim Tsoi

**Experimental Investigation of Thermal Transport in  
Graphene and Hexagonal Boron Nitride**

**by**

**Insun Jo, B. S.**

**Dissertation**

Presented to the Faculty of the Graduate School of

The University of Texas at Austin

in Partial Fulfillment

of the Requirements

for the Degree of

**Doctor of Philosophy**

**The University of Texas at Austin**

**December, 2012**

**Dedicated to my parents**

## Acknowledgements

The works presented here would not have been possible without contributions from many collaborators. I want to express sincere appreciation to my co-supervisors Profs. Zhen Yao and Li Shi for their support and insightful guidance while I pursued my Ph.D. Their visions and experiences on nanostructures and devices have driven me to explore this research area with joy. I would like to thank my dissertation committee, Profs. Chih-Kang Shih, Allan MacDonald, and Maxim Tsoi, for helpful guidance and inspiration. I have been very grateful to meet many collaborators with great abilities. In particular, I have been working closely with Michael T. Pettes, Jae Hun Seol, Yong J. Lee, Mir Mohamed Sadeghi from our group. I also would like to thank Suyong Jung and Kang Luo for helping me in the early stage of my research. I would like to give special thanks to Seyoung Kim, a close friend of mine and a great researcher. We have developed experimental skills and had fruitful discussions that helped explore the relatively new material, graphene. I would like to thank Profs. Emanuel Tutuc, Sanjay Banerjee, and Stephen Cronin for their support and advice. I have been constantly inspired by attending Prof. MacDonald's group meetings; discussions with theorists have been a driving force and helped me widen my horizon, and we are also close friends: Jeil Jung, Guru Khalsa, Rohit Hegde, and Inti Sodemann.

For the past six and half years in Austin, I have met many great individuals who directly or indirectly helped me to achieve my Ph.D. I would like to thank close friends of mine for giving me strong support and good memories: Austin Yi, Yongsup Ihn, Jusang Yang, Miri Choi, Woosuk Bang, Hyojung Kim, Hyungdo Nam, and Donghoon Kuk. I

would also like to thank Heidi Seinige and Cheng Wang for the support in and outside the office.

A special thanks for useful comments on my dissertation draft goes to Austin Yi, Dan Sellan, and Annie Weathers.

Lastly, I would like to mention my soccer and softball teams to thank the people I met and built friendships with: Red Devils, PAMA, and Austin Blues.

# **Experimental Investigation of Thermal Transport in Graphene and Hexagonal Boron Nitride**

Insun Jo, Ph. D.

The University of Texas at Austin, 2012

Supervisors: Zhen Yao and Li Shi

Two-dimensional graphene, a single layer of graphite, has emerged as an excellent candidate for future electronic material due to its unique electronic structure and remarkably high carrier mobility. Even higher carrier mobility has been demonstrated in graphene devices using hexagonal boron nitride as an underlying dielectric support instead of silicon oxide. Interestingly, both graphene and boron nitride exhibit superior thermal properties, therefore may potentially offer a solution to the increasingly severe heat dissipation problem in nanoelectronics caused by increased power density. In this thesis, we focus on the investigation of the thermal properties of graphene and hexagonal boron nitride.

First, scanning thermal microscopy based on a sub-micrometer thermocouple at the apex of a microfabricated tip was employed to image the temperature profiles in electrically biased graphene devices with  $\sim 100$  nm scale spatial resolution. Non-uniform temperature distribution in the devices was observed, and the “hot spot” locations were correlated with the charge concentrations in the channel, which could be controlled by both gate and drain-source biases. Hybrid contact and lift mode scanning has enabled us to obtain the quantitative temperature profiles, which were compared with the profiles obtained from Raman-based thermometry. The temperature rise in the channel provided

an important insight into the heat dissipation mechanism in Joule-heated graphene devices.

Next, thermal conductivity of suspended single and few-layer graphene was measured using a micro-bridge device with built-in resistance thermometers. Polymer-assisted transfer technique was developed to suspend graphene layers on the pre-fabricated device. The room temperature thermal conductivity values of 1-7 layer graphene were measured to be lower than that of bulk graphite, and the value appeared to increase with increasing sample thickness. These observations can be explained by the impact of the phonon scattering by polymer residue remaining on the sample surfaces.

Lastly, thermal conductivity of few-layer hexagonal boron nitride sample was measured by using the same device and technique used for suspended graphene. Measurements on samples with different suspended lengths but similar thickness allowed us to extract the intrinsic thermal conductivity of the samples as well as the contribution of contact thermal resistance to the overall thermal measurement. The room temperature thermal conductivity of 11 layer sample approaches the basal-plane value reported in the bulk sample. Lower thermal conductivity was measured in a 5 layer sample than an 11 layer sample, which again supports the polymer effect on the thermal transport in few-layer hexagonal boron nitride.

## Table of Contents

List of Tables .....	xii
List of Figures .....	xiii
Chapter 1. Introduction .....	1
1.1 Background .....	1
1.2 Crystal structure : graphene and hexagonal boron nitride .....	5
1.3 Electronic structure .....	7
1.4 Phonon dispersion .....	8
1.5 Thermal conductivity .....	11
1.6 Outline of the thesis .....	13
References .....	14
Chapter 2. Experimental Techniques .....	18
2.1 Scotch tape method .....	18
2.2 Sample characterization methods .....	20
2.2.1 Atomic force microscopy .....	20
2.2.2 Raman spectroscopy .....	21
2.2.3 Transmission electron microscopy .....	24
2.2.4 Electrical transport measurement .....	25
2.3 Transfer technique .....	28
2.4 Summary .....	30
References .....	32
Chapter 3. Scanning Thermal Microscopy Measurement on Graphene Devices ..	37
3.1 Introduction .....	37
3.2 Scanning thermal microscopy .....	39
3.3 Sample preparation and experimental set-up .....	41
3.3.1 Graphene sample preparation .....	41
3.3.2 SThM set-up .....	42
3.4 Results .....	43

3.5 summary.....	52
References.....	54
Chapter 4. Thermal Conductivity Measurements of Suspended Graphene.....	57
4.1 Introduction.....	57
4.2 Sample preparation.....	58
4.3 Thermal measurement method.....	61
4.4 Results.....	65
4.5 Discussion.....	76
4.6 Summary.....	77
References.....	79
Chapter 5. Thermal Conductivity Measurements of Suspended Hexagonal Boron Nitride.....	82
5.1 Introduction.....	82
5.2 Sample preparation and characterization.....	83
5.3 Results.....	88
5.4 Summary.....	94
References.....	96
Chapter 6. Summary and Outlook.....	99
6.1 Summary.....	99
6.2 Outlook.....	100
References.....	105
Appendices.....	106
Appendix A. Temperature Calibration and Finite Element Method.....	107
A.1 Contact Mode and Lift Mode SThM.....	107
A.2 Finite element method.....	112
References.....	116

Appendix B. Gate Stress Effect .....	117
Appendix C. Thermal Conductivity Modeling .....	119
References .....	122
Appendix D. Thermal Contact Conductance .....	123
References .....	125
Bibliography .....	126

## List of Tables

**Table 5.1** Dimension of the suspended h-BN samples measured in this work. .87

## List of Figures

<b>Figure 1. 1</b>	Two dimensional crystals exfoliated on a silicon substrate .....	4
<b>Figure 1. 2</b>	Crystal structures of graphite and h-BN.....	6
<b>Figure 1. 3</b>	Electronic band structure of graphene .....	7
<b>Figure 1. 4</b>	Phonon dispersion of graphite and single layer graphene .....	10
<b>Figure 1. 5</b>	Phonon dispersion of bulk and single layer h-BN .....	10
<b>Figure 2. 1</b>	Scotch tape method.....	19
<b>Figure 2. 2</b>	Application of AFM for graphene device characterization .....	20
<b>Figure 2. 3</b>	Raman spectra of single, bi-, and 7- layer graphene showing Raman active G and 2D mode peaks.....	23
<b>Figure 2. 4</b>	TEM images and diffraction patterns of suspended few-layer h-BN.....	25
<b>Figure 2. 5</b>	Electrical transport properties of graphene.....	26
<b>Figure 2. 6</b>	Schematic diagram of the transfer process using a PMMA support.....	29
<b>Figure 3. 1</b>	SEM micrograph of a SThM tip and the heat transfer mechanism in SThM .....	40
<b>Figure 3. 2</b>	Optical micrograph of a graphene device and the temperature calibration of the thermometer line.....	42
<b>Figure 3. 3</b>	Schematic diagram of the instrumental set-up .....	43
<b>Figure 3. 4</b>	Thermal mapping of Device 1 and Device 2 .....	45
<b>Figure 3. 5</b>	Comparison of temperatures determined from SThM and Raman measurement.....	51
<b>Figure 4. 1</b>	Transfer of exfoliated graphene onto a micro-bridge device .....	60

<b>Figure 4. 2</b>	Heat conduction diagram in a suspended device and the thermal measurement data.....	62
<b>Figure 4. 3</b>	SEM images of two suspended graphene samples measured with micro-bridge devices.....	67
<b>Figure 4. 4</b>	TEM images of 7-layer graphene.....	68
<b>Figure 4. 5</b>	Seebeck coefficient and electrical conductivity measured in bilayer graphene.....	69
<b>Figure 4. 6</b>	Measured thermal conductance of suspended graphene.....	70
<b>Figure 4. 7</b>	Measured $\kappa$ of bi- and 7-layer suspended graphene. ....	72
<b>Figure 4. 8</b>	Room temperature $\kappa$ values as a function of layer thickness.. ....	75
<b>Figure 5. 1</b>	Transfer of exfoliated few-layer h-BN onto a micro-bridge device .....	85
<b>Figure 5. 2</b>	TEM images of suspended h-BN samples.....	87
<b>Figure 5. 3</b>	Measured thermal conductance values of four h-BN samples, sample geometry, and $R_s W$ product versus the $L/t$ plot. ....	90
<b>Figure 5. 4</b>	Thermal conductivity values of the two 7.5 $\mu\text{m}$ long, 11 and 5 layer thick suspended h-BN samples .....	91
<b>Figure A.1</b>	Thermovoltage response of SThM probe .....	108
<b>Figure A. 2</b>	Contact-mode and lift-mode thermovoltage profiles.....	111
<b>Figure A. 3</b>	FEM simulation results.....	115
<b>Figure B. 1</b>	$R$ vs $V_g$ measurement showing a gate stress effect.....	118
<b>Figure C. 1</b>	Phonon dispersion of bulk h-BN along the high symmetric direction connecting between $\Gamma$ and M.....	119
<b>Figure C. 2</b>	Comparison between the experimental thermal conductivity and calculation results for different $l_b$ values.....	121

**Figure D. 1** The obtained thermal interface conductance between the  
h-BN sample and the micro-bridge device. ....124

# Chapter 1. Introduction

## 1.1 BACKGROUND

Graphene, a two-dimensional monolayer of carbon atoms arranged in a honeycomb lattice, is the building block for other graphitic materials including one-dimensional carbon nanotubes and three-dimensional graphite. It has been theoretically investigated for more than sixty years. For example, Wallace<sup>1</sup> calculated the electronic band structure of graphene using a tight-binding method in 1947, revealing its semi-metallic nature and linear energy dispersion around the Fermi energy. Until recently, however, graphene remained a conceptual curiosity. In 2004,<sup>2</sup> Geim and Novoselov of Manchester University demonstrated that graphene could be isolated by using a remarkably simple mechanical exfoliation technique, which is commonly called the Scotch tape method. A single-layer of graphene could be identified in an optical microscope due to optical interference when they are exfoliated on a silicon substrate covered by silicon oxide of suitable thickness. An example is shown in Fig. 1 (a). Geim and Novoselov showed that graphene devices exhibit ambipolar field-effect transistor behavior, consistent with the semi-metallic nature of graphene. In 2005, the Manchester group<sup>3</sup> and Philip Kim's group<sup>4</sup> at Columbia University independently observed the quantum Hall effect in graphene. The quantum Hall plateaus were found to be quantized in half-integer values which provided convincing evidence of the two-dimensional massless chiral nature of charge carriers in this system. These early discoveries have

initiated intense research activities worldwide on graphene and other two-dimensional materials.

The exploding interests in graphene have been largely motivated by its remarkable electronic properties. Due to the linear energy dispersion around the Fermi energy, the low-energy charge carriers in graphene are described by relativistic Dirac equation rather than the Schrodinger equation. Additionally, the two carbon sublattices in the honeycomb lattice introduce a new degree of freedom, pseudospin, which is associated with the hopping of electrons between the two sublattices. Because of the pseudospin nature which suppresses the backscattering, the charge carriers in graphene are reported to have a high mobility  $\sim 10,000 \text{ cm}^2\text{V}^{-1}\text{s}^{-1}$  in  $\text{SiO}_2$  supported graphene<sup>5</sup> and about  $\sim 200,000 \text{ cm}^2\text{V}^{-1}\text{s}^{-1}$  in suspended graphene.<sup>6</sup> Because of the gapless nature of monolayer graphene, field-effect transistors based on graphene do not show large on-off ratio. Thus graphene cannot be used directly for logic devices. However, the high mobility of charge carriers and the ambipolar transport characteristics make graphene particularly promising for high frequency analog applications. It was demonstrated by Lin et al.<sup>7</sup> that high frequency operation, at 100 GHz, was possible in graphene-based analog transistors. In order to realize graphene's full potential as a post-silicon electronic material, a sizable bandgap larger than 0.5 eV must be created.<sup>8</sup> Although a small bandgap can be engineered in nano-ribbons and bilayer graphene under strong electric field, a sufficiently large gap has not been created at this stage.

Mechanical properties of graphene are also extraordinary due to the strong carbon-carbon covalent bonds. The tensile strength of graphene is measured to be 130

GPa,<sup>9</sup> which is about 300 times greater than steel. In addition, graphene can sustain a large degree of stretching and bending without structural damage. These properties together with the optical transparency make graphene very attractive in potential applications in solar cells, touch screen displays, and flexible optoelectronic devices.

A major focus of our research is on the thermal transport properties in graphene. Graphene is expected to have high thermal conductivity, which makes it promising for applications in nanoelectronics and thermal management. The thermal conductivity of mechanically-exfoliated and suspended graphene was first measured by Balandin et al.<sup>10</sup> with the use of Raman-based thermometry. The room temperature value was found to be  $\sim 5000 \text{ Wm}^{-1}\text{K}^{-1}$ , higher than the highest value reported for carbon nanotubes,  $3500 \text{ Wm}^{-1}\text{K}^{-1}$ . Subsequent work by Cai et al.<sup>11</sup> measured a value  $2500 +1100/-1050 \text{ Wm}^{-1}\text{K}^{-1}$  at 350 K in graphene grown by the chemical vapor deposition method. Seol et al.<sup>12</sup> developed a micro-thermometer device that measured the thermal conductivity of a single layer graphene supported on  $\text{SiO}_2$  over a wide temperature range. A room temperature value  $\sim 600 \text{ Wm}^{-1}\text{K}^{-1}$  was obtained. This is significantly lower than that of suspended graphene, but still higher than that of copper,  $\sim 400 \text{ Wm}^{-1}\text{K}^{-1}$ . The suppression was attributed to phonon scattering by the underlying substrate. The work presented in this thesis is primarily focused on the thermal transport measurements of suspended graphene using a microfabricated bridge structure and the results will be presented in Chapter 4.

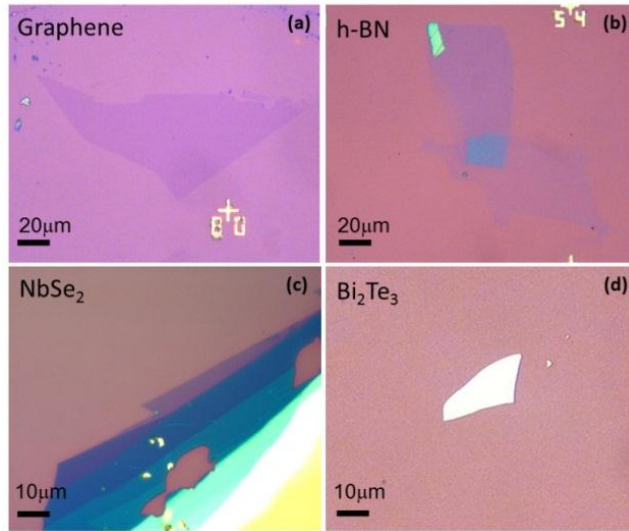


**Figure 1. 1** Two dimensional crystals exfoliated on a silicon substrate (a) Single-layer graphene, (b) Few-layer h-BN, (c) NbSe<sub>2</sub> and (d) Bi<sub>2</sub>Te<sub>3</sub> nanoplate.

Hexagonal boron nitride (h-BN) [shown in Fig. 1.1 (b)] has recently emerged as an excellent dielectric support for graphene-based devices. When used as a substrate, few-layer h-BN provides a clean and flat surface for graphene channel, thus ultrahigh electron mobility comparable to that of suspended graphene, has been achieved. Moreover, compared with other commonly used thin-film dielectric materials, few-layer h-BN offers the additional advantages of high thermal conductivity<sup>13</sup> and mechanical strength.<sup>14</sup> In particular, thermal conductivity of bulk h-BN was measured to be about two orders of magnitude higher than that of the current-generation dielectric material, SiO<sub>2</sub>. We have conducted the first thermal-conductivity measurements of few-layer h-BN and the results are presented in Chapter 5.

The mechanical exfoliation technique has also enabled the study of other two-dimensional materials. Figure 1.1 (c) shows a few-layer NbSe<sub>2</sub> sample. Bulk NbSe<sub>2</sub> has a superconducting transition temperature  $\sim 7.2$  K. It would be interesting to investigate the effect of reduced thickness on the superconducting properties similar to a recent study conducted in few-layer Pb films.<sup>15</sup> Lastly, Fig. 1.1 (d) shows a few-layer Bi<sub>2</sub>Te<sub>3</sub>. Traditionally a semiconducting thermoelectric material, this material has recently attracted great attention as it has been identified as a topological insulator exhibiting interesting conducting surface states with an insulating bulk. As the thickness decreases, the surface states of Bi<sub>2</sub>Te<sub>3</sub> dominate the transport, allowing one to investigate the properties of the topologically protected surface states.<sup>16, 17</sup> In addition to the examples shown here, there are many materials with layered structures and diverse properties that can be prepared in two-dimensional form by the exfoliation technique, thus we believe that many opportunities exist for future research.

In the following, we first discuss the crystal structures of graphene and h-BN, two materials studied in this thesis. Electronic and phonon structures are discussed as well as the calculation of thermal conductivity from the phonon dispersion in ideal samples.

## **1.2 CRYSTAL STRUCTURE : GRAPHENE AND HEXAGONAL BORON NITRIDE**

Graphite and bulk h-BN have a very similar crystal structure as shown in Fig. 1.2. Two-dimensional graphene layers are bound via weak Van der Waals force along the out-of-plane direction, while covalent bonds allow in-plane atoms to strongly interact. Different stacking orders along the vertical direction are observed. In graphite, ABA or

Bernal stacking is more abundant than others such as turbostratic and ABC stacking. In h-BN, AAA stacking where boron and nitrogen atoms are stacked alternatively, is dominant as it is more stable than others. Due to the layered structure, the physical properties in both bulk materials are highly anisotropic. For example, basal-plane thermal conductivity in bulk graphite<sup>18</sup> and h-BN<sup>19</sup> is measured to be about 600 and 200 times larger than out-of-plane thermal conductivity, respectively.

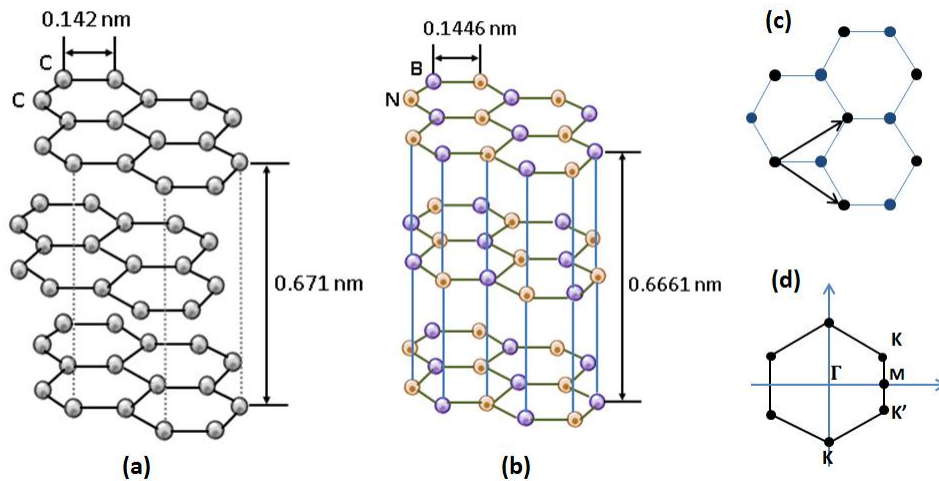


**Figure 1. 2** Crystal structure of graphite and h-BN (a) Graphene layers are stacked ABA order, although other phases are also observed. (b) AAA stacking in h-BN. (c) Single-layer crystal structure. (d) First Brillouin zone.

Single layer crystal structure is shown in Fig. 1.2 (c). The two translational vectors are indicated by arrows. There are two atoms in a unit cell in graphene and h-BN. The first Brillouin zone is depicted in Fig. 1.2 (d), where high symmetry points are denoted.

### 1.3 ELECTRONIC STRUCTURE

Carbon atoms in graphene form strong covalent bonds by hybridized  $sp^2$  orbitals in a honeycomb lattice structure, while one  $p_z$  orbital per carbon atom is delocalized. The electronic properties of graphene are determined by these delocalized  $p_z$  orbital electrons. Analytic tight-binding calculations have been used to obtain the band structure of graphene as shown in Fig. 1.3.

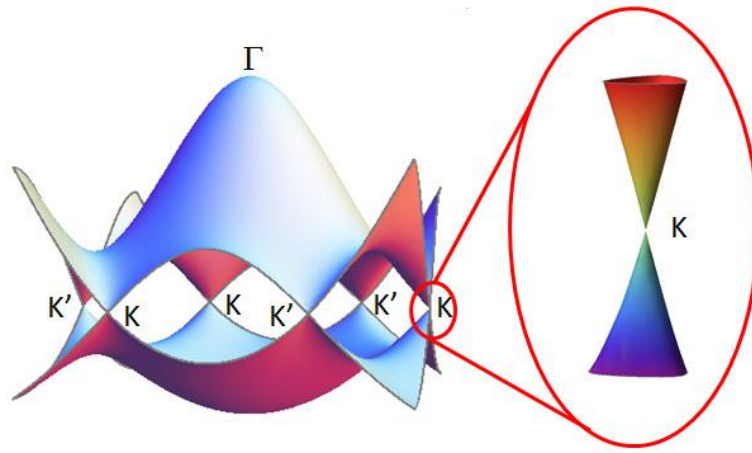


**Figure 1. 3** Electronic band structure of graphene. 2D linear dispersion at the K point is shown in the zoomed-in oval.<sup>20</sup>

Interestingly, the energies of charge carriers on the 2D Fermi surface, located near the degenerate K and K' points, show a linear dispersion:

$$E_{\pm}(k) = \pm\hbar v_F k \quad (1.1)$$

where  $\hbar$  is the reduced Plank constant,  $v_F$  is the Fermi velocity ( $=1 \times 10^6 \text{ ms}^{-1}$ ).

Electron-hole symmetry is shown in the zoomed-in oval, where upper cone is the conduction band and the bottom cone is the valence band. When the two cones meet,

which is called the Dirac point, the charge carriers in the graphene channel is minimum, resulting in maximum resistivity. Electric field exerted by a gate can change the Fermi energy ( $E_F$ ) and tune the polarity and density of charge carriers in graphene according to

$$E_F = \pm \hbar v_F \sqrt{\pi n}, \quad (1.2)$$

thus ambipolar transport characteristics are observed.

Because of the many interesting electronic properties of single and few-layer graphene, a vast number of experiments and theoretical studies have been done on these systems. Some excellent reviews can be found in Refs 21-22.

In h-BN, breaking of sublattice symmetry by dissimilar atoms of boron and nitrogen opens up a bandgap. *ab initio* calculations<sup>23-25</sup> show that h-BN have a wide bandgap of 5-6 eV. Ultraviolet luminescence has been observed in h-BN due to its direct bandgap. Thus this material holds promise in optoelectronic applications.<sup>25</sup>

#### 1.4 PHONON DISPERSION

In single layer graphene and h-BN, two atoms in a unit cell yield 3 acoustic and 3 optical phonon modes. In comparison, bulk materials with a unit cell composed of 2 layer crystals exhibit 3 acoustic and 9 optical phonon modes. Phonon dispersion in two dimensional graphene and h-BN can be calculated using Density Functional Perturbation Theory. The *ab initio* calculation package Quantum ESPRESSO is used.<sup>26</sup> For the calculation, pseudo-potentials based on local density approximation replaced the core electrons, and the valence electrons were expanded in a number of plane waves with an energy cutoff of 70 a.u. These plane waves were used as a basis set in the self-consistent

calculations. The lattice constants used in calculation for bulk graphite are  $a = 2.458 \text{ \AA}$  and  $c = 6.701 \text{ \AA}$ . while  $a = 2.479 \text{ \AA}$  and  $c = 6.995 \text{ \AA}$  are taken for h-BN. The calculation was performed on an  $8 \times 8 \times 4$   $k$ -point grid in the Brillouin zone, and the calculations for the soft ZA phonon mode could not be converged if the sampling was coarser.

Figures 1.4 (a) and 1.5 (a) show the phonon dispersion in bulk graphite and h-BN while Figs 1.4 (b) and 1.5 (b) are results for single layer graphene and h-BN, respectively. Experimental data using electron energy loss spectroscopy<sup>27</sup>, inelastic X-ray scattering<sup>28-30</sup>, Raman<sup>31-33</sup>, and Infrared<sup>31</sup> spectroscopy are also depicted as blue (graphite) and red (h-BN) circles, which show excellent agreement with our calculation results.

As shown in Fig. 1.4 (b), 2D graphene has three acoustic phonon modes, LA, TA and ZA. The out-of-plane vibrational mode, ZA phonon mode, shows quadratic dispersion in contrast to linear dispersion in LA and TA phonons at low frequencies. In addition, the interlayer coupling in bulk graphite introduced a splitting of the low-energy phonons near the  $\Gamma$  point. The splitting corresponds to the in and out-of-phase vibrational modes of adjacent layers. Similar features in h-BN are observed in Fig. 1.5.

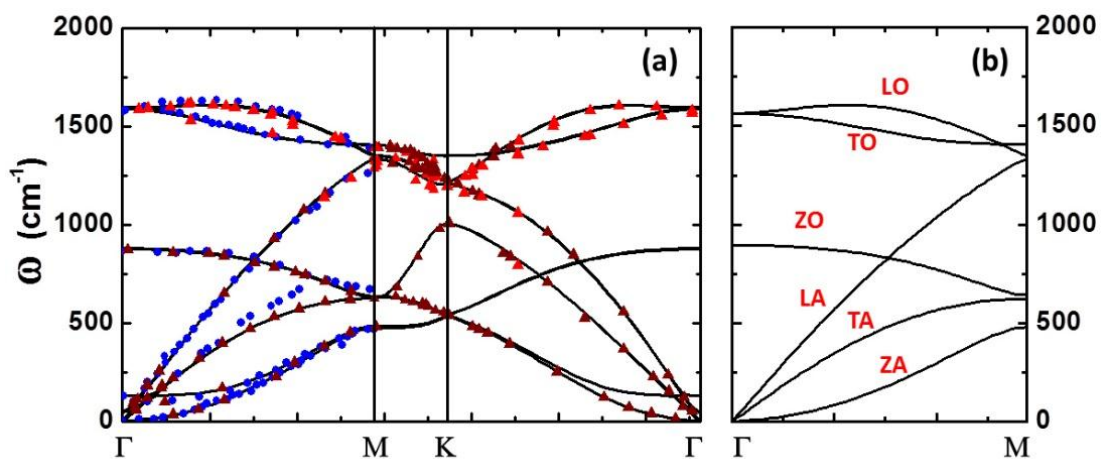


**Figure 1. 4** Phonon dispersion in graphite (a) and single layer graphene (b). Experimental data reported by electron energy loss spectroscopy<sup>27</sup> (blue circles), inelastic X-ray scattering (red<sup>28</sup> and brown<sup>29</sup> triangles) measurements.

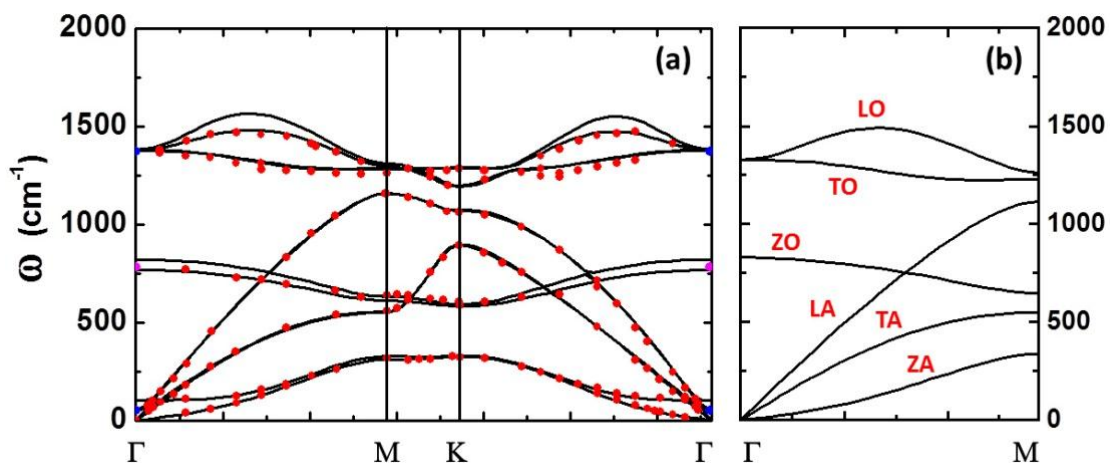


**Figure 1. 5** Phonon dispersion in bulk (a) and single layer (b) h-BN. Experimental data reported by inelastic X-ray scattering<sup>30</sup> (red circle), Raman spectroscopy<sup>31-33</sup> (blue circle), and Infrared spectroscopy<sup>31</sup> (magenta circle) measurements.

## 1.5 THERMAL CONDUCTIVITY

In general, thermal conductivity consists of lattice contribution and electron contribution. Electron thermal conductivity ( $\kappa_e$ ) can be estimated from the Wiedemann-Franz law in metals, which relates  $\kappa_e$  and the electrical conductivity  $\sigma$  according to

$$\frac{\kappa_e}{\sigma T} \approx L_0 \quad (1.3)$$

where  $L_0 = 2.44 \times 10^{-8} \text{ V}^2 \text{ K}^{-2}$  is called Lorenz number.

Note that  $L_0$  can vary with the carrier density and the type of electron scattering mechanism in semiconductors. While  $\kappa_e$  dominates the thermal conductivity in metals, its contribution in graphene is negligible because of the low carrier density. Lattice thermal conductivity ( $\kappa_l$ ) represents heat transport by the lattice vibrations, or phonons. In the kinetic theory under the Gray approximation,  $\kappa_l$  in  $d$  dimensional material in the diffusive regime is expressed as

$$\kappa_l = \frac{1}{d} C v l \quad (1.4)$$

where  $C$  is the lattice specific heat,  $v$  is the phonon group velocity, and  $l$  is the phonon mean free path, respectively.

The temperature dependence of  $\kappa_l$  and  $C$  are important as they reflect the intrinsic phonon properties. In  $d$  dimensions, phonon mode with a dispersion  $\omega \propto k^\alpha$  gives rise to  $C \propto T^{d/\alpha}$ .<sup>34</sup> At low temperatures ( $T \leq 50\text{K}$ ), the soft ZA phonon modes are predominantly populated due to their large density of states,<sup>35</sup> thus the specific heat of 2D graphene is expected to be dominated by the ZA modes and shows a linear temperature

dependence. When temperature increases further, most ZA phonons are occupied, while LA and TA phonons are being filled up. Hence, the temperature dependence of  $C$  changes to  $T^2$ . In suspended 2D graphene, where ZA phonons are dominant at low temperatures,  $\kappa_l$  is expected to show  $T^{1.5}$  dependence in the ballistic limit or when mean free path is constant.<sup>12, 36</sup> In comparison, for bulk graphite, the temperature dependence of  $C$  shows a  $T^3$  behavior at very low temperature ( $T \leq 10\text{K}$ ), then make transition to a  $T^2$  behavior because out-of-plane mode phonons are occupied quickly. Thus, in the intermediate temperature range (10-100K), where LA and TA phonons are being populated, the  $T^2$  dependence of  $C$  together with constant  $v$  of LA and TA phonons results in  $\kappa_l \propto T^{2.37}$ . At very high temperatures,  $\kappa_l$  is dominated by phonon-phonon scattering in both graphene and bulk graphite. This is an anharmonic 3-phonon scattering process which results in  $\kappa_l \sim T^{-1}$ . Hence low temperature thermal conductivity data are important in order to understand the intrinsic phonon transport properties associated with the dimensionalities.

In real samples,  $\kappa_l$  is often affected by edge and defect scattering. In particular, the isotope defect in h-BN is considerable due to the composition of 19.9%  $\text{B}^{10}$  and 80.1%  $\text{B}^{11}$ . In graphite, on the other hand, the isotope composition is 98.9%  $^{12}\text{C}$  and 1.1%  $^{13}\text{C}$ . The effect of isotope defect has been observed in graphene<sup>38</sup> and h-BN nanotubes<sup>39</sup>, where  $\kappa_l$  in isotopically enriched sample increased significantly. In our work, we have also found that the thermal conductivity can be strongly suppressed by the underlying support and by the polymer residues on the sample surfaces.

## **1.6 OUTLINE OF THE THESIS**

The remaining thesis is organized as follows. Experimental techniques to create and characterize graphene and h-BN are described in Chapter 2. In Chapter 3, scanning thermal microscopy is applied to investigate the temperature distribution in Joule-heated graphene devices. These temperature profiles are compared with Raman-based thermometry results. Chapter 4 presents thermal conductivity measurements in suspended graphene as a function of temperature as well as a thickness. In Chapter 5, the thermal conductivity measurements of few-layer h-BN crystals will be presented. Finally, summary and future outlook will be presented in Chapter 6.

## REFERENCES

1. Wallace, P. R., *Phys Rev* **1947**, *71*, 476-476.
2. Novoselov, K. S.; Geim, A. K.; Morozov, S. V.; Jiang, D.; Zhang, Y.; Dubonos, S. V.; Grigorieva, I. V.; Firsov, A. A., *Science* **2004**, *306*, 666-669.
3. Novoselov, K. S.; Geim, A. K.; Morozov, S. V.; Jiang, D.; Katsnelson, M. I.; Grigorieva, I. V.; Dubonos, S. V.; Firsov, A. A., *Nature* **2005**, *438*, 197-200.
4. Zhang, Y. B.; Tan, Y. W.; Stormer, H. L.; Kim, P., *Nature* **2005**, *438*, 201-204.
5. Kim, S.; Nah, J.; Jo, I.; Shahrjerdi, D.; Colombo, L.; Yao, Z.; Tutuc, E.; Banerjee, S. K., *Appl Phys Lett* **2009**, *94*, 062107.
6. Bolotin, K. I.; Sikes, K. J.; Jiang, Z.; Klima, M.; Fudenberg, G.; Hone, J.; Kim, P.; Stormer, H. L., *Solid State Commun* **2008**, *146*, 351-355.
7. Lin, Y. M.; Dimitrakopoulos, C.; Jenkins, K. A.; Farmer, D. B.; Chiu, H. Y.; Grill, A.; Avouris, P., *Science* **2010**, *327*, 662-662.
8. Avouris, P., *Nano Lett* **2010**, *10*, 4285-4294.
9. Lee, C.; Wei, X. D.; Kysar, J. W.; Hone, J., *Science* **2008**, *321*, 385-388.
10. Balandin, A. A.; Ghosh, S.; Bao, W. Z.; Calizo, I.; Teweldebrhan, D.; Miao, F.; Lau, C. N., *Nano Lett* **2008**, *8*, 902-907.
11. Cai, W. W.; Moore, A. L.; Zhu, Y. W.; Li, X. S.; Chen, S. S.; Shi, L.; Ruoff, R. S., *Nano Lett* **2010**, *10*, 1645-1651.

12. Seol, J. H.; Jo, I.; Moore, A. L.; Lindsay, L.; Aitken, Z. H.; Pettes, M. T.; Li, X. S.; Yao, Z.; Huang, R.; Broido, D.; Mingo, N.; Ruoff, R. S.; Shi, L., *Science* **2010**, *328*, 213-216.
13. Sichel, E. K.; Miller, R. E.; Abrahams, M. S.; Buiocchi, C. J., *Phys Rev B* **1976**, *13*, 4607-4611.
14. Zhi, C. Y.; Bando, Y.; Tang, C. C.; Kuwahara, H.; Golberg, D., *Adv Mater* **2009**, *21*, 2889.
15. Qin, S. Y.; Kim, J.; Niu, Q.; Shih, C. K., *Science* **2009**, *324*, 1314-1317.
16. Xia, Y.; Qian, D.; Hsieh, D.; Wray, L.; Pal, A.; Lin, H.; Bansil, A.; Grauer, D.; Hor, Y. S.; Cava, R. J.; Hasan, M. Z., *Nat Phys* **2009**, *5*, 398-402.
17. Zhang, H. J.; Liu, C. X.; Qi, X. L.; Dai, X.; Fang, Z.; Zhang, S. C., *Nat Phys* **2009**, *5*, 438-442.
18. Klein, C. A.; Holland, M. G., *Phys Rev a-Gen Phys* **1964**, *136*, A575.
19. Simpson, A.; Stuckes, A. D., *J Phys Part C Solid* **1971**, *4*, 1710.
20. *Modified from Wolfram demonstrations project.*
21. Castro Neto, A. H.; Guinea, F.; Peres, N. M. R.; Novoselov, K. S.; Geim, A. K., *Rev Mod Phys* **2009**, *81*, 109-162.
22. Das Sarma, S.; Adam, S.; Hwang, E. H.; Rossi, E., *Rev Mod Phys* **2011**, *83*, 407-470.
23. Catellani, A.; Posternak, M.; Baldereschi, A.; Freeman, A. J., *Phys Rev B* **1987**, *36*, 6105-6111.
24. Robertson, J., *Phys Rev B* **1984**, *29*, 2131-2137.

25. Watanabe, K.; Taniguchi, T.; Kanda, H., *Nat Mater* **2004**, *3*, 404-409.
26. Giannozzi, P.; Baroni, S.; Bonini, N.; Calandra, M.; Car, R.; Cavazzoni, C.; Ceresoli, D.; Chiarotti, G. L.; Cococcioni, M.; Dabo, I.; Dal Corso, A.; de Gironcoli, S.; Fabris, S.; Fratesi, G.; Gebauer, R.; Gerstmann, U.; Gougoussis, C.; Kokalj, A.; Lazzeri, M.; Martin-Samos, L.; Marzari, N.; Mauri, F.; Mazzarello, R.; Paolini, S.; Pasquarello, A.; Paulatto, L.; Sbraccia, C.; Scandolo, S.; Sclauzero, G.; Seitsonen, A. P.; Smogunov, A.; Umari, P.; Wentzcovitch, R. M., *J Phys-Condens Mat* **2009**, *21*, 395502.
27. Oshima, C.; Aizawa, T.; Souda, R.; Ishizawa, Y.; Sumiyoshi, Y., *Solid State Commun* **1988**, *65*, 1601-1604.
28. Maultzsch, J.; Reich, S.; Thomsen, C.; Requardt, H.; Ordejon, P., *Phys Rev Lett* **2004**, *92*, 075501
29. Mohr, M.; Maultzsch, J.; Dobardzic, E.; Reich, S.; Milosevic, I.; Damnjanovic, M.; Bosak, A.; Krisch, M.; Thomsen, C., *Phys Rev B* **2007**, *76*, 035439.
30. Serrano, J.; Bosak, A.; Arenal, R.; Krisch, M.; Watanabe, K.; Taniguchi, T.; Kanda, H.; Rubio, A.; Wirtz, L., *Phys Rev Lett* **2007**, *98*, 095503.
31. Geick, R.; Perry, C. H.; Rupprecht, G., *Phys Rev* **1966**, *146*, 543.
32. Nemanich, R. J.; Solin, S. A.; Martin, R. M., *Phys Rev B* **1981**, *23*, 6348-6356.
33. Reich, S.; Ferrari, A. C.; Arenal, R.; Loiseau, A.; Bello, I.; Robertson, J., *Phys Rev B* **2005**, *71*, 205201.
34. Popov, V. N., *Phys Rev B* **2002**, *66*, 153408.
35. Hone, J., *Top Appl Phys* **2001**, *80*, 273-286.

36. Lindsay, L.; Broido, D. A.; Mingo, N., *Phys Rev B* **2010**, *82*, 115427.
37. Benedict, L. X.; Louie, S. G.; Cohen, M. L., *Solid State Commun* **1996**, *100*, 177-180.
38. Chen, S. S.; Wu, Q. Z.; Mishra, C.; Kang, J. Y.; Zhang, H. J.; Cho, K. J.; Cai, W. W.; Balandin, A. A.; Ruoff, R. S., *Nat Mater* **2012**, *11*, 203-207.
39. Chang, C. W.; Fennimore, A. M.; Afanasiev, A.; Okawa, D.; Ikuno, T.; Garcia, H.; Li, D. Y.; Majumdar, A.; Zettl, A., *Phys Rev Lett* **2006**, *97*, 085901.

## Chapter 2. Experimental Techniques

Experimental techniques commonly used for sample preparation and characterization are explained in this chapter. So-called Scotch tape method has been successfully applied to create mono- to few- layer graphene and h-BN on an oxidized silicon substrate. Atomic force microscopy, Raman spectroscopy, transmission electron microscopy, and electrical transport measurement are then employed to characterize structural and electrical properties of graphene. In the last section, a technique to transfer exfoliated samples onto another substrate or device is demonstrated.

### 2.1 SCOTCH TAPE METHOD

The Scotch tape method was developed by K. Novoselov and A. Geim,<sup>1</sup> who were awarded the Nobel Prize in physics in 2010. By simply using an adhesive tape and bulk graphite, they obtained single and few-layer graphene. Figure 2.1 shows images of each step to obtain a single layer graphene. All that is needed for demonstration are a graphite source, an adhesive tape, and a silicon substrate with about 300nm oxide on top. First we start with the bulk graphite [Fig. 2.1 (a)]. By using the sticky side of the tape, we can peel off some flakes from the bulk graphite. The thickness of the flakes transferred on Scotch tape vary, but many of them are initially a few micrometers thick [Fig. 2.1 (b)]. By repeatedly folding and peeling the tape, thinner flakes are obtained on the adhesive side of the tape [Fig. 2.1 (c) and (d)]. Subsequently, the tape with the graphene flakes is pressed onto a silicon substrate with  $\sim 300$  nm oxide, then searching for single and few-layer graphene can be done under an optical microscope.

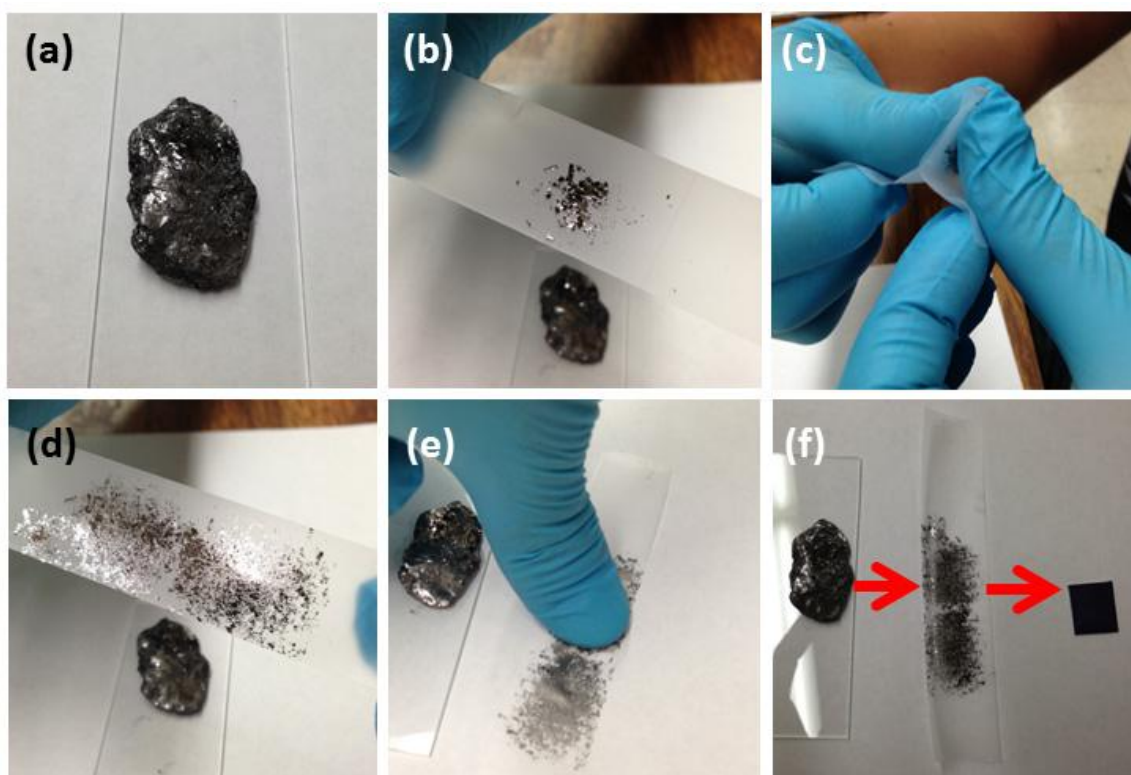


**Figure 2. 1** Scotch tape method. (a) Bulk graphite source (natural graphite). (b) Scotch tape with thin flakes after peeling off from the bulk crystal. (c) Thinning process. (d) Thin flakes created after repeated thinning processes. (e) Pressing the thin flakes onto a substrate. (f) Graphene migration from bulk, to tape, finally onto a substrate.

## 2.2 SAMPLE CHARACTERIZATION METHODS

### 2.2.1 Atomic force microscopy

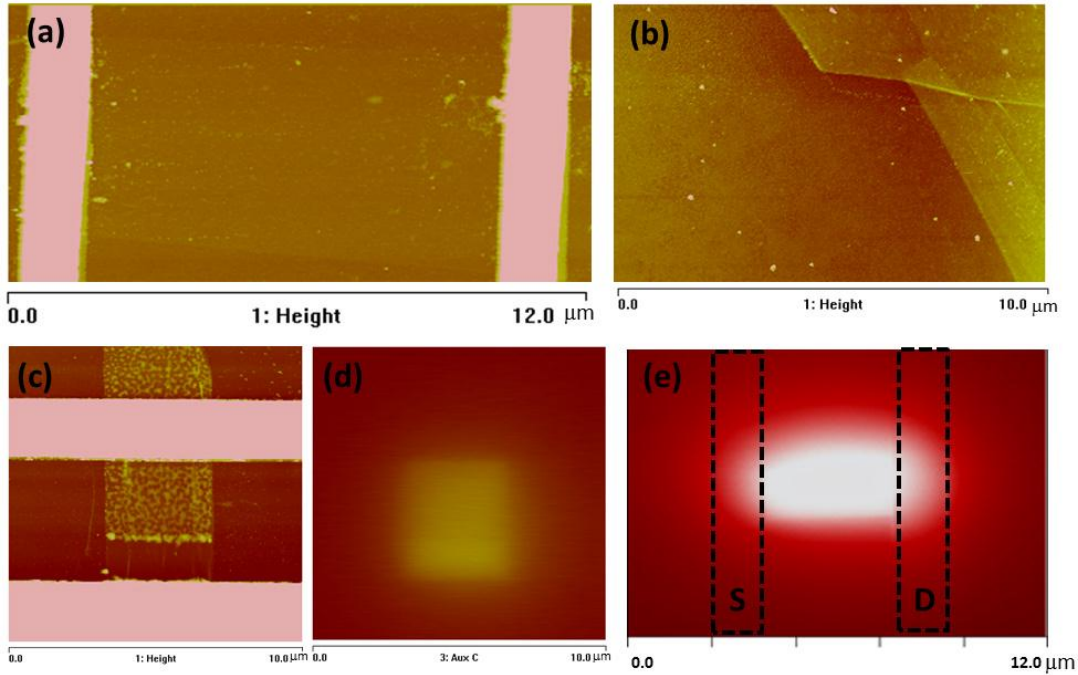


**Figure 2. 2** Application of AFM for graphene device characterization. (a) AFM topography of a graphene channel with two metallic electrodes. (b) Topography of transferred graphene on SiO<sub>2</sub> after annealing. (c) Topography image of graphene device showing the PMMA residue partly removed near bottom electrode. (d) Scanning gate microscopy image of the same device shown in (c). (e) Scanning thermal microscopy image showing the thermovoltage signals in a Joule-heated graphene channel, demonstrated in Chapter 3.

Atomic force microscope (AFM) is widely used to investigate the topography of graphene surfaces as well as device structures with a sub-nanometer resolution. Tapping mode AFM is typically used to obtain topography images. Although the thickness of a single layer graphene can be resolved from the height profile for clean samples, tip-

sample deformation, water adsorbates or tape residue on the surface can often induce an error to the height profile. Figures 2.2 (a) and (b) show the topography of a graphene device and a transferred and annealed graphene on SiO<sub>2</sub> substrate, respectively. Because the properties of graphene are very sensitive to the surface condition, topography image provides valuable information in understanding the properties of a graphene device. For instance, shown in Fig. 2.2 (c) is the graphene channel partly covered with PMMA residue. The clean area close to the bottom electrode is obtained after employing a contact-mode AFM to remove the PMMA residue during scanning.<sup>2</sup> In Fig. 2.2 (d), scanning gate microscopy is employed on the same device in (c), where locally gated tip changes the resistance of the graphene channel, which shows inhomogeneous local conductivity in the graphene channel.<sup>3,4</sup> Lastly, as presented in Chapter 3, the scanning thermal microscopy is used to map out the temperature distribution in an electrically biased graphene channel as shown in Fig. 2.2. (e).

### **2.2.2 Raman spectroscopy**

Raman spectroscopy is a non-contact optical measurement technique that has been used for structural characterization in graphitic material including graphene<sup>5-8</sup> and carbon nanotubes.<sup>9,10</sup> An incident laser on graphene induces the electron excitation, then the coupling of the excited electrons with phonons results in strong Raman active G and 2D bands. Raman G band in single layer graphene, centered at 1582 cm<sup>-1</sup> in Fig. 2.3 (a), is associated with optical phonons at the zone center [Fig. 2.3 (e)], which correspond to

the relative vibrations of the two sub-lattices against each other.<sup>6, 11</sup> The Raman 2D mode in graphene, centered at  $2670 \text{ cm}^{-1}$  in Fig. 2.3 (b), is a consequence of the double resonance process of zone boundary optical phonons, as illustrated in Fig. 2.3 (f).<sup>6, 11</sup> Defect-induced D band is also observed at  $\sim 1350 \text{ cm}^{-1}$  for some defective crystals containing vacancies<sup>12, 13</sup> and edges<sup>14, 15</sup> with broken bonds. The measured Raman shifts and the full width half maximum (FWHM) of the Raman peak vary with laser excitation energy,<sup>6</sup> chemical<sup>7</sup> and electrical<sup>16, 17</sup> doping, stacking order,<sup>18</sup> and mechanical strain.<sup>17, 19</sup> Hence, both experimental and theoretical studies on the Raman spectra in graphene have been actively pursued.<sup>5, 6</sup>

Raman spectra show clear difference between samples of different layer thicknesses as shown in Fig. 2.3 (a) to (d). In particular, the intensity ratio of 2D band over G band,  $I_{2D}/I_G$ , is used to identify single layer graphene. As shown in Fig. 2.3 (a) to (c),  $I_{2D}/I_G$  decreases as the layer thickness increases. Moreover, FWHM of 2D band increases as the layer thickness increases, which is associated with the electronic band structure near the K and K' points. In bilayer graphene, for example, because of the four eligible double resonance modes [Fig. 2.3 (g)], 2D band consists of 4 Lorentzians in contrast to a single Lorentzian fit in single layer graphene, resulting in the broadening of the peak, as shown in Fig. 2.3 (d).

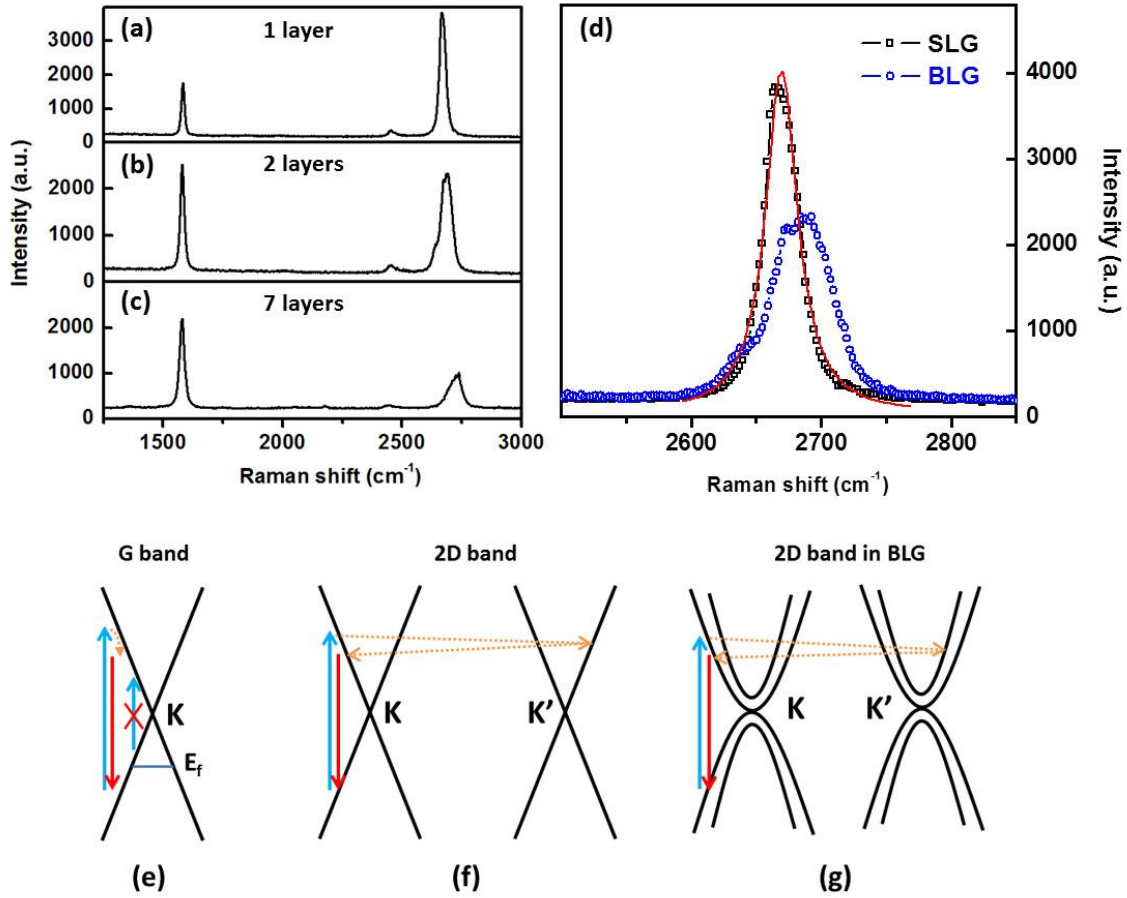


**Figure 2. 3** Raman spectra of (a) single, (b) bi-, and (c) 7-layer graphene showing Raman active G and 2D mode peaks. 532 nm laser excitation is used for single and bi-layer, while 488 nm laser is used for 7 layer graphene. (d) The difference between the single and bi-layer graphene for the 2D mode peak. (e) and (f) are schematics of the Raman G and 2D bands in single layer graphene. (g) One of the double resonance modes of 2D band in bilayer graphene. Blue and red arrows represent electron-hole pair creation and annihilation, and orange dotted arrow represents phonons associated with the Raman modes.  $E_f$  in (e) indicates the Fermi energy.

Interestingly, linear temperature dependence of the Raman G band and 2D band shifts have been observed in single and bi-layer graphene. As the temperature increases

the G and 2D bands showed a constant red shift over the temperature range between 70 K and 500 K.<sup>20, 21</sup> This behavior forms the basis for Raman-based thermometry, with which the thermal conductivity of graphene has been measured based on the temperature profile in a laser heated suspended graphene.<sup>21, 22</sup> In addition, despite the large error and limited spatial resolution of this technique, this method has also been employed to investigate the temperature distribution in a Joule-heated graphene<sup>23, 24</sup> as discussed in Chapter 3. We have applied both Raman-based thermometry and scanning thermal microscopy to an electrically heated graphene for comparison, and our observations are presented in Chapter 3.

### **2.2.3 Transmission electron microscopy**

Transmission electron microscopy (TEM) is used to characterize the crystal structure of a suspended sample and to resolve surface polymers in graphene<sup>25, 26</sup> and h-BN.<sup>27</sup> Figure 2.4 (a) shows the low magnification TEM image of a suspended few-layer h-BN as presented in Chapter 5. Figure 2.4 (b) shows electron diffraction patterns of a suspended h-BN, that shows a single set of hexagonal Bragg diffraction peaks. Our TEM results typically show highly ordered single crystalline structure in graphene and h-BN within the maximum device dimension of  $\sim 7.5 \mu\text{m}$ . The high resolution TEM image showing lattice fringes at the folded edge in Fig 2.4 (c) can be used to count the number of atomic layers in the samples. The image also revealed the presence of a thin layer of polymer on the surface, which is the key to understanding the suppression in thermal

conductivities in our samples. The TEM measurements presented here were performed by M. T. Pettes using an FEI Tecnai G2 F20 TEM with acceleration voltages between 120-200 kV.

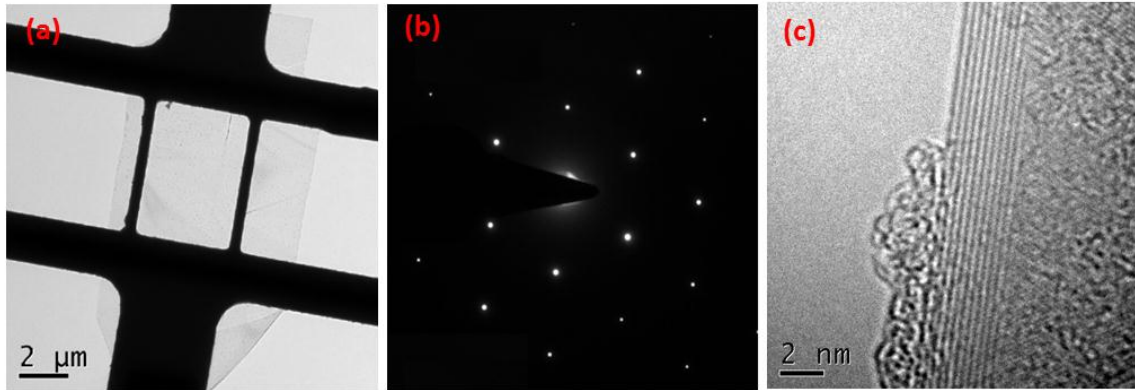


**Figure 2. 4** TEM images and diffraction pattern of suspended few-layer h-BN. (a) Low magnification TEM image of a suspended h-BN on a micro-bridge device. (b) Selected area electron diffraction pattern revealing a single crystalline hexagonal crystal structure. (c) High resolution image resolving the number of layers on the folded edge of the h-BN.

#### 2.2.4 Electrical transport measurement

Because of rich electronic properties of single and few-layer graphene, or graphene/h-BN hetero-structures, numerous experimental and theoretical studies have been done extensively and the results can be found in several review articles.<sup>28-30</sup> Here, we will only show the general features of electrical transport in single layer graphene devices.

The electric-field induced resistance change in the graphene channel is measured using AC lock-in technique with low excitation currents of 0.1-1 μA and low frequency

of  $\sim 10$  Hz. Graphene channel with a silicon back gate separated by  $\sim 300$  nm  $\text{SiO}_2$  is typically used for the scanning thermal microscopy study presented in Chapter 3.

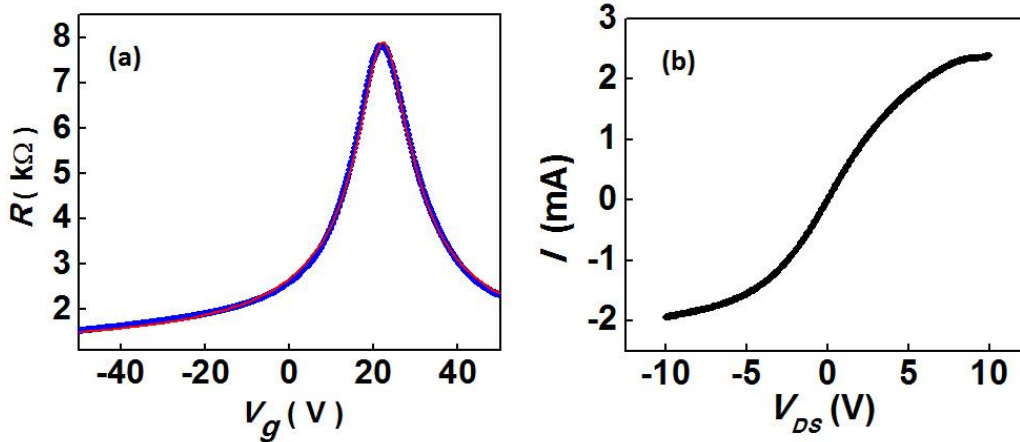


**Figure 2. 5** Electrical properties of graphene (a)  $R$  vs.  $V_g$  measurement results (blue) on a device with a transport model fitting (red). (b) Current ( $I$ ) vs. drain-source voltage ( $V_{DS}$ ) for the same device at  $V_g = -20\text{V}$ .

Figure 2.5 (a) shows two-probe resistance ( $R$ ) vs back gate voltage ( $V_g$ ) (blue curve) measured with AC lock-in technique together with a model fitting (red curve). Ambipolar nature of graphene is clearly seen, i.e., on the left hand side of the Dirac point ( $V_D = 20$  V), holes are majority carriers, while electrons are majority carriers on the right hand side. The positive value of  $V_D$  suggests that the graphene channel is hole-doped at  $V_g = 0$  V. Near the Dirac point, both residual electron and hole carriers coexist due to the formation of electron and hole puddles<sup>31</sup> near local charge impurities.<sup>32</sup> Because of extrinsic charge impurities, the Dirac point of graphene varies from sample to sample.

This gate dependent resistance can be used to extract low field mobility ( $\mu$ ), residual charge concentration ( $n_0$ ), and contact resistance ( $R_{ct}$ ) for each device. Assuming

a constant mobility, the two-probe resistance is fitted with a model suggested by Kim et al.<sup>33</sup>

$$R_{tot}(V_g) = R_{ct} + \frac{N_{sq}}{\sqrt{n_0^2 + n^2(V_g - V_D)e\mu}} \quad (2.1)$$

where  $N_{sq}$  is channel length divided by channel width,  $e$  is elementary charge,  $V_D$  is gate bias voltage at maximum resistance, and  $n$  is the field-induced carrier concentration.

Due to the two dimensional nature and linear dispersion of electrons, an applied gate voltage induces carrier concentration  $n$  according to<sup>16, 33</sup>

$$V_g - V_D = \frac{e}{C_{ox}}n + \frac{\hbar v_F \sqrt{\pi n}}{e} \quad (2.2)$$

where  $C_{ox}$  is the geometrical capacitance of the gate oxide, and  $v_F$  is the Fermi velocity in graphene. The second term is derived from the quantum capacitance in a two dimensional free-electron gas model.<sup>34</sup>

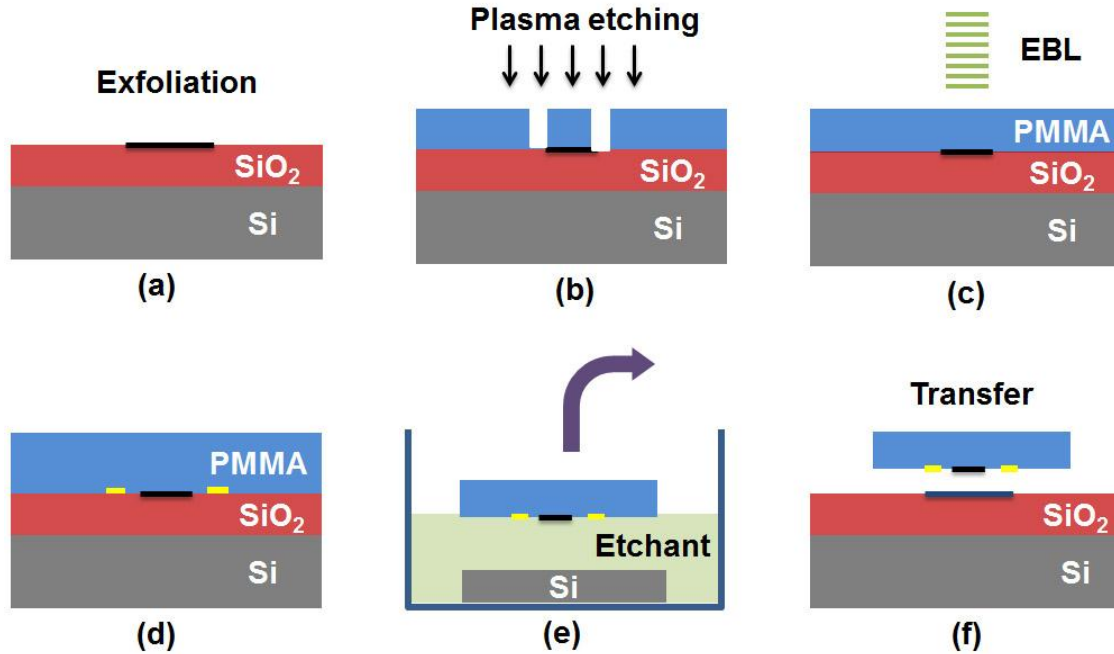
Using the model, the extracted values of  $n_0 = 2.7 \times 10^{11} \text{ cm}^{-2}$ ,  $\mu = 6800 \text{ cm}^2\text{V}^{-1}\text{s}^{-1}$ , and  $R_{ct} = 680 \text{ } \Omega$  are obtained for the device shown in Fig. 2.5. Typical mobility values of single layer graphene range between 6,000 and 10,000  $\text{cm}^2\text{V}^{-1}\text{s}^{-1}$  in our devices, indicative of high quality samples.

Figure 2.5 (b) shows a DC current vs voltage measurement at high drain-source bias voltage ( $V_{DS}$ ) in a hole-doped graphene channel ( $V_g = -20\text{V}$ ). It is interesting that a single layer graphene can carry a current density as high as  $2.2 \times 10^8 \text{ Acm}^{-2}$ ,<sup>35</sup> similar to the value observed in carbon nanotubes.<sup>36</sup> The saturation of current occurs at  $V_{DS} = 10 \text{ V}$ , which may be attributed to the carrier backscattering by surface polar phonons in  $\text{SiO}_2$

with an energy  $\sim 56$  meV.<sup>23,37</sup> The applied high current density heats up the graphene channel and the resulting temperature profile is investigated with scanning thermal microscopy in Chapter 3.

### **2.3 TRANSFER TECHNIQUE**

Transferring graphene or h-BN from one substrate to another is possible by the use of Poly(methyl methacrylate) (PMMA) support. This transfer process was initially used to transfer graphene grown on metal substrates by chemical vapor deposition (CVD) onto a silicon substrate by etching the underlying metallic substrates.<sup>38,39</sup> It was also used to transfer graphene onto a TEM grid to study the crystal structure of graphene.<sup>40,41</sup> In addition, graphene hetero-structures<sup>42,43</sup> with more than two graphene layers and/or h-BN layers are made by using multiple transfer processes.



**Figure 2. 6** Schematic diagram of the transfer process using a PMMA support. (a) Graphene or h-BN sample exfoliated on Si substrates covered with SiO<sub>2</sub>. (b) Sample patterning with the use of plasma etching after EBL on PMMA coated sample. (c) Second EBL process to define registration marks (d) Thick PMMA coating on top of sample and registration marks. (e) PMMA support floating after etching sacrificial layer. (f) Transfer onto a target substrate or a device.

Figure 2.6 shows a schematic diagram of PMMA-assisted transfer process, which is used to prepare suspended graphene and h-BN as presented in Chapter 4 and 5. First, a thin layer sample is exfoliated on a silicon substrate by using the Scotch tape method [Fig. 2.6 (a)]. Because the exfoliated sample has an irregular shape, we coated the sample with PMMA resist and performed standard electron beam lithography (EBL) to draw desired pattern on the resist layer. After the resist was developed, plasma etching using oxygen for graphene (CF<sub>4</sub> for h-BN) was applied to remove the exposed region [Fig. 2.6

(b)]. Thin layer graphene or h-BN may be too transparent to be visible during the transfer process. Thus, we deposited registration marks around the sample to facilitate precise alignment in the next step. This can be done with an extra EBL step followed by gold deposition without using an adhesion layer [Fig. 2.6 (c)]. Then, the substrate with the patterned sample and the registration marks was spin coated with a  $\sim 1.5 \mu\text{m}$  thick PMMA support film [Fig. 2.6 (d)], and the  $\text{SiO}_2$  layer is subsequently removed with 1% hydrofluoric acid (HF) or 3M NaOH, which makes the PMMA film float over the etchant solution [Fig. 2.6 (e)]. After rinsing the PMMA film with deionized water several times, the PMMA/sample was aligned on a target substrate or device with the help of the registration marks under an optical microscope [Fig. 2.6(f)]. Lastly, the PMMA support film is dissolved in warm acetone and rinsed with isopropanol multiple times. The remaining PMMA residue can be removed with thermal annealing<sup>43, 44</sup> or current annealing.<sup>45</sup> However, it has been observed that the PMMA residue can be difficult to completely remove.<sup>46, 47</sup> PMMA residue remaining on the surface has been an issue for our thermal transport measurements as it can result in phonon scattering, which will be discussed in Chapters 4 and 5.

## 2.4 SUMMARY

In this chapter, several experimental techniques were introduced to fabricate two dimensional graphene or h-BN devices for the experiments. The simple Scotch tape method was able to produce single and few- layer graphene, h-BN and other layered materials. AFM was used to probe the surface topography of the samples, and also in the

scanning thermal microscopy mode to study the temperature distribution in graphene channel, which will be presented in Chapter 3. Raman spectroscopy was a powerful optical measurement technique to determine the graphene thickness and to investigate the structural properties of graphene. Temperature dependence of the Raman peak shifts can be used to infer the temperature in a Joule-heated graphene channel. TEM provided the crystallographic information as well as high resolution lattice fringe images, that could be used to count the number of atomic layers in graphene and h-BN. Electrical transport measurement as a function of gate was performed and the result can be used to obtain the carrier mobility in the graphene devices. Lastly, sample transfer technique using PMMA support was developed to make suspended graphene and h-BN for thermal conductivity measurements, as presented in Chapter 4 and 5.

## REFERENCES

1. Novoselov, K. S.; Geim, A. K.; Morozov, S. V.; Jiang, D.; Zhang, Y.; Dubonos, S. V.; Grigorieva, I. V.; Firsov, A. A., *Science* **2004**, *306*, 666-669.
2. Goossens, A. M.; Calado, V. E.; Barreiro, A.; Watanabe, K.; Taniguchi, T.; Vandersypen, L. M. K., *Appl Phys Lett* **2012**, *100*, 073110.
3. Connolly, M. R.; Chiou, K. L.; Smith, C. G.; Anderson, D.; Jones, G. A. C.; Lombardo, A.; Fasoli, A.; Ferrari, A. C., *Appl Phys Lett* **2010**, *96*, 113501.
4. Jalilian, R.; Jauregui, L. A.; Lopez, G.; Tian, J. F.; Roecker, C.; Yazdanpanah, M. M.; Cohn, R. W.; Jovanovic, I.; Chen, Y. P., *Nanotechnology* **2011**, *22*, 295705.
5. Ferrari, A. C.; Meyer, J. C.; Scardaci, V.; Casiraghi, C.; Lazzeri, M.; Mauri, F.; Piscanec, S.; Jiang, D.; Novoselov, K. S.; Roth, S.; Geim, A. K., *Phys Rev Lett* **2006**, *97*, 187401.
6. Malard, L. M.; Pimenta, M. A.; Dresselhaus, G.; Dresselhaus, M. S., *Phys Rep* **2009**, *473*, 51-87.
7. Ryu, S.; Liu, L.; Berciaud, S.; Yu, Y. J.; Liu, H. T.; Kim, P.; Flynn, G. W.; Brus, L. E., *Nano Lett* **2010**, *10*, 4944-4951.
8. Graf, D.; Molitor, F.; Ensslin, K.; Stampfer, C.; Jungen, A.; Hierold, C.; Wirtz, L., *Nano Lett* **2007**, *7*, 238-242.
9. Jorio, A.; Pimenta, M. A.; Souza, A. G.; Saito, R.; Dresselhaus, G.; Dresselhaus, M. S., *New J Phys* **2003**, *5*, 139.
10. Rao, A. M.; Eklund, P. C.; Bandow, S.; Thess, A.; Smalley, R. E., *Nature* **1997**, *388*, 257-259.

11. Ferrari, A. C.; Meyer, J. C.; Scardaci, V.; Casiraghi, C.; Lazzeri, M.; Mauri, F.; Piscanec, S.; Jiang, D.; Novoselov, K. S.; Roth, S.; Geim, A. K., *Phys Rev Lett* **2006**, *97*.
12. Kudin, K. N.; Ozbas, B.; Schniepp, H. C.; Prud'homme, R. K.; Aksay, I. A.; Car, R., *Nano Lett* **2008**, *8*, 36-41.
13. Lucchese, M. M.; Stavale, F.; Ferreira, E. H. M.; Vilani, C.; Moutinho, M. V. O.; Capaz, R. B.; Achete, C. A.; Jorio, A., *Carbon* **2010**, *48*, 1592-1597.
14. Casiraghi, C.; Hartschuh, A.; Qian, H.; Piscanec, S.; Georgi, C.; Fasoli, A.; Novoselov, K. S.; Basko, D. M.; Ferrari, A. C., *Nano Lett* **2009**, *9*, 1433-1441.
15. Cancado, L. G.; Jorio, A.; Ferreira, E. H. M.; Stavale, F.; Achete, C. A.; Capaz, R. B.; Moutinho, M. V. O.; Lombardo, A.; Kulmala, T. S.; Ferrari, A. C., *Nano Lett* **2011**, *11*, 3190-3196.
16. Das, A.; Pisana, S.; Chakraborty, B.; Piscanec, S.; Saha, S. K.; Waghmare, U. V.; Novoselov, K. S.; Krishnamurthy, H. R.; Geim, A. K.; Ferrari, A. C.; Sood, A. K., *Nat Nanotechnol* **2008**, *3*, 210-215.
17. Wang, F.; Zhang, Y. B.; Tian, C. S.; Girit, C.; Zettl, A.; Crommie, M.; Shen, Y. R., *Science* **2008**, *320*, 206-209.
18. Lui, C. H.; Li, Z. Q.; Chen, Z. Y.; Klimov, P. V.; Brus, L. E.; Heinz, T. F., *Nano Lett* **2011**, *11*, 164-169.
19. Ni, Z. H.; Yu, T.; Lu, Y. H.; Wang, Y. Y.; Feng, Y. P.; Shen, Z. X., *Acs Nano* **2008**, *2*, 2301-2305.

20. Calizo, I.; Balandin, A. A.; Bao, W.; Miao, F.; Lau, C. N., *Nano Lett* **2007**, *7*, 2645-2649.
21. Cai, W. W.; Moore, A. L.; Zhu, Y. W.; Li, X. S.; Chen, S. S.; Shi, L.; Ruoff, R. S., *Nano Lett* **2010**, *10*, 1645-1651.
22. Balandin, A. A.; Ghosh, S.; Bao, W. Z.; Calizo, I.; Teweldebrhan, D.; Miao, F.; Lau, C. N., *Nano Lett* **2008**, *8*, 902-907.
23. Freitag, M.; Steiner, M.; Martin, Y.; Perebeinos, V.; Chen, Z. H.; Tsang, J. C.; Avouris, P., *Nano Lett* **2009**, *9*, 1883-1888.
24. Jo, I.; Hsu, I. K.; Lee, Y. J.; Sadeghi, M. M.; Kim, S.; Cronin, S.; Tutuc, E.; Banerjee, S. K.; Yao, Z.; Shi, L., *Nano Lett* **2011**, *11*, 85-90.
25. Pettes, M. T.; Jo, I. S.; Yao, Z.; Shi, L., *Nano Lett* **2011**, *11*, 1195-1200.
26. Huang, P. Y.; Ruiz-Vargas, C. S.; van der Zande, A. M.; Whitney, W. S.; Levendorf, M. P.; Kevek, J. W.; Garg, S.; Alden, J. S.; Hustedt, C. J.; Zhu, Y.; Park, J.; McEuen, P. L.; Muller, D. A., *Nature* **2011**, *469*, 389.
27. Alem, N.; Erni, R.; Kisielowski, C.; Rossell, M. D.; Gannett, W.; Zettl, A., *Phys Rev B* **2009**, *80*, 155425.
28. Castro Neto, A. H.; Guinea, F.; Peres, N. M. R.; Novoselov, K. S.; Geim, A. K., *Rev Mod Phys* **2009**, *81*, 109-162.
29. Avouris, P., *Nano Lett* **2010**, *10*, 4285-4294.
30. Das Sarma, S.; Adam, S.; Hwang, E. H.; Rossi, E., *Rev Mod Phys* **2011**, *83*, 407-470.

31. Martin, J.; Akerman, N.; Ulbricht, G.; Lohmann, T.; Smet, J. H.; Von Klitzing, K.; Yacoby, A., *Nat Phys* **2008**, *4*, 144-148.
32. Chen, J. H.; Jang, C.; Xiao, S. D.; Ishigami, M.; Fuhrer, M. S., *Nat Nanotechnol* **2008**, *3*, 206-209.
33. Kim, S.; Nah, J.; Jo, I.; Shahrjerdi, D.; Colombo, L.; Yao, Z.; Tutuc, E.; Banerjee, S. K., *Appl Phys Lett* **2009**, *94*, 062107.
34. Luryi, S., *Appl Phys Lett* **1988**, *52*, 501-503.
35. Meric, I.; Han, M. Y.; Young, A. F.; Ozyilmaz, B.; Kim, P.; Shepard, K. L., *Nat Nanotechnol* **2008**, *3*, 654-659.
36. Yao, Z.; Kane, C. L.; Dekker, C., *Phys Rev Lett* **2000**, *84*, 2941-2944.
37. Meric, I.; Dean, C. R.; Young, A. F.; Baklitskaya, N.; Tremblay, N. J.; Nuckolls, C.; Kim, P.; Shepard, K. L., *Nano Lett* **2011**, *11*, 1093-1097.
38. Li, X. S.; Cai, W. W.; An, J. H.; Kim, S.; Nah, J.; Yang, D. X.; Piner, R.; Velamakanni, A.; Jung, I.; Tutuc, E.; Banerjee, S. K.; Colombo, L.; Ruoff, R. S., *Science* **2009**, *324*, 1312-1314.
39. Kim, K. S.; Zhao, Y.; Jang, H.; Lee, S. Y.; Kim, J. M.; Kim, K. S.; Ahn, J. H.; Kim, P.; Choi, J. Y.; Hong, B. H., *Nature* **2009**, *457*, 706-710.
40. Meyer, J. C.; Geim, A. K.; Katsnelson, M. I.; Novoselov, K. S.; Booth, T. J.; Roth, S., *Nature* **2007**, *446*, 60-63.
41. Huang, P. Y.; Ruiz-Vargas, C. S.; van der Zande, A. M.; Whitney, W. S.; Levendorf, M. P.; Kevek, J. W.; Garg, S.; Alden, J. S.; Hustedt, C. J.; Zhu, Y.; Park, J.; McEuen, P. L.; Muller, D. A., *Nature* **2011**, *469*, 389.

42. Kim, S.; Jo, I.; Nah, J.; Yao, Z.; Banerjee, S. K.; Tutuc, E., *Phys Rev B* **2011**, *83*, 161401.
43. Dean, C. R.; Young, A. F.; Meric, I.; Lee, C.; Wang, L.; Sorgenfrei, S.; Watanabe, K.; Taniguchi, T.; Kim, P.; Shepard, K. L.; Hone, J., *Nat Nanotechnol* **2010**, *5*, 722-726.
44. Ni, Z. H.; Wang, H. M.; Luo, Z. Q.; Wang, Y. Y.; Yu, T.; Wu, Y. H.; Shen, Z. X., *J Raman Spectrosc* **2010**, *41*, 479-483.
45. Bolotin, K. I.; Sikes, K. J.; Jiang, Z.; Klima, M.; Fudenberg, G.; Hone, J.; Kim, P.; Stormer, H. L., *Solid State Commun* **2008**, *146*, 351-355.
46. Lin, Y. C.; Jin, C. H.; Lee, J. C.; Jen, S. F.; Suenaga, K.; Chiu, P. W., *Acs Nano* **2011**, *5*, 2362-2368.
47. Lin, Y. C.; Lu, C. C.; Yeh, C. H.; Jin, C. H.; Suenaga, K.; Chiu, P. W., *Nano Lett* **2012**, *12*, 414-419.

## Chapter 3. Scanning Thermal Microscopy Measurement on Graphene Devices

### 3.1 INTRODUCTION

Several different thermometry techniques have been used for the temperature measurements of different energy carriers in electrically biased graphene devices at high current densities.<sup>1-5</sup> Thermal emission spectroscopy in the near-infrared<sup>1, 4</sup> and visible range<sup>2</sup> has been measured and fitted with the Planck distribution to determine the electronic temperature, where it reaches as high as 1570 K at a power density of 500 kW/cm<sup>2</sup>. The ratio of anti-Stokes and Stokes Raman G mode has been used to deduce the temperature of the zone-center optical G phonons.<sup>3</sup> This method is accurate only when the temperature of the zone-center optical phonons is higher than about 600 K, below which the anti-Stokes peak is too small to be measured accurately. Nevertheless, the temperature of the optical G phonons has been found to be close to the electronic temperature, suggesting strong coupling between high-energy electrons and optical G phonons. Another method based on the Raman G band relies on the downward shift of the G band with increasing temperature.<sup>6</sup> The temperature determined from this method reflects the equivalent temperature of the anharmonic scattering processes between the zone-center optical phonons and the intermediate frequency phonons (IFPs),<sup>7, 8</sup> although the position of the G peak is also known to be sensitive to impurity doping and strain.<sup>7, 9</sup> Similarly, the shift of the Raman 2D band, involving the scattering of two zone-boundary optical phonons into IFPs, has been employed to estimate the equivalent temperature of these anharmonic decaying processes.<sup>4, 5</sup> The work by Chae et al.<sup>3</sup> and Berciaud et al.<sup>2</sup>

suggested that the IFPs may not be in full equilibrium with high-energy electrons and optical phonons, while the work by Freitag et al.<sup>4</sup> suggested that both the electrons and phonons were in full equilibrium.

Although these optical non-contact measurements have yielded a rich set of data of electronic and zone-center optical phonon temperatures, as well as the anharmonic scattering temperatures of zone-center and zone-boundary optical phonons, there is still a lack of direct measurement of the low-frequency acoustic phonon temperatures. Such phonons play an important role in heat dissipation as they are primarily responsible for the in-plane thermal conductivity due to their large group velocity as well as the interfacial thermal conductance because of an increasing interface transmission coefficient with decreasing frequency at a van der Waals interface.<sup>10,11</sup> As such, they are relevant to the burn-out behavior of graphene. In addition, one disadvantage of the optical mapping methods is the spatial resolution that is limited by far field diffraction to be comparable to the wavelength. For example, IR emission spectroscopy has identified bias-dependent hot spot locations in electrically-heated graphene devices.<sup>1,4</sup> So far, this observation has been limited to long-channel devices with a channel length longer than 25  $\mu\text{m}$ . It is unclear whether the hot spots still exist in short-channel devices due to increased lateral heat transfer to the contacts.

In this chapter, we present a contact measurement method for high-spatial-resolution quantitative mapping of the low-frequency acoustic phonon temperature distribution in electrically-biased graphene. With the use of a combined contact mode and lift mode operation of a scanning thermal microscopy (SThM) probe tip, we were able to

determine the low-frequency acoustic phonon temperature profiles in the graphene channel with a spatial resolution on the order of 100 nm. Using this method, we were able to resolve bias-dependent hot spots in electrically biased graphene channels that were considerably smaller than those used in the IR mapping experiments.<sup>1,4</sup> In addition, the high temperature sensitivity of the SThM technique allows us to examine the thermal behavior of the graphene in the low-power density regime that was not accessible by the optical techniques due to their limited temperature sensitivity.

### 3.2 SCANNING THERMAL MICROSCOPY

SThM has been developed for imaging temperature distribution on the surface of devices and nanostructures. The SThM sensor is a custom-made atomic force microscopy (AFM) tip with a sub-micron Pt-Cr thermocouple fabricated at the tip apex,<sup>12, 13</sup> as shown in the scanning electron micrograph (SEM) in Fig. 3.1 (a). The heat transfer mechanism that induces thermovoltage signal is shown Fig. 3.1 (b). When the thermocouple sensor is in contact with the sample, a thin oxide layer on the Cr surface prevents direct electronic coupling between the sensor and sample. On the other hand, phonon coupling across the tip-sample interface via the solid-solid contact and the surrounding liquid meniscus causes a change in the thermocouple temperature. With the low contact force used in the measurement, the phonon transmission coefficient across the weakly interacting interface is inversely proportional to  $\omega^2$ , where  $\omega$  is the phonon frequency.<sup>10, 11</sup> Consequently, low- $\omega$  acoustic phonons in graphene make much larger contribution to the sensor temperature

change than the high- $\omega$  phonons. During the measurements in ambient condition, parasitic heat transfer also occurs through the air gap between the sample and the cantilever. Recently, SThM measurement has been performed under ultra-high vacuum by Kim et al.<sup>14</sup>, where heat transfer by air convection is eliminated. Because our measurements were conducted in air, thermovoltage signals are affected not only by the local temperature at the contact, but also by the temperature of the substrate and the cantilever. The contribution from parasitic heat transfer processes was eliminated by combining contact mode and lift mode scanning in our SThM, as discussed later in the Chapter.

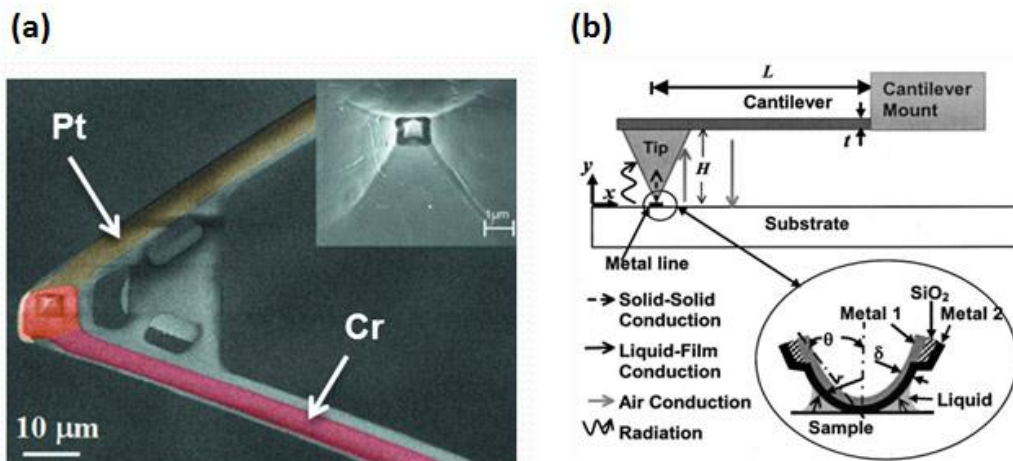


**Figure 3. 1** SEM micrograph of a SThM tip showing a Pt-Cr thermocouple fabricated at the apex (a). Heat transfer mechanism in the SThM measurement (b). Adopted from Shi et al.<sup>12</sup>

### **3.3 SAMPLE PREPARATION AND EXPERIMENTAL SET-UP**

#### **3.3.1 Graphene sample preparation**

Graphene devices were fabricated by using standard electron-beam lithography (EBL) and metal lift-off process as well as oxygen plasma etching. First, single layer graphene was exfoliated onto a 300 nm thick thermally grown oxide on 500  $\mu\text{m}$  thick silicon substrate. The first EBL process defined the rectangular shape of the graphene device, followed by an oxygen plasma etching for 10-30 seconds. Subsequently, a second layer of PMMA was coated and baked for the second EBL to draw the metal deposition structure. 5/50nm thick Cr/Au was deposited using a thermal evaporator. In order to obtain the high mobility sample, we thoroughly cleaned the PMMA in warm acetone at  $\sim 60^\circ\text{C}$  combined with 3 times of acetone and IPA rinse processes. Fig. 3.2 (a) shows the optical image of a device measured in this study. The 100  $\mu\text{m}$  long resistance thermometer line was calibrated in a variable temperature stage without self-heating, then the resistance change induced by self-heating with large DC bias is converted to the temperature rise as shown in Fig. 3.2 (b).

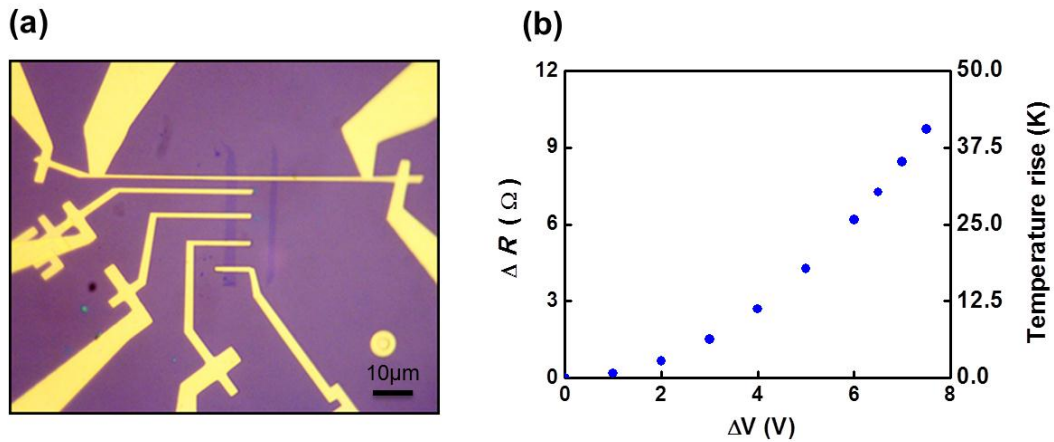


**Figure 3. 2** (a) Optical micrograph of a graphene device with four Au/Cr metal electrodes and an adjacent 100  $\mu\text{m}$  long, 1  $\mu\text{m}$ -wide Au/Cr heater and resistance thermometer line patterned on top of the graphene. (b) The resistance change of the thermometer line at large DC bias voltages is used for temperature calibration.

### 3.3.2 SThM set-up

The schematic diagram for the experimental set-up is shown in Fig. 3.3. For the SThM measurements, we used a MultiMode AFM with the Nanoscope IIIa controller (Digital Instruments) equipped with the Signal Access Module. SThM tip was mounted on a custom-made tip holder and the two terminals of the thermocouple were wire bonded to two metal plates that were connected to an SR 560 voltage preamplifier. A silicon substrate with a graphene device was mounted on a chip carrier, wire-bonded, and connected to the external electronics which applies bias voltages and measures the current. SThM measurements were conducted in the contact mode, while the lift mode was employed to calibrate the temperature response of the sensor, as detailed in Appendix A.

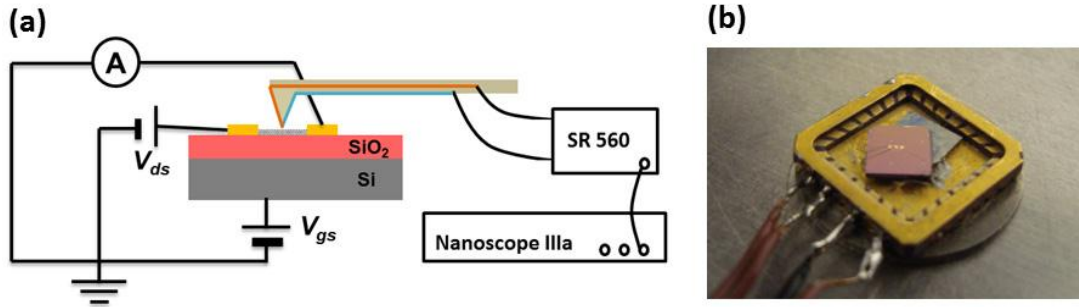


**Figure 3. 3** (a) Schematic diagram of the instrumental set-up. (b) Graphene device mounted on a sample stage.

### 3.4 RESULTS

We have performed the SThM measurements on 3 single-layer graphene devices with the channel lengths and widths of  $6.7 \mu\text{m} \times 3.8 \mu\text{m}$  (Device 1),  $9.6 \mu\text{m} \times 3.3 \mu\text{m}$  (Device 2), and  $7.0 \mu\text{m} \times 4.0 \mu\text{m}$  (Device 3), respectively. Figure 3.4 (a) displays the linear-response resistance ( $R$ ) as a function of silicon back gate voltage ( $V_{GS}$ ) in Device 1, showing typical ambipolar behavior. The maximum resistance occurs at 4.5 V, corresponding to the Dirac point,  $V_{GS-0}$ . The dominant charge carriers to the left and right of  $V_{GS-0}$  are holes and electrons, respectively. The carrier mobilities extracted from the  $R$  vs.  $V_{GS}$  curves range from 6,000 to 10,000  $\text{cm}^2\text{V}^{-1}\text{s}^{-1}$ ,<sup>15</sup> which is indicative of the high quality of our devices.

Figures 3.4 (b) to (d) show the contact-mode SThM measurements of Device 1 at different gate voltages and at a constant drain-source bias ( $V_{DS}$ ) of 4 V. Remarkably, the thermovoltage signal exhibits a non-uniform profile along the graphene channel. For  $V_{GS}$

= -20 V, which makes the graphene channel hole doped, the temperature rise near the grounded source electrode is much higher than the other areas along the channel [Fig. 3.4 (b)]. When  $V_{GS}$  was at 0 V and close to the Dirac point, the hot spot was found to have moved toward the middle of the channel [Fig. 3.4 (c)]. When the gate bias was increased further to 40 V causing electron doping, the hot spot appeared on the drain electrode side [Fig. 3.4 (d)].

The obtained thermovoltage map also displays a strong dependence on the drain-source voltage. Figures 3.4 (e) to (h) show the thermovoltage maps measured on Device 2 under different bias conditions. The Dirac point for this device is  $\sim 22$  V. Similar to Device 1, at a positive drain-source voltage of 6 V, the hot spot shifted from the grounded source side on the left to the drain side on the right when the gate voltage was switched from negative to positive [Fig. 3.4 (e) and (f)]. Upon exchanging the two contacts such that the right contact was grounded and a positive voltage was applied to the left contact, the hot spot again appeared near the grounded side as shown in Fig. 3.4 (g). In the same hole-doped regime, when a negative voltage was applied to the drain, the hot spot shifted to the drain side, as shown in Fig. 3.4 (h).

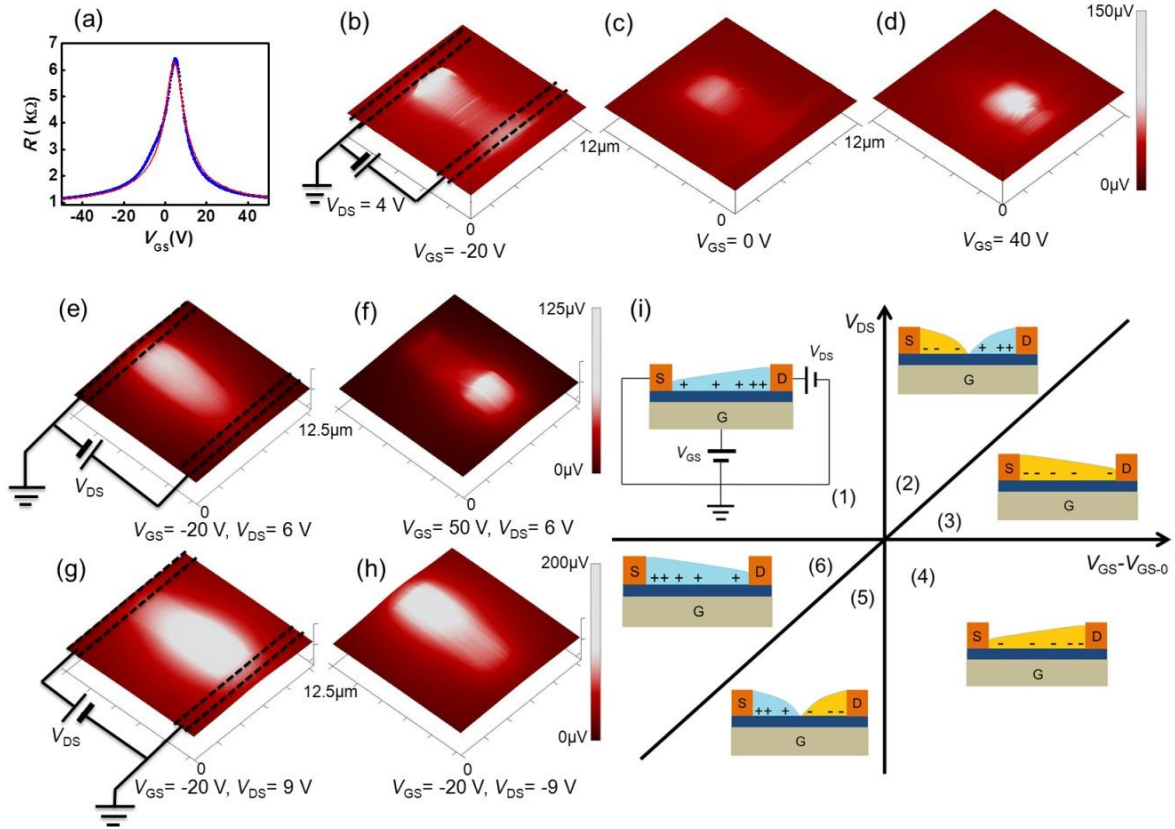


**Figure 3. 4** Thermal mapping of Device 1 and Device 2. (a) Two-probe low-bias resistance (blue line) of Device 1 as a function of the back gate voltage. The red line is the model fitting from which the mobility is extracted. (b-d) SThM thermovoltage maps of Device 1 for a constant drain-source bias ( $V_{DS} = 4$  V) and different gate voltage of -20V, 0V and 40V, respectively. The scan size is  $12 \mu\text{m} \times 12 \mu\text{m}$ . (e-h) SThM thermovoltage maps of Device 2 for different combinations of bias and gate voltages. The electrode connections for (f) and (h) are the same as those shown for (e) and (g), respectively. (i) Schematic illustration of the spatial distribution of the local charge carrier concentration in the graphene channel for different bias and gate voltages. Majority carriers can be either holes (blue +) or electrons (orange -). The source (S) electrode is grounded and the  $V_{DS}$  is applied to the drain (D) electrode.

The origin of the hot spot has been discussed quantitatively in recent reports of infrared emission measurement results,<sup>1, 4</sup> and is explained here by using a series resistance model in the graphene channel. The current density is homogeneous in our two terminal devices with a constant channel width. Hence, the local heating rate is proportional to the local resistivity, with the region of high temperature rise corresponding to the location of high resistivity, which is inversely proportional to the local carrier concentration assuming constant carrier mobility. The local carrier density is controlled by the effective electric potential  $V_{\text{eff}}(x) = V_{\text{GS}} - V_{\text{GS-0}} - V(x)$ , where  $V(x)$  is the local electrochemical potential along the channel. This leads to different regimes of transport depending on the bias and gate voltages as shown in Fig. 3.4 (i). For positive  $V_{\text{DS}}$  and negative  $V_{\text{GS}} - V_{\text{GS-0}}$ , the device is in the unipolar hole-doped regime [Regime 1 in Fig. 3.4 (i)]. The hot spot thus occurs near the grounded source electrode where the hole density is the lowest [Fig. 3.4 (b), (e) and (g)]. For positive  $V_{\text{GS}} - V_{\text{GS-0}}$  and small positive  $V_{\text{DS}}$  ( $< V_{\text{GS}} - V_{\text{GS-0}}$ ), the device is in the unipolar electron-doped regime (Regime 3). Therefore the hot spot appears near the drain contact where the electron density is the lowest [Fig. 3.4 (d) and (f)]. For negative  $V_{\text{GS}} - V_{\text{GS-0}}$ , when  $V_{\text{DS}}$  is switched from positive to negative, the device remains in the hole-doped regime. However, the minimum in the hole density moves from the source to the drain (Regime 6). Hence the hot spot shifts from the source side to the drain side [Fig. 3.4 (h)]. The profile shown in Fig. 3.4 (c) was obtained at zero gate voltage and positive  $V_{\text{DS}}$ , which should correspond to the hole-doped regime, similar to Fig. 3.4 (b). However, the hot spot shows up in the middle of the channel. Since this image was acquired after  $V_{\text{GS}} = -20$  V had been applied for a long time

(~40 minutes) to obtain the image in Fig. 3.4 (b), it is likely that the Dirac point had shifted to slightly negative value due to bias stress effect (see Appendix B). As a result, the device is now in the ambipolar regime (Regime 2), where the hot spot develops at the Dirac point inside the channel.

In order to quantify the acoustic phonon temperature in the graphene, we used a 100  $\mu\text{m}$  long metal line heater and resistance thermometer patterned on the graphene to calibrate the SThM measurement results. The temperature coefficient of the metal line resistance was measured in a variable-temperature stage with a low excitation current. Subsequently, a dc heating current was flown between two wide metal electrodes to the thermometer line [Fig. 3.2 (a)]. The resistance of the metal line was measured in a four-probe configuration, and used to determine the average temperature rise in the metal line at different heating current levels. The temperature rise was measured to be 42 K and 28 K at 18.56 mW and 12.15 mW electrical power dissipations in the heater line, respectively. Since the thermal contact resistance between the tip and the metal line and between the tip and graphene may be different, the calibration performed on the metal line cannot be directly applied to graphene. To this end, a finite element method (FEM) simulation was used to obtain the temperature distribution on the metal line as well as the graphene surface (see Appendix A.2). In the model, the thermal conductivity of the heater line is obtained using the Wiedemann-Franz law based on the measured electrical resistivity of the heater line. The thermal conductivity values of  $\text{SiO}_2$  and the supported graphene are taken to be  $1.3 \text{ Wm}^{-1}\text{K}^{-1}$  and  $600 \text{ Wm}^{-1}\text{K}^{-1}$ , respectively.<sup>11, 16</sup> The calculated average temperature of the metal line is made to match the measurement results using the

resistance thermometry method by adjusting the interface resistance between the metal line and the SiO<sub>2</sub> surface, which is found to be  $1.0 \times 10^{-8} \text{ m}^2\text{KW}^{-1}$ . The value is consistent with the literature values for the metal-dielectric interface resistance and an order of magnitude larger than the interface resistance between SiO<sub>2</sub> and Si substrate.<sup>17-19</sup> We used interface resistance value of  $2.0 \times 10^{-8} \text{ m}^2\text{KW}^{-1}$  found at the Al-graphite interface for the metal-graphene interface resistance,<sup>20</sup> and  $1.0 \times 10^{-8} \text{ m}^2\text{KW}^{-1}$  for the interface resistance between the graphene and the SiO<sub>2</sub> film.<sup>21</sup> These two interface resistances affect the graphene temperature profile close to the metal line, and the temperature of the short metal line segment located on top of graphene, but has little effect on the average temperature of the long metal line.

In order to eliminate the contribution of air conduction to the thermovoltage signals, SThM measurements were conducted in both contact and lift modes on the sample heated using the metal line heater. Figure 1d shows such measurements obtained at the center of the metal heater line. The thermovoltage signal obtained in the lift mode is caused mostly by heat transfer through the air gap between the sample and the probe including both the tip and the cantilever, and is insensitive to the lift height when the lift height is much smaller than the  $\sim 8 \text{ }\mu\text{m}$  height of the tip (see Appendix A).<sup>12</sup> In our measurements, the thermovoltage signal obtained in lift mode at a lift height of 400 nm was subtracted from that obtained in the contact mode. The resultant signal is caused by heat transfer due to low-frequency acoustic phonons through the solid-solid contact and the surrounding liquid meniscus. The ratio of the obtained thermovoltage difference between the two SThM modes over the calculated sample surface temperature is 0.53

$\mu\text{V/K}$  and  $0.63 \pm 0.04 \mu\text{V/K}$  when the tip was on the metal line and graphene, respectively.

With the same contact pressure and lift height as those used in the calibration, the hybrid contact-lift mode SThM measurements were conducted on Device 3 [Fig. 3.5]. From low-bias  $R$  vs.  $V_{\text{GS}}$  measurement, the Dirac point of this sample is located at  $V_{\text{GS}-0} = 16$  V. The SThM measurements were conducted at  $V_{\text{GS}} = 0$  V to prevent any spurious doping due to the gate bias.<sup>1, 22, 23</sup> At  $V_{\text{GS}} = 0$  V, the corresponding Fermi level is determined to be  $-0.135$  eV, so that the majority carriers are holes at a positive  $V_{\text{DS}}$ . Similar to the other samples, the position of the hot spot was found to correspond to the region of low local carrier density. Based on the obtained temperature response ratio of the SThM tip on graphene, the temperature rise in the channel was determined from the difference between the two measured thermovoltage values obtained in the contact and the lift modes. The maximum temperature rise of the low-frequency acoustic phonons in the graphene was found to be  $160$  K at  $V_{\text{DS}} = -6.5$  V, as shown in Fig. 3.5 (c). The average temperature rise of the graphene channel increases linearly with the power density [Fig. 3.5 (e)], calculated as the electrical power divided by the area of the graphene channel. A linear fit to the data yields an equivalent thermal resistance of  $7735 \text{ KW}^{-1}$  for the sample. This resistance value is in good agreement with the sum of the  $7653 \text{ KW}^{-1}$  thermal resistance of the underlying  $300$  nm thick oxide spacer of the same dimension as the graphene, a graphene-SiO<sub>2</sub> interface resistance of  $357 \text{ KW}^{-1}$ ,<sup>21</sup> and a  $608 \text{ KW}^{-1}$  spreading resistance of the Si substrate.<sup>24, 29</sup> In comparison, the thermal

resistance for lateral heat spreading along the graphene is on the order of  $4 \times 10^6 \text{ KW}^{-1}$ , which is much larger than the thermal resistance for heat conduction into the substrate.<sup>28</sup> This comparison suggests that vertical heat dissipation to the  $\text{SiO}_2$  support dominates over lateral heat dissipation to the metal electrode even for these considerably shorter graphene samples than those used in the IR measurements,<sup>1,4</sup> similar to the situation of electrically biased single-walled carbon nanotubes.<sup>13</sup>

Because both of our SThM and Raman measurements were conducted in air, the power density could not be increased to sufficiently high level for the anti-Stoke signal to be observed without sample burn-out.<sup>3</sup> In Fig. 3.5 (f), we have plotted our temperature versus power density results together with literature results obtained using the Raman and thermal emission measurements performed in vacuum and mostly at higher power density.<sup>4-6</sup> Except for the  $1.5 \mu\text{m} \times 0.6 \mu\text{m}$  graphene constriction sample reported in Ref 3, all the data appear to converge onto a single curve, suggesting that the temperatures of different energy carriers measured by different methods are approximately in equilibrium with each other in these relatively large-area graphene samples. Moreover, the temperatures appear to follow a linear dependence on the power density. Because the slope of the curve is equivalent to the thermal resistance per unit area, this convergence suggests that the thermal resistance in these devices is mainly determined by the underlying  $\text{SiO}_2$  spacer due to dominant vertical heat transport. For the graphene constriction sample, the zone-center optical phonon temperature measured by the anti-Stokes to Stokes ratio is considerably higher, and the anharmonic temperature of the G band shift is considerably lower than the fitting to the other data. Besides impurity doping

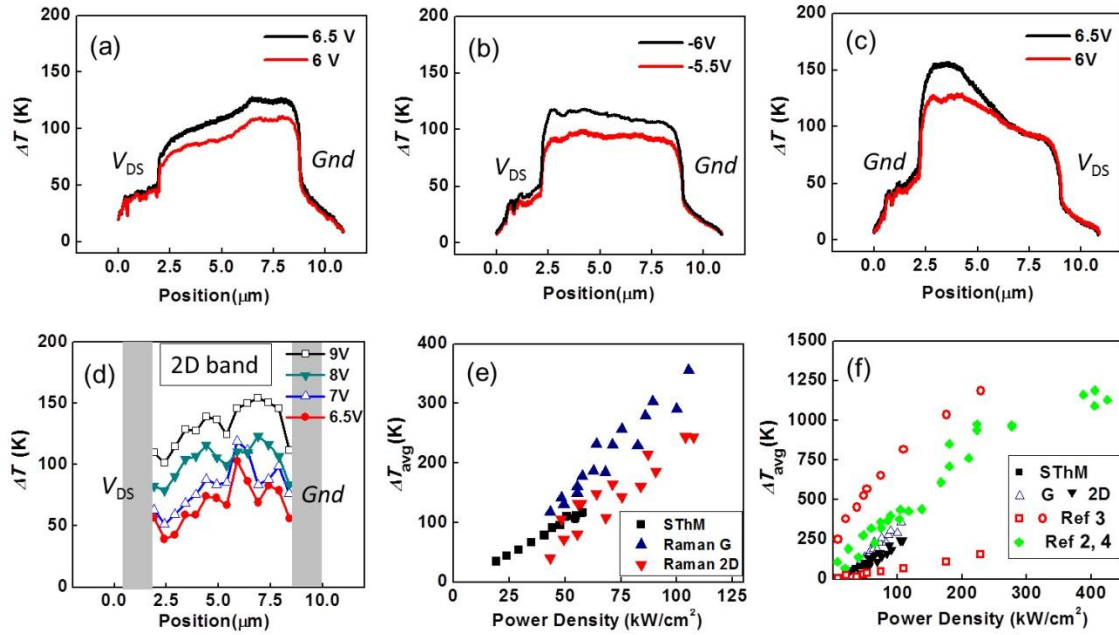


**Figure 3. 5** Comparison of temperatures determined from SThM measurement and Raman measurement. (a-c) Measured SThM temperature profiles in Device 3 at different  $V_{DS}$  values and polarities and  $V_{GS} = 0$  V. (d) Raman 2D band temperature profile measured on the same device at different  $V_{DS}$  values and  $V_{GS} = 0$  V. *Gnd* refers to the ground electrode. The shaded areas indicate the locations of the two electrodes. (e) Average temperature rise in the graphene channel measured by the SThM as well as Raman G and 2D peak shifts as a function of power density. (f) Average temperature rise as a function of power density obtained using SThM (black squares), Raman G band shift (open upper triangles), and 2D band shift (down triangles) from the present work and previous optical measurement results including the Raman G band temperature in Ref 3 (red open squares), the temperature determined from the anti-Stokes/Stokes ratio in Ref 3 (red open circles), and the temperatures measured by using IR emission, Raman 2D and G band shifts, and the anti-Stokes/Stokes ratio in Refs 2 and 4 (green diamonds).

and strain, the lower anharmonic G band temperature in the constriction sample could be caused by the increasing importance of lateral heat dissipation by acoustic phonons from the graphene to the metal electrodes, as well as a relatively smaller spreading thermal resistance component of the Si substrate that scales inversely with the lateral dimension instead of area as for the thermal resistance of the SiO<sub>2</sub> spacer.<sup>25</sup> The presence of hot optical phonons in the constriction also suggests strong electron coupling between the hot electrons and zone-center optical phonons compared to surface polar optical phonon scattering and coupling of optical phonons with lower-energy phonons. The clear observation of hot optical phonons only in the constriction sample deserves further investigation.

### **3.5 SUMMARY**

Our high-spatial resolution SThM measurement results suggest that asymmetric heating due to inhomogeneous charge carrier concentration also occurs in several micron-long graphene channels that are considerably shorter than those observed using IR mapping. By subtracting the signal measured in the lift mode due to parasitic air conduction from that measured in the contact mode, we have obtained the temperature distribution of the low-frequency acoustic phonons in graphene that dominate the heat transfer through the van der Waals contact and the surrounding liquid meniscus. The obtained average temperature of the low-frequency acoustic phonons increases linearly with the power density and is in equilibrium with the anharmonic scattering temperature of Raman 2D phonons measured on the same sample. The slope of the average

temperature rise versus power density curve obtained by SThM at low power density is consistent with those measured using optical techniques in graphene channels of similar or larger sizes at higher power density. This comparison suggests that the different energy carriers in graphene channels larger than several microns in size are in equilibrium, with their average temperature rise close to the power density divided by the thermal resistance per unit area of the underlying SiO<sub>2</sub> layer.

## REFERENCES

1. Bae, M. H.; Ong, Z. Y.; Estrada, D.; Pop, E., *Nano Lett* **2010**, *10*, 4787-4793.
2. Berciaud, S.; Han, M. Y.; Mak, K. F.; Brus, L. E.; Kim, P.; Heinz, T. F., *Phys Rev Lett* **2010**, *104*, 227401.
3. Chae, D. H.; Krauss, B.; von Klitzing, K.; Smet, J. H., *Nano Lett* **2010**, *10*, 466-471.
4. Freitag, M.; Chiu, H. Y.; Steiner, M.; Perebeinos, V.; Avouris, P., *Nat Nanotechnol* **2010**, *5*, 497-501.
5. Freitag, M.; Steiner, M.; Martin, Y.; Perebeinos, V.; Chen, Z. H.; Tsang, J. C.; Avouris, P., *Nano Lett* **2009**, *9*, 1883-1888.
6. Calizo, I.; Miao, F.; Bao, W.; Lau, C. N.; Balandin, A. A., *Appl Phys Lett* **2007**, *91*, 071913.
7. Basko, D. M.; Piscanec, S.; Ferrari, A. C., *Phys Rev B* **2009**, *80*, 165413.
8. Bonini, N.; Lazzeri, M.; Marzari, N.; Mauri, F., *Phys Rev Lett* **2007**, *99*, 176802.
9. Das, A.; Pisana, S.; Chakraborty, B.; Piscanec, S.; Saha, S. K.; Waghmare, U. V.; Novoselov, K. S.; Krishnamurthy, H. R.; Geim, A. K.; Ferrari, A. C.; Sood, A. K., *Nat Nanotechnol* **2008**, *3*, 210-215.
10. Prasher, R., *Appl Phys Lett* **2009**, *94*, 041905.
11. Seol, J. H.; Jo, I.; Moore, A. L.; Lindsay, L.; Aitken, Z. H.; Pettes, M. T.; Li, X. S.; Yao, Z.; Huang, R.; Broido, D.; Mingo, N.; Ruoff, R. S.; Shi, L., *Science* **2010**, *328*, 213-216.

12. Shi, L.; Majumdar, A., *J Heat Trans-T Asme* **2002**, *124*, 329-337.
13. Shi, L.; Zhou, J. H.; Kim, P.; Bachtold, A.; Majumdar, A.; McEuen, P. L., *J Appl Phys* **2009**, *105*, 104306.
14. Kim, K.; Jeong, W. H.; Lee, W. C.; Reddy, P., *Acs Nano* **2012**, *6*, 4248-4257.
15. Kim, S.; Nah, J.; Jo, I.; Shahrjerdi, D.; Colombo, L.; Yao, Z.; Tutuc, E.; Banerjee, S. K., *Appl Phys Lett* **2009**, *94*, 062107.
16. Cahill, D. G.; Bullen, A.; Lee, S. M., *High Temp-High Press* **2000**, *32*, 135-142.
17. Kading, O. W.; Skurk, H.; Goodson, K. E., *Appl Phys Lett* **1994**, *65*, 1629-1631.
18. Kim, J. H.; Feldman, A.; Novotny, D., *J Appl Phys* **1999**, *86*, 3959-3963.
19. Yamane, T.; Nagai, N.; Katayama, S.; Todoki, M., *J Appl Phys* **2002**, *91*, 9772-9776.
20. Schmidt, A. J.; Chen, X. Y.; Chen, G., *Rev Sci Instrum* **2008**, *79*, 114902.
21. Chen, Z.; Jang, W.; Bao, W.; Lau, C. N.; Dames, C., *Appl Phys Lett* **2009**, *95*, 161910.
22. Lafkioti, M.; Krauss, B.; Lohmann, T.; Zschieschang, U.; Klauk, H.; von Klitzing, K.; Smet, J. H., *Nano Lett* **2010**, *10*, 1149-1153.
23. Zilker, S. J.; Detcherry, C.; Cantatore, E.; de Leeuw, D. M., *Appl Phys Lett* **2001**, *79*, 1124-1126.
24. Asheghi, M.; Kurabayashi, K.; Kasnavi, R.; Goodson, K. E., *J Appl Phys* **2002**, *91*, 5079-5088.
25. The thermal resistance of the SiO<sub>2</sub> spacer between the graphene and the Si substrate is estimated as  $R_{SiO_2} \approx t_{SiO_2}/\kappa_{SiO_2}WL$ , where  $t_{SiO_2} = 300$  nm and  $\kappa_{SiO_2}$

are the thickness and the thermal conductivity of the SiO<sub>2</sub> film, respectively, and  $W$  and  $L$  are the width and length of the graphene channel, respectively. The spreading thermal resistance of the Si substrate is calculated as  $R_{Si} \approx 1/2\kappa_{Si}(WL)^{1/2}$  where  $\kappa_{Si}$  is the thermal conductivity of the silicon substrate. The thermal resistance for lateral heat spreading from the graphene to the metal electrodes is estimated as  $R_g \approx L/2\kappa_g Wt$ , where  $\kappa_g$  and  $t$  are the thermal conductivity and thickness of the supported graphene.

## Chapter 4. Thermal Conductivity Measurements of Suspended Graphene

### 4.1 INTRODUCTION

The thermal conductivity ( $\kappa$ ) of suspended graphene was reported to be 3000-5000  $\text{Wm}^{-1}\text{K}^{-1}$  at room temperature based on micro-Raman thermometry.<sup>1,2</sup> By contrast, supported graphene and suspended bilayer graphene measured with resistance thermometer devices showed room temperature  $\kappa$  around 600  $\text{Wm}^{-1}\text{K}^{-1}$ ,<sup>3</sup> while bi- and 7 layer graphene samples encased with  $\text{SiO}_2$  on both sides were measured by using heat spreader method to be 50 and 420  $\text{Wm}^{-1}\text{K}^{-1}$ , respectively.<sup>4</sup> It was also found that phonon scattering by polymer residue on suspended bilayer graphene reduces the  $\kappa$  of the bi-layer graphene.

Existing Raman-based thermometry methods for graphene measurements suffer from low temperature sensitivity and cannot obtain the low-temperature thermal transport properties. In addition, laser heating used in the Raman thermometry may result in local non-equilibrium temperatures of optical and acoustic phonons.<sup>5</sup> Hence, alternative experimental methods are needed to probe phonon transport in graphene. One of the methods is based on micro bridge devices with built-in resistance thermometers. However, one challenge in such measurements is the transfer of graphene onto the micro-bridge device.

This chapter describes an efficient method to transfer suspended graphene onto micro-bridge device for thermal measurements. A PMMA film is used as the carrier layer for the transfer process. This high-yield transfer method has been used to prepare

graphene samples with different layer thickness for  $\kappa$  measurements. In contrast with theoretical prediction for suspended clean graphene samples, the experimental data shows a general trend of increasing  $\kappa$  with increasing layer thickness. This trend is attributed to increasing scattering of phonons in thinner graphene samples by polymer residues on the graphene surface.

## 4.2 SAMPLE PREPARATION

Suspended graphene samples have been prepared with the PMMA assisted transfer technique as demonstrated in Fig. 4.1. The micro-bridge device shown in (e) is modified from an earlier design for thermal transport measurements of supported graphene.<sup>6</sup> The current design consists of a suspended structure fabricated from a 500-nm-thick SiN<sub>x</sub> film, on which four 10/70-nm-thick Cr/Pt metal lines are patterned. The graphene sample was transferred and suspended onto the central rectangular frame made of SiN<sub>x</sub> beams according to the procedure shown in Fig. 4.1 (a-d). In this procedure, graphene was first exfoliated from bulk graphite source onto a silicon substrate covered with about 290 nm thick thermal oxide, which provides sufficient optical contrast for identifying few-layer graphene [Fig. 4.1 (a)]. After a PMMA layer was spin coated on the sample and patterned with the use of electron beam lithography (EBL), the exposed region of the graphene flake was etched by O<sub>2</sub> plasma to form a rectangular shape. Subsequently, EBL and metal lift-off process were used to deposit Au registration marks around the patterned h-BN [Fig.4.1 (b)]. A ~1.5  $\mu\text{m}$  thick PMMA film was then spin coated onto the substrate. After the sample was placed in 1% hydrofluoric acid solution,

the interface oxide was etched so that the PMMA layer was detached from the substrate. The graphene sample and the gold alignment marks were attached to the PMMA film that floated on top of the solution. Upon thorough rinsing with deionized water, the PMMA film was manually aligned to the micro-bridge device in an aqueous environment under an optical microscope [Fig.4.1 (c,f)]. After the deionized water was evaporated, we used EBL to expose parts of the suspended PMMA layer and developed the PMMA layer in MIBK:IPA(3:1) for 1 minute to open windows in the PMMA layer. A 5nm/30nm thick Cr/Au layer was deposited on the PMMA layer. Subsequently, the PMMA layer was dissolved in acetone, rinsed and dried in warm acetone at about 60 °C. This process yielded a graphene sample suspended by the central rectangular SiN<sub>x</sub> frame of the micro-bridge device. The two ends of the graphene sample is sandwiched between a Cr/Au layer on top and the Pt resistance thermometer line on the bottom, as shown in Fig. 4.1 (g). Because the additional EBL and metal deposition process to deposit the top Cr/Au sample can decrease the yield of this transfer method, some of the graphene samples were transferred onto the device without an Cr/Au metal deposited on top of the two ends.

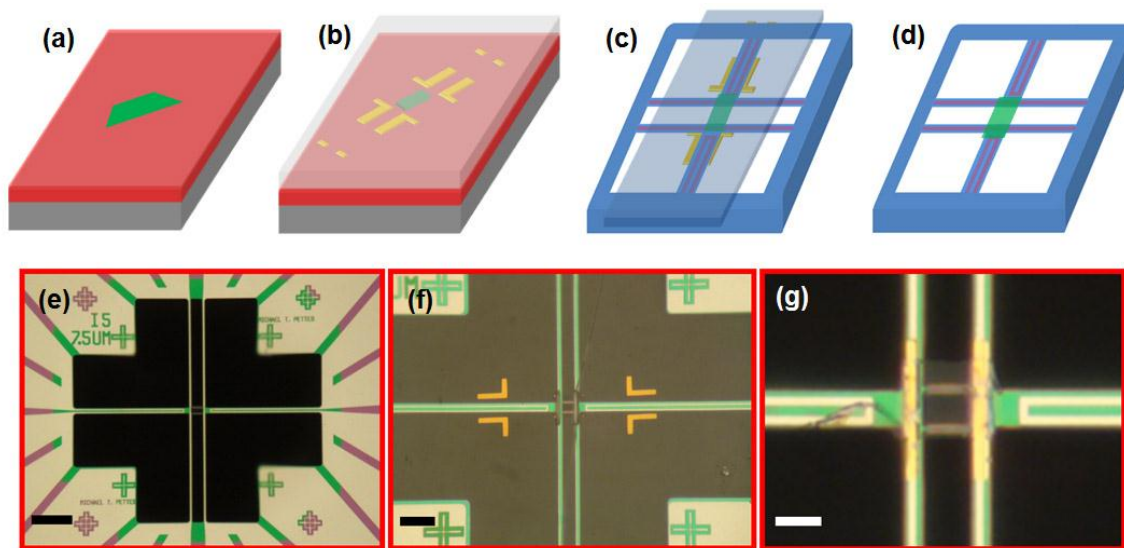


**Figure 4. 1** Transfer of exfoliated graphene over a micro-bridge device. The top row consists of schematics showing (a) graphene (green) exfoliated on top of a Si substrate (gray) covered by thermal oxide (red), (b) Au registration marks (golden) on the substrate and a PMMA layer (semi-transparent) covering the patterned graphene ribbon, (c) the PMMA carrier layer transferred on top of the micro-bridge device (blue), (d) graphene samples suspended on the central SiNx frame of the micro-device after the dissolution of the PMMA layer. The bottom row consists of optical micrographs showing (e) the micro-bridge device, (f) PMMA layer aligned on the device after two windows were open in the PMMA layer via EBL and developing, and (g) a graphene sample suspended on the device after dissolving of the PMMA layer and dried in warm acetone. The scale bars represent 25, 10, 5 $\mu\text{m}$  in (e-g)

It is well known that it is difficult to remove PMMA residue completely from the graphene surface.<sup>7-10</sup> Thermal annealing in a hydrogen and argon environment above 340 °C has been used to remove the residues from graphene devices<sup>11, 12</sup>, however, doping by remnant molecules after annealing often led to degraded electron transport characteristics.<sup>7, 12, 13</sup> Recent studies TEM have shown that PMMA residues can be

burned off more easily with oxygen in air<sup>7, 14</sup> at elevated temperatures of 250-350 °C. In this work, some of the transferred graphene samples were annealed in air at 300°C for 3 hours.

The devices were placed wire-bonded to a chip carrier before being installed in the high-vacuum sample space of a variant temperature cryostat. The measurements have been performed at a temperature range between 45K and 450K. After the thermal measurement, Raman spectroscopy was used to determine the thickness of single and bi-layer graphene, and to characterize defects via the Raman D peak intensity. TEM has been used to further confirm the layer thickness, to determine the crystallographic orientation of the graphene samples, and to examine whether polymer residue remains on the graphene surface.

### 4.3 THERMAL MEASUREMENT METHOD

Figure 4.2 (a) shows a false color SEM image of a sample suspended over a micro-bridge device with the heat flow diagram and the mid-point temperatures of the four resistance thermometer (RT) lines. The left horizontal RT, RT<sub>1</sub>, is Joule-heated with an electrical power  $Q$ . Part of the heating,  $Q_1$ , is transferred by conduction through the other three suspended beams to the substrate kept at temperature  $T_0$ . The resistance change of the RTs is used to determine the average temperature rises in the four RTs ( $\overline{\Delta T_j}; j=1,2,3,4$ ), which is further used to determine the local temperature rises

(  $\Delta T_{j,m}(x)$ ;  $j=1,2,3,4$  ) at the middle of the four thermometer lines based on the temperature distribution in each suspended beam.

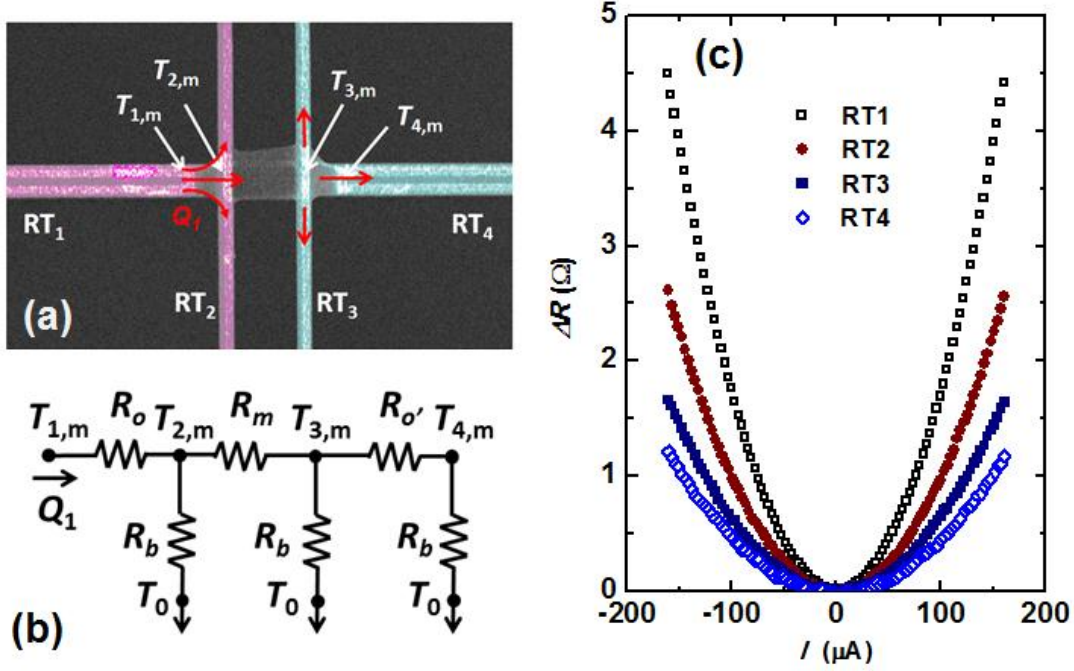


**Figure 4.2** (a) Heat conduction diagram in a suspended device. The four suspended resistance thermometer lines are indicated by  $RT_j$ ,  $j=1, 2, 3, 4$ .  $RT_1$  is heated by a DC current  $I$  to cause heat transfer along the suspended graphene sample. (b) Equivalent thermal circuit of the device (c) Resistance changes of the four RTs as a function of the DC heating current  $I$  through  $RT_1$ .

Steady-state heat conduction in each of the four suspended RT lines is described by the following one-dimensional heat conduction equation,

$$\frac{d^2 T(x)}{dx^2} + \frac{q}{\kappa} = 0 \quad (4.1)$$

where  $\kappa$  and  $q$  are the equivalent thermal conductivity and the volumetric heat generation rate in each RT line. For RT<sub>2</sub>, RT<sub>3</sub>, and RT<sub>4</sub>,  $q = 0$ , and the temperature distribution in the suspended beam is linear so that

$$T_j(x) = \frac{T_j(L) - T_0}{L} x + T_0 \quad (L \geq x \geq 0) \quad (4.2)$$

where  $L$  is the distance between the midpoint and one end of the suspended RT line, and  $x$  is measured from one end of the suspended beam. Thus, the mid-point temperature rise is twice the average temperature rise,

$$\Delta T_{j,m} \equiv T_{j,m} - T_0 = 2\overline{\Delta T_j}; \quad j = 2,3,4. \quad (4.3)$$

For RT<sub>1</sub>,  $q = Q/AL$ , where  $A$  is the cross section area of RT<sub>1</sub>. The temperature distribution along RT<sub>1</sub> is described by the following parabolic relation

$$\Delta T_1(x) \equiv T_1(x) - T_0 = -\frac{Q}{2\kappa_b LA} x^2 + C_1 x + C_2 \quad (4.4)$$

where  $C_1$  and  $C_2$  are two constants.

The boundary condition for  $\Delta T_1(x=0) = 0$  and  $\Delta T_1(x=L) = \Delta T_1$  gives

$$\Delta T_1(x) = -\frac{Q}{2\kappa_b LA} x^2 + \left( \frac{\Delta T_{1,m}}{L} + \frac{R_b Q}{2L} \right) x \quad (4.5)$$

where  $R_b \equiv L/\kappa_b A$  is the thermal resistance between the midpoint of the RT and the substrate, and is designed to be the same for all the four RT lines.

The rate of heat transfer  $Q_I$  from RT<sub>1</sub> to the other three RT lines equals the total heat transfer from RT<sub>2</sub>, RT<sub>3</sub>, and RT<sub>4</sub> to the substrate, i.e.

$$Q_1 = -\kappa_b A \frac{d\Delta T_1(x)}{dx} \Big|_{x=L} = \frac{\Delta T_{2,m} + \Delta T_{3,m} + \Delta T_{4,m}}{R_b} \quad (4.6)$$

In addition, the rate of heat transfer  $Q_0$  from  $RT_1$  directly to the environment is obtained

as

$$Q_0 = \kappa_b A \frac{d\Delta T_1(x)}{dx} \Big|_{x=0} = \kappa_b A \left[ \frac{\Delta T_{1,m}}{L} + \frac{R_b Q}{2L} \right] = \frac{\Delta T_{1,m}}{R_b} + \frac{Q}{2} = Q - Q_1 \quad (4.7)$$

Hence,

$$R_b = 2 \frac{\Delta T_{1,m} + \Delta T_{2,m} + \Delta T_{3,m} + \Delta T_{4,m}}{Q} \quad (4.8)$$

Using Eq.(4.5) and (4.8), the measured average temperature rise in  $RT_1$  is expressed as

$$\overline{\Delta T_1} = \frac{1}{L} \int_0^L \Delta T_1(x) dx = \frac{4\Delta T_{1,m} + \Delta T_{2,m} + \Delta T_{3,m} + \Delta T_{4,m}}{6} \quad (4.9)$$

Thus,

$$\Delta T_{1,m} = \frac{3}{2} \overline{\Delta T_1} - \frac{1}{2} (\overline{\Delta T_2} + \overline{\Delta T_3} + \overline{\Delta T_4}) \quad (4.10)$$

Based on the thermal circuit shown in Fig.4.2 (b), the heat transfer through  $R_m$  is equal to the heat transfer through  $RT_3$  and  $RT_4$ , so that

$$\frac{R_m}{R_b} = \frac{\Delta T_{2,m} - \Delta T_{3,m}}{\Delta T_{3,m} + \Delta T_{4,m}} \quad (4.11)$$

Therefore, the thermal resistance of the suspended graphene and the two underlying  $\text{SiN}_x$  bars is

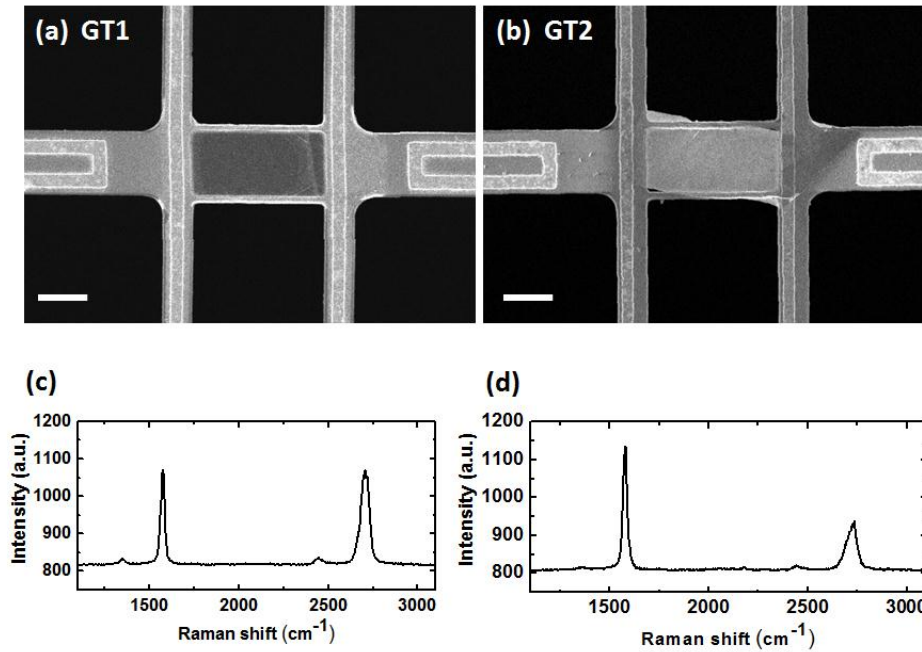
$$R_m = 2 \frac{\Delta T_{2,m} - \Delta T_{3,m}}{\Delta T_{3,m} + \Delta T_{4,m}} \frac{(\Delta T_{1,m} + \Delta T_{2,m} + \Delta T_{3,m} + \Delta T_{4,m})}{Q} \quad (4.12)$$

Figure 4.2(c) shows the resistance changes for the four RTs as a function of the heating current  $I$  in RT<sub>1</sub>. The current was ramped from 0 to negative maximum, then to positive maximum, and back to zero. During the ramping cycle, a total of 203 measurements were taken at equal intervals of  $I$ . At each  $I$ , the data was taken after 3 second delay time to reach a steady state. The average resistance change is used to obtain the local temperature rise based on Eq. (4.3) and (4.10). Finally, the thermal conductance of the sample,  $G_m \equiv I/R_m$ , is calculated by using Eq. (4.12).

#### 4.4 RESULTS

Figures 4.3 (a-b) show SEM images of two suspended graphene samples after thermal measurements (denoted as GT1 and GT2). The suspended length of both samples is same as the horizontal dimension of the frame structure in the middle, i.e. 7.5  $\mu\text{m}$ . The distance between the two SiN<sub>x</sub> bars under the graphene is 3.5  $\mu\text{m}$ , which is smaller than the 5  $\mu\text{m}$  patterned width ( $w$ ) of the graphene ribbon transferred on top of the two bars. Micro-Raman spectroscopy with 488 nm laser excitation of GT1 shows bi-layer signatures, such as a similar G band and 2D band intensities,  $I_G/I_{2D}=1$ , and 2D band full width at half maximum (FWHM) of about 52  $\text{cm}^{-1}$ .<sup>15</sup> Although the FWHM of the 2D band in suspended bilayer graphene was measured to be as small as 17  $\text{cm}^{-1}$ , similar FWHM  $\sim$  55  $\text{cm}^{-1}$  to our result was observed in a supported bilayer graphene measured by

using a laser wavelength of 488 nm. For GT2, a large G band to 2D band intensity ratio,  $I_G/I_{2D}=2.6$ , and a large 2D band FWHM of  $57\text{ cm}^{-1}$ , indicate a thicker graphene sample. The Raman spectra of Fig 4.3 (c-d) show a clear difference between two samples. First, a small defect-related D band appears at  $1354.7\text{ cm}^{-1}$  in GT1 with an intensity ratio of  $I_D/I_G=0.07$ , but it is absent in GT2. Although the Raman spectrum for GT1 is obtained at the central area of the sample with a  $1\mu\text{m}$  laser aperture, the structural defect observed near  $RT_3$  in the SEM image (a) is likely responsible for the small D peak in the bilayer graphene. In addition, it has been known that anisotropic strain in graphene can result in the splitting of the G band.<sup>16</sup> Absence of the signature in both samples indicates that the strain in the suspended graphene is not large.



**Figure 4.3** SEM images of two suspended graphene samples measured with micro-bridge devices. (a) GT1 is determined to be bilayer graphene from micro-Raman spectroscopy and (b) GT2 is 7 layer graphene determined by TEM images shown in Fig. 4.4. (c-d) Raman spectra of GT1(c) and GT2 (d) with 488 nm laser excitation. The scale bars in (a-b) indicate 2 $\mu$ m.

Sample GT2 was subsequently characterized by using TEM (FEI Tecnai G2 F20) at a 120 kV accelerating voltage. Figure 4.4 (a) shows the selected area electron diffraction (SAED) pattern from a 4.2  $\mu$ m diameter region in the center of the GT2 sample. The crystallographic orientation and a single hexagon of Bragg reflection peaks suggest that the entire sample is likely a single crystal and the stacking order of the graphitic layers is likely to be ABA or Bernal stacking. Figure 4.4 (b) is a low magnification TEM image of the suspended graphene over the central frame of the micro-bridge device, showing no apparent structural defect. Figure 4.4 (c-f) show phase

contrast TEM images that can resolve a thin layer of polymeric residue remaining on the surface. Although some areas of the suspended GT2 are atomically clean as shown in Fig. 4.4 (c), most of the surface shows the similar polymer residue that was observed previously in suspended bilayer graphene as shown in Fig. 4.4 (d-f). Thus thermal annealing under oxygen atmosphere was not effective to completely remove the polymer induced during the transfer process. The high resolution TEM micrographs shown in (e) and (f) can be used to clearly count the number of layers to be 7.

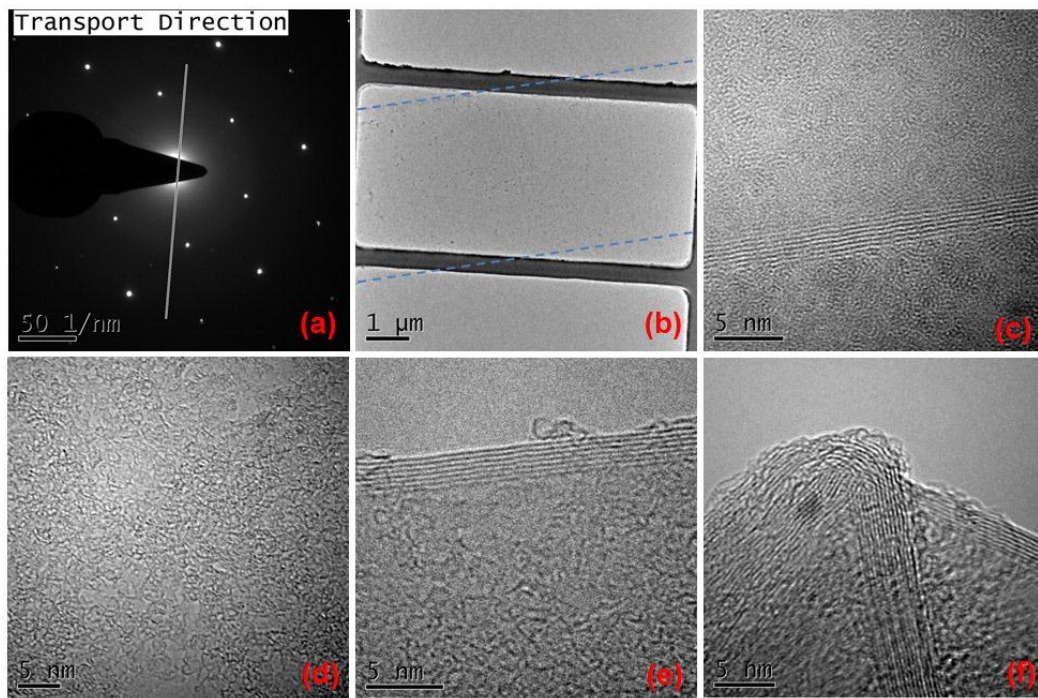


**Figure 4. 4** TEM images obtained with GT2 after thermal measurement. (a) Selected area electron diffraction (SAED) pattern from a 4.25  $\mu\text{m}$  diameter region in the center of the sample. The crystal orientation with respect to the heat transport direction is determined. (b) Low magnification TEM image showing the graphene suspended over the micro-bridge structure. The two dash lines are used to indicate the edges of the suspended graphene. (c) Clean area of suspended graphene (d) Polymer residue covering the large area of the sample (e) The fringe image on the edge of the sample showing 7 graphitic layers. (f) Folded edge with a thin layer of polymer residue.

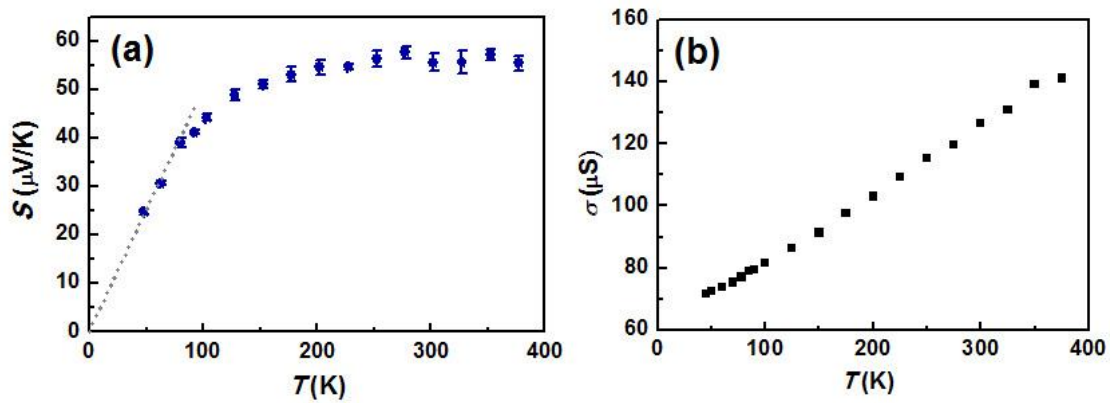


**Figure 4. 5** (a) Seebeck coefficient and (b) Electrical conductivity measured in bilayer GT1. Dotted line in (a) shows Mott relations at Fermi energy ( $E_f$ ) = 31meV.

Because of the electrical contact of graphene with the two straight Pt/Cr thermometer lines, the Seebeck coefficient and the electrical resistance can also be measured. Figure 4.5 (a-b) shows the Seebeck coefficients and two-probe electrical conductivity of GT1 at various temperatures. The Seebeck coefficient of GT1 at room temperature was measured to be  $55.6 \pm 1.8 \mu\text{V/K}$ , indicative of hole-doped graphene. The temperature dependence above 100 K deviates from the linearity expected from the Mott relation for a metal. The reported Seebeck coefficient in a supported bilayer graphene with a high carrier density follows the Mott relation.<sup>17</sup> However, when the Fermi level is near the charge neutral point, the Seebeck coefficient deviates from the linear temperature dependence above 100 K. The linear fit shown in Fig. 4.5 (a) is the thermopower calculation result based on the Mott relation with a Fermi energy  $E_f = 31$  meV measured from the charge neutral point. Moreover, the increasing electrical

conductivity with increasing temperature indicates that the Fermi level of GT1 sample is close to the charge neutral point of the parabolic band.<sup>17</sup>

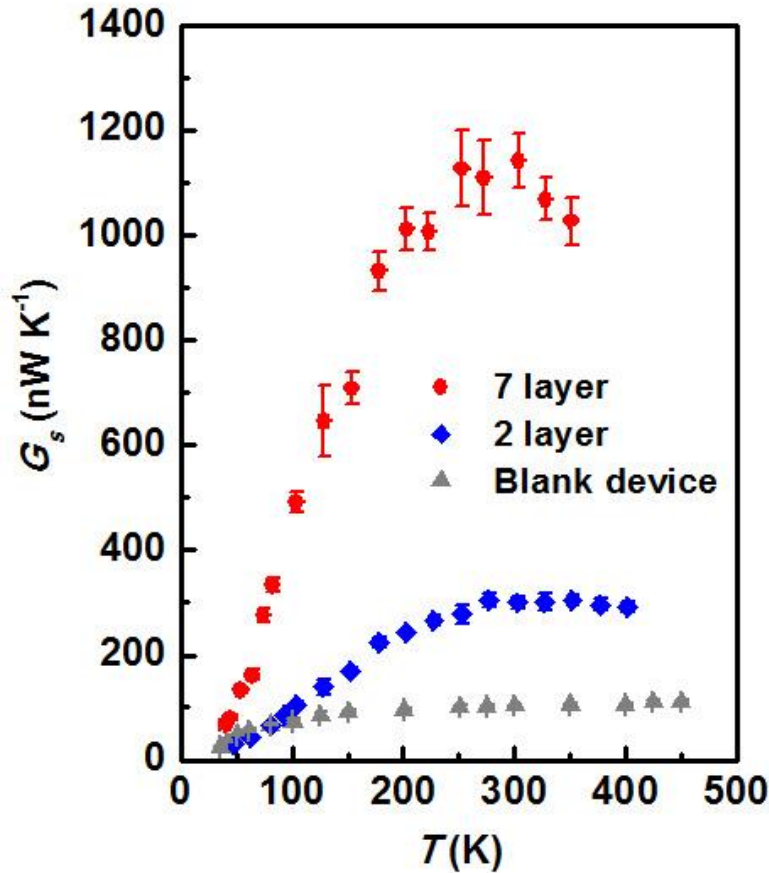


**Figure 4. 6** Measured thermal conductance of suspended graphene, GT1(blue diamond) and GT2(red circle), together with a blank device(grey triangle) of the same geometry used for GT1 and GT2.

The thermal conductance of the suspended graphene samples as well as the blank device was measured in a temperature range between 45 K and up to 450 K, as shown in Fig. 4.6. The thermal conductance of the blank device is mainly due to the heat conduction through the two narrow supporting bars made of SiN<sub>x</sub>. The thermal

conductance of the graphene sample,  $G_s$  in Fig. 4.6, is obtained after the subtraction of the contribution from the  $\text{SiN}_x$  bars from the measured conductance,  $G_m$ . The relative thermal conductance contribution from the  $\text{SiN}_x$  bars is in the range of 25-58 % and 8-30 % of the measured conductance values for GT1 and GT2, respectively, with the upper limit found at low temperatures.

The measured thermal resistance of the sample consists of both the diffusive thermal resistance of the suspended graphene and the contact thermal resistance at its two ends. In a recent experiment performed in suspended h-BN, the contribution of the thermal contact resistance at room temperature was estimated to be about 8% of the sample with a similar  $G_s$  as that of GT2 (Refer to Chapter 5). If we assume the same thermal contact resistance as in the graphene samples as in h-BN, ignoring the thermal contact resistance can underestimate the room temperature  $\kappa$  up to 8% for GT2 and only 3% for GT1.

The  $\kappa$  values shown in Fig. 4.7 are obtained as  $\kappa = G_s L / wt$ , where  $L$  and  $w$  are the length and width of the suspended segment, and  $t$  is the thickness of few-layer graphene. The room temperature  $\kappa$  was measured to be  $672 \pm 28$  and  $724 \pm 35 \text{ Wm}^{-1}\text{K}^{-1}$  for GT1 and GT2, respectively. These values are about a factor of 3 lower than the basal plane values reported for highly oriented pyrolytic graphite (HOPG). The peak values for both samples appear at 300K, above which the  $\kappa$  value decreases due to Umklapp phonon-phonon scattering. In comparison, the peak  $\kappa$  occurs between 100 and 200 K in HOPG.

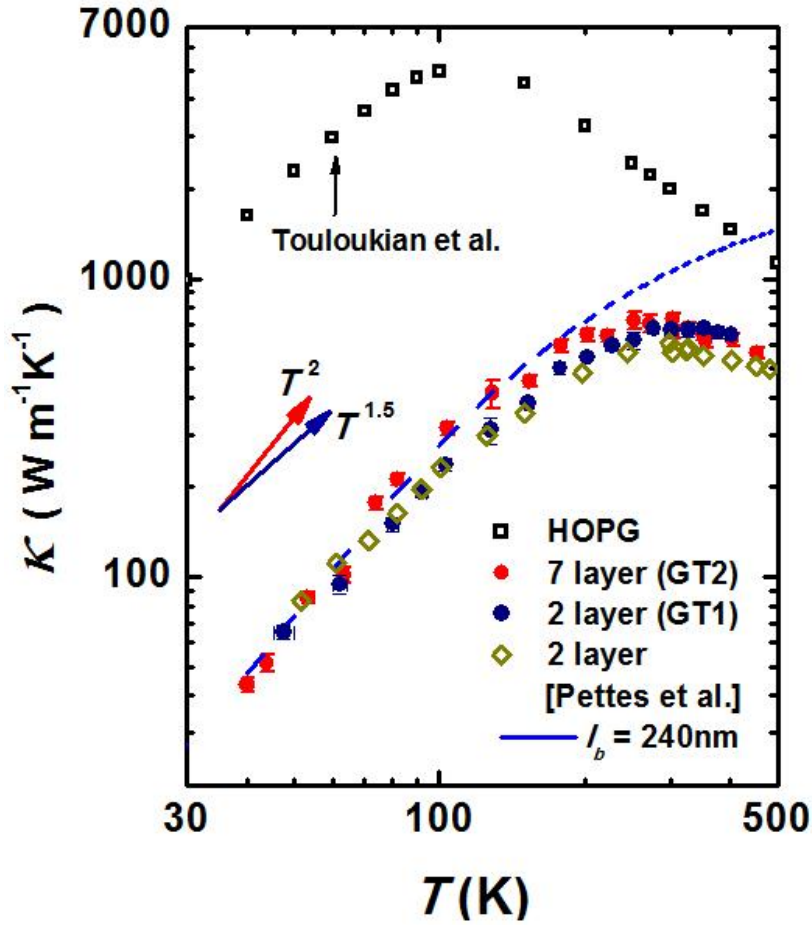


**Figure 4.** 7 Measured  $\kappa$  of bi-layer (navy circle) and 7-layer (red circle) suspended graphene. Also shown for comparison are the reported data for suspended bilayer graphene<sup>3</sup> (open diamond) measured by a different micro-resistance thermometer device, and bulk graphite  $\kappa$  from Touloukian et al.<sup>18</sup> The blue dashed line is the calculation result for a 240 nm boundary scattering mean free path. Red and navy arrow line represents  $T^2$  and  $T^{1.5}$  dependence, respectively.

The  $\kappa$  of few-layer graphene can be calculated using a solution of the phonon Boltzmann transport equation as

$$\kappa = \frac{1}{4\delta} \sum_p \int_{\omega=0}^{\omega_{\max}} v_p^2 \tau_p D_p(\omega) \hbar \omega \frac{d \langle n \rangle}{dT} d\omega \quad (4.13)$$

where  $p$  indicates phonon polarization,  $v_p$  is group velocity,  $\tau_p$  is scattering time,  $D_p(\omega)$  is density of states,  $\langle n \rangle$  is the Bose-Einstein distribution. The summation is over the different phonon polarizations. The phonon dispersion relation of graphite obtained from *ab initio* calculation based on local density approximation is used. The six low frequency phonon branches in a unit cell shown in Fig. 1.4 are considered in the  $\kappa$  calculation. Two types of scattering terms, i.e. isotope defect, boundary scattering, are taken into account to the calculation. First, when the edge scattering with a constant  $l_b$  is the dominant scattering mechanism at low temperatures, the scattering time is expressed as  $\tau_p \approx l_b/v_p$ . Secondly, the isotope of 98.9%  $^{12}\text{C}$  and 1.1%  $^{13}\text{C}$  in a naturally abundant graphite is taken into account according to

$$\tau_{D,p}^{-1}(\omega) = \frac{S_0 \Gamma}{4} \frac{k_p(\omega)}{v_p} \omega_p^2 \quad (4.14)$$

where  $S_0$  is the cross-sectional area per atom, and  $\Gamma$  is the strength of the point defect scattering, which can be calculated by  $\Gamma = \sum_i f_i \left(1 - \frac{M_i}{\bar{M}}\right)^2 = 7.59 \times 10^{-5}$ , where  $f_i$  is the fractional concentration,  $M_i$  is the mass of the impurity, and  $\bar{M}$  is the average atomic mass of C.

By considering both isotope defect and boundary scattering with the use of Matthiessen's rule,  $\tau_{tot}^{-1} = \sum \tau^{-1}$ , we evaluated the Eq. (4.13) to match measurement results of GT2 at low temperatures.

Figure 4.7 shows the  $\kappa$  values measured in this study as well as suspended bilayer graphene from Ref 3 and high quality bulk graphite adopted from Ref 18. The blue dashed line illustrates the result of the model calculation using Eq. (4.13) with a  $l_b = 240\text{nm}$ . Bilayer GT1 shows approximately  $T^{1.5}$  temperature dependence between 50 and 125K, similar to two suspended bilayer graphene in Ref 3. On the other hand, the bulk graphite indicated in Fig. 4.7 shows  $T^2$  dependence. Because similar  $\kappa$  values are observed and the same PMMA layer is used during the transfer process in both experiments, the polymer residue is expected to play a similar role in reducing  $\kappa$  of GT1.

When polymer residue remains on the surface of the suspended graphene, its impact on suppressing  $\kappa$  may vary for samples with different thicknesses. Because of the large portion of surface area to volume in thin layer system, the impact of phonon scattering occurring at the polymer-graphene interface can increase significantly when the thickness decreases. For bulk crystals, on the other hand, the measured samples are typically hundreds of micrometers thick,<sup>19</sup> thus the surface effect is negligible.

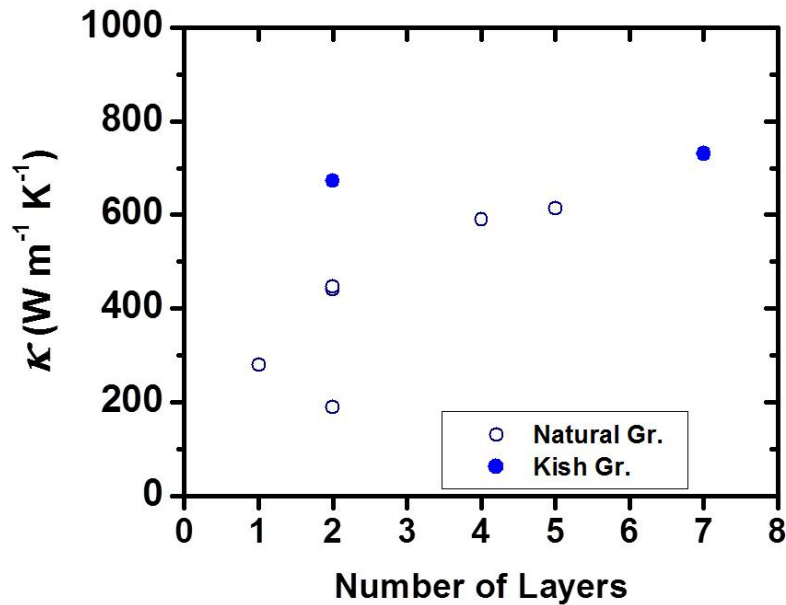


**Figure 4. 8** Measured room temperature  $\kappa$  values of suspended graphene with different thicknesses. Navy empty circles represent graphene samples prepared from natural graphite while blue filled circles represent samples prepared from Kish graphite.

Figure 4.8 (a) shows the measured room-temperature  $\kappa$  of different samples as a function of the layer thickness. The thicknesses of the single and bi-layer graphene are determined by Raman spectroscopy, and 7 layer sample thickness is determined by TEM. The samples with 4-5 atomic layers are determined from optical contrast analysis based on Ref 20. In Fig. 4.8 (a), the  $\kappa$  of single-layer graphene is observed to be  $\sim 280 \text{ W m}^{-1} \text{K}^{-1}$ , and the sample shows no significant Raman D peak associated with the structural defect. In four bi-layer graphene samples, the measured  $\kappa$  values scatter between 200 and 670  $\text{W m}^{-1} \text{K}^{-1}$ . Note that two bi-layer samples show a similar  $\kappa \sim 445 \text{ W m}^{-1} \text{K}^{-1}$ . A general trend of increasing  $\kappa$  with the thickness can be observed in the measurement results for the 8

suspended graphene samples shown in Fig. 4.8, although the plot shows a considerable data scattering for bilayer samples. In addition, the Raman spectra of the bilayer sample with  $\kappa \sim 190 \text{ Wm}^{-1}\text{K}^{-1}$  shows no D peak and one of the bilayer samples with  $\kappa \sim 445 \text{ Wm}^{-1}\text{K}^{-1}$  shows a smaller D peak ( $I_D/I_G = 0.04$ ) than that of GT1 sample,  $I_D/I_G = 0.07$ , although the highest  $\kappa$  in these bi-layer samples was found in GT1. Therefore, the data scattering shown for the bi-layer samples is not related with the D peak intensity that is caused by point defects, except that the two samples prepared from Kish graphite show a slightly higher  $\kappa$  than the others from natural graphite.

#### 4.5 DISCUSSION

The measured  $\kappa$  values in suspended bi- (GT1) and 7 (GT2) layer graphene using a micro-bridge device show about 60% suppression compared to high quality bulk graphite at room temperature. The similar suppression has been reported in supported single layer graphene and suspended bilayer graphene. The  $\kappa$  of graphene supported on  $\text{SiO}_2$  has been measured to be around  $579 \pm 34 \text{ Wm}^{-1}\text{K}^{-1}$  at room temperature, while two suspended bilayer graphene reported by Pettes et al.<sup>3</sup> showed  $560 \pm 70 \text{ Wm}^{-1}\text{K}^{-1}$  and  $620 \pm 80 \text{ Wm}^{-1}\text{K}^{-1}$ . These values are similar to  $672 \pm 28 \text{ Wm}^{-1}\text{K}^{-1}$  measured in GT1 (bilayer) sample. The measured room temperature value in GT2 (7 layer) sample,  $724 \pm 35 \text{ Wm}^{-1}\text{K}^{-1}$  is slightly higher than others. In addition, there exhibits a general trend of increasing  $\kappa$  with increasing layer thickness of these suspended graphene samples contaminated by polymer residue.

Although the underlying mechanism in the reduction of  $\kappa$  is not exactly the same for suspended, supported, and encased graphene, the role of interface scattering at the graphene surface is responsible for the observations. Lindsay et al.<sup>21</sup> have shown that out-of-plane vibrational ZA phonons dominate the heat transport in clean suspended graphene and the suppression is attributed to the strong ZA phonon scattering by SiO<sub>2</sub> support. The influence of polymer residue on one side of the suspended bilayer graphene is shown to give a similar effect on the thermal transport. In comparison, the encased graphene showed large suppression of the conductivity, likely caused by the stronger phonon scattering effect at the interface.

Although high  $\kappa$  values in suspended graphene measured with micro-Raman technique reached 3000-5000 Wm<sup>-1</sup>K<sup>-1</sup>, it is not clear that the suspended sample prepared by PMMA transfer method is polymer free. Especially, the  $\kappa$  measurement is largely affected by the accuracy of the Raman-based thermometry method, where strains, impurity doping, and local non-equilibrium between different phonon populations in the laser spot can introduce errors to the measurements.

#### **4.6 SUMMARY**

The basal-plane  $\kappa$  in suspended graphene between 1 and 7 atomic layers is measured with micro-bridge devices, on which graphene samples are transferred by using a PMMA carrier film. The room temperature  $\kappa$  was measured to be  $672 \pm 28$  and  $724 \pm 35$  Wm<sup>-1</sup>K<sup>-1</sup> for bi-layer and 7 layer samples, respectively. TEM analysis on 7 layer sample shows that the suspended sample is a high quality single crystal. In addition, a thin layer

of polymer residue is observed. The room-temperature  $\kappa$  of these suspended graphene samples with polymer residue was found to decrease with increasing layer thickness. This trend emphasizes the impact of polymer-induced phonon scattering in suspended graphene. Although the polymer-induced scattering is more pronounced in thinner samples, it is also the dominant mechanism for the suppressed  $\kappa$  found in the 7-layer graphene sample.

## REFERENCES

1. Cai, W. W.; Moore, A. L.; Zhu, Y. W.; Li, X. S.; Chen, S. S.; Shi, L.; Ruoff, R. S., *Nano Lett* **2010**, *10*, 1645-1651.
2. Balandin, A. A.; Ghosh, S.; Bao, W. Z.; Calizo, I.; Teweldebrhan, D.; Miao, F.; Lau, C. N., *Nano Lett* **2008**, *8*, 902-907.
3. Pettes, M. T.; Jo, I. S.; Yao, Z.; Shi, L., *Nano Lett* **2011**, *11*, 1195-1200.
4. Jang, W. Y.; Chen, Z.; Bao, W. Z.; Lau, C. N.; Dames, C., *Nano Lett* **2010**, *10*, 3909-3913.
5. Sadeghi, M. M.; Pettes, M. T.; Shi, L., *Solid State Commun* **2012**, *152*, 1321-1330.
6. Seol, J. H.; Jo, I.; Moore, A. L.; Lindsay, L.; Aitken, Z. H.; Pettes, M. T.; Li, X. S.; Yao, Z.; Huang, R.; Broido, D.; Mingo, N.; Ruoff, R. S.; Shi, L., *Science* **2010**, *328*, 213-216.
7. Lin, Y. C.; Lu, C. C.; Yeh, C. H.; Jin, C. H.; Suenaga, K.; Chiu, P. W., *Nano Lett* **2012**, *12*, 414-419.
8. Lock, E. H.; Baraket, M.; Laskoski, M.; Mulvaney, S. P.; Lee, W. K.; Sheehan, P. E.; Hines, D. R.; Robinson, J. T.; Tosado, J.; Fuhrer, M. S.; Hernandez, S. C.; Waltont, S. G., *Nano Lett* **2012**, *12*, 102-107.
9. Goossens, A. M.; Calado, V. E.; Barreiro, A.; Watanabe, K.; Taniguchi, T.; Vandersypen, L. M. K., *Appl Phys Lett* **2012**, *100*, 073110.

10. Liang, X. L.; Sperling, B. A.; Calizo, I.; Cheng, G. J.; Hacker, C. A.; Zhang, Q.; Obeng, Y.; Yan, K.; Peng, H. L.; Li, Q. L.; Zhu, X. X.; Yuan, H.; Walker, A. R. H.; Liu, Z. F.; Peng, L. M.; Richter, C. A., *Acs Nano* **2011**, *5*, 9144-9153.
11. Ishigami, M.; Chen, J. H.; Cullen, W. G.; Fuhrer, M. S.; Williams, E. D., *Nano Lett* **2007**, *7*, 1643-1648.
12. Dean, C. R.; Young, A. F.; Meric, I.; Lee, C.; Wang, L.; Sorgenfrei, S.; Watanabe, K.; Taniguchi, T.; Kim, P.; Shepard, K. L.; Hone, J., *Nat Nanotechnol* **2010**, *5*, 722-726.
13. Ryu, S.; Liu, L.; Berciaud, S.; Yu, Y. J.; Liu, H. T.; Kim, P.; Flynn, G. W.; Brus, L. E., *Nano Lett* **2010**, *10*, 4944-4951.
14. Huang, P. Y.; Ruiz-Vargas, C. S.; van der Zande, A. M.; Whitney, W. S.; Levendorf, M. P.; Kevek, J. W.; Garg, S.; Alden, J. S.; Hustedt, C. J.; Zhu, Y.; Park, J.; McEuen, P. L.; Muller, D. A., *Nature* **2011**, *469*, 389.
15. Park, J. S.; Reina, A.; Saito, R.; Kong, J.; Dresselhaus, G.; Dresselhaus, M. S., *Carbon* **2009**, *47*, 1303-1310.
16. Berciaud, S.; Ryu, S.; Brus, L. E.; Heinz, T. F., *Nano Lett* **2009**, *9*, 346-352.
17. Nam, S. G.; Ki, D. K.; Lee, H. J., *Phys Rev B* **2010**, *82*, 245416.
18. Touloukian, Y. S.; Powell, R. W.; Ho, C. Y.; Klemens, P. G., *New York, IFI/Plenum* **1970**.
19. Slack, G. A., *Phys Rev* **1962**, *127*, 694.
20. Gaskell, P. E.; Skulason, H. S.; Rodenchuk, C.; Szkopek, T., *Appl Phys Lett* **2009**, *94*, 143101.

21. Lindsay, L.; Broido, D. A.; Mingo, N., *Phys Rev B* **2010**, 82, 115427.

## Chapter 5. Thermal Conductivity Measurements of Suspended Hexagonal Boron Nitride

### 5.1 INTRODUCTION

Both h-BN and graphite belong to the family of hexagonal layered materials. Although the lattice constants are similar for the two materials, the electronic properties are completely different.<sup>1</sup> While graphite is a semi-metal, breaking of the sub-lattice symmetry in h-BN results in a wide direct band gap of 5.8 eV, which enables its use as a dielectric layer in electronic devices as well as a lasing material in the ultra-violet spectrum.<sup>2</sup> Because of the clean and atomically smooth surface of h-BN, the electron mobility of graphene electronic devices supported on exfoliated few-layer h-BN has been found to be an order of magnitude higher than those supported on silicon dioxide (SiO<sub>2</sub>).<sup>3</sup> In addition, the basal-plane thermal conductivity ( $\kappa$ ) of a pyrolytic h-BN bulk sample has been reported to be as high as 390 Wm<sup>-1</sup>K<sup>-1</sup> at room-temperature.<sup>4</sup> This value is 280 times higher than that for the SiO<sub>2</sub> dielectric used in current-generation silicon electronic devices, and is lower than only few dielectrics such as diamond. Although the  $\kappa$  along the *c*-axis of h-BN is as low as 2 Wm<sup>-1</sup>K<sup>-1</sup> because of the anisotropic layered crystal structure,<sup>5</sup> the high basal-plane  $\kappa$  can be used to enhance lateral heat spreading when few-layer h-BN is used as the dielectric support for graphene electronic devices as well as other future-generation thin-film devices made of silicon, conducting polymers, or other novel layered semiconductors.<sup>6</sup> In contrast, although the basal plane  $\kappa$  of graphite can be even higher than that reported for h-BN bulk crystals, the semi-metallic nature of graphite and few-layer graphene can result in electrical shorting when they are used as a heat

spreader directly beneath the active layer in electronic devices. Despite the attractive thermal and electrical properties of h-BN for thermal management, recent studies of thermal transport in two-dimensional materials have been limited to single and few-layer graphene.<sup>7,8</sup> Although a theoretical study of phonon transport in few-layer h-BN has been reported recently,<sup>9</sup> experimental data on the thermal transport properties in this system are lacking.

In this Chapter, we present thermal transport measurements of suspended few-layer h-BN samples. Because the intensity of the Raman peaks in few-layer h-BN is very weak compared to those in few-layer graphene, micro-Raman thermometry methods developed for thermal measurements of graphene<sup>7, 10, 11</sup> are not applicable for h-BN. Hence, we have established a method to transfer and suspend few-layer h-BN samples onto micro-bridge devices with built-in resistance thermometers for thermal transport measurements. With this method, few-layer h-BN samples of different suspended lengths and layer thicknesses have been measured to obtain the  $\kappa$  and the thermal contact resistance in the temperature range between 45 and 450 K.

## **5.2 SAMPLE PREPARATION AND CHARACTERIZATION**

The same micro-bridge device presented in the previous Chapter is used to measure  $\kappa$  of suspended h-BN. The few-layer h-BN sample was transferred and suspended onto the central rectangular frame made of SiN<sub>x</sub> beams according to the procedure shown in Fig. 5.1 (a-d). In this procedure, few-layer h-BN was first exfoliated

from h-BN powder crystals onto a silicon substrate covered with  $\sim 290$  nm thick thermal oxide, which provides sufficient optical contrast for identifying few-layer h-BN [Fig. 5.1 (a)]. After a PMMA layer was spin coated on the sample and patterned with the use of electron-beam lithography (EBL), the exposed region of the few-layer h-BN flake was etched by  $\text{CF}_4/\text{O}_2$  plasma to form a rectangular h-BN ribbon. Subsequently, EBL and metal lift-off process were used to deposit Au registration marks around the patterned h-BN [Fig. 5.1 (b)]. A  $\sim 1.5$   $\mu\text{m}$  thick PMMA film was then spin-coated onto the substrate. After the sample was placed in a 1% hydrofluoric acid solution, the interface oxide was etched so that the PMMA layer was detached from the substrate. The few-layer h-BN sample and the gold alignment marks were attached to the PMMA film that floated on top of the solution. Upon thorough rinsing with deionized water, the wet PMMA film was manually aligned to the micro-bridge device under an optical microscope [Fig. 5.1 (c,f)]. After the deionized water was evaporated, the device was annealed at  $150^\circ\text{C}$  in vacuum to increase the adhesion between the few-layer h-BN and the micro-bridge device. The PMMA film was subsequently dissolved in acetone heated to about  $60^\circ\text{C}$  and then dried. Figure 5.1 (g) shows a completed device consisting of a suspended 11-layer h-BN sample.

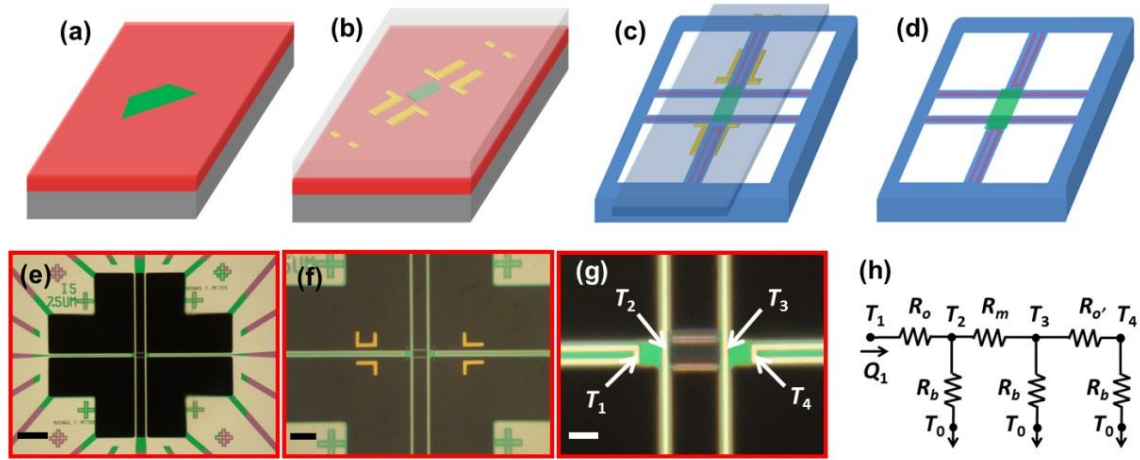


**Figure 5. 1** Transfer of exfoliated few-layer h-BN over a micro-bridge device. The top row consists of schematics showing (a) a few-layer h-BN flake (green) exfoliated on top of a Si substrate (gray) covered by thermal oxide (red), (b) Au registration marks (golden) on the substrate and a PMMA layer (semi-transparent) covering the patterned few-layer h-BN ribbon, (c) the PMMA carrier layer transferred on top of the micro-bridge device (blue), and (d) few-layer h-BN suspended on the central SiN<sub>x</sub> frame of the micro-device after the dissolution of the PMMA layer. The bottom row consists of optical micrographs showing (e) the micro-bridge device, (f) the PMMA layer aligned on the device, and (g) an 11-layer h-BN sample suspended on the device after dissolving of the PMMA layer, and (h) equivalent thermal circuit of the measurement device, where  $T_1$ ,  $T_2$ ,  $T_3$ , and  $T_4$  are the temperature at the middle point of the four Cr/Pt lines, as shown in (g).  $R_m$  is the equivalent thermal resistance of the few-layer h-BN and the two SiN<sub>x</sub> bars underneath,  $R_b$  is the thermal resistance of each of the four Cr/Pt/SiN<sub>x</sub> beams at the two ends of the h-BN sample,  $R_o$  and  $R_o'$  are the thermal resistance of the two SiN<sub>x</sub> connections between the middle points of the U-shaped Cr/Pt line and the adjacent straight Cr/Pt line. The scale bars represent 25, 10, 5  $\mu\text{m}$  in (e-g), respectively.

A through-substrate hole under the micro-bridge allowed for transmission electron microscopy (TEM) characterization of the crystal structure of the few-layer h-BN sample suspended on the device upon the completion of the thermal measurement. Table 1 lists the layer thickness and lateral dimensions obtained from TEM and scanning

electron microscopy (SEM) analyses of each of the four h-BN samples measured in this work. The thickness of sample h-BN1 was determined from atomic force microscopy (AFM). For the other three samples, the layer thickness was obtained from the (0002) lattice fringes at the folded edge of each suspended h-BN sample. For example, the lattice fringes shown in Fig. 5.2 (a) and (c) reveal that samples h-BN3 and h-BN4 consisted of 11 and 5 atomic layers, respectively. The selected area electron diffraction (SAED) patterns from the center of these samples produce only one set of Bragg reflections [Fig. 5.2 (b,d)], indicative of a single crystal structure within the 4.25  $\mu\text{m}$  diameter focused electron beam spot and AAA stacking order, which has also been observed in previous reports.<sup>1, 12</sup> Additionally, we consistently observed the presence of polymer residues on the surface of all four h-BN samples during TEM analysis. Similar polymer residue has been observed on the surface of suspended graphene or h-BN samples that were in contact with a PMMA layer during sample preparation.<sup>13, 14</sup> Although thermal annealing under various gas environments has been employed to burn out the PMMA residue, it has been found that polymer residue cannot be completely removed from the sample surface.<sup>14-18</sup> In this work, annealing of the h-BN sample in air for 3 hours at 300°C was found to be ineffective in removing the PMMA residue.

**Table 1** Dimension of the suspended h-BN samples measured in this work.

	Number of Layers	Width ( $\mu\text{m}$ )	Suspended Length ( $\mu\text{m}$ )
<b>h-BN1</b>	<b><math>12 \pm 1</math></b>	<b>9.0</b>	<b>3.0</b>
<b>h-BN2</b>	<b>12</b>	<b>6.7</b>	<b>5.0</b>
<b>h-BN3</b>	<b>11</b>	<b>6.5</b>	<b>7.5</b>
<b>h-BN4</b>	<b>5</b>	<b>6.6</b>	<b>7.5</b>

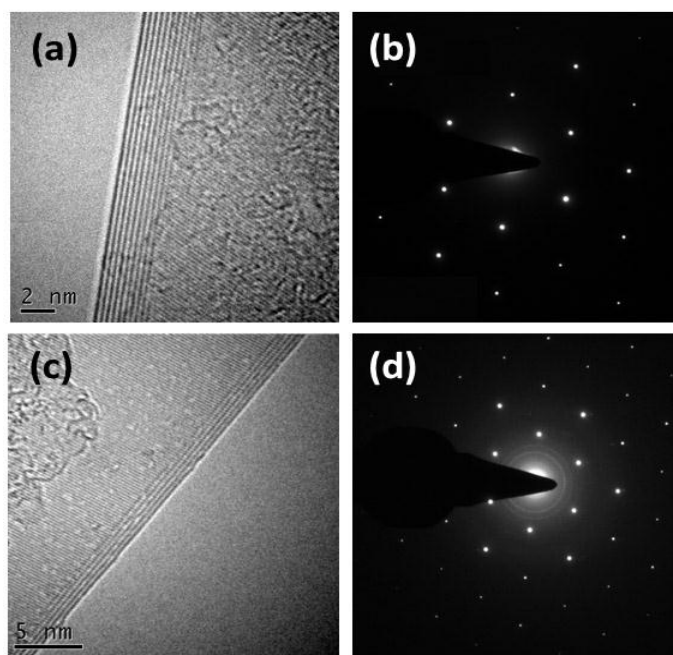


**Figure 5. 2** TEM images and electron diffraction patterns of few-layer h-BN samples. (a) TEM micrograph of the folded edge of sample h-BN3 showing that the sample consisted of 11 atomic layers. (b) SAED pattern taken from an 825 nm diameter region of sample h-BN3. (c) TEM micrograph of sample h-BN4 showing 5 atomic layers. (d) SAED pattern taken from a 4.25  $\mu\text{m}$  diameter region of h-BN4.

### 5.3 RESULTS

The devices were placed in the evacuated sample space of a cryostat for thermal measurements. During the measurement, the electrical resistance of each of the four metal lines was measured to determine the average temperature rise ( $\overline{\Delta T_j}$ ,  $j = 1, 2, 3,$  and  $4$ ) in the metal line when one U-shaped Cr/Pt line was electrically heated. For the other U-shaped metal line and the two straight metal lines, the temperature rise at the mid-point of the metal line is twice of the average temperature rise, i.e.  $\Delta T_j \equiv T_j - T_0 = 2\overline{\Delta T_j}$ ;  $j = 2, 3, 4$ , where  $T_0$  is the substrate temperature. In addition, heat conduction analysis of the U-shaped heater line yields the temperature rise at its mid-point as  $\Delta T_1 = \frac{3}{2}\overline{\Delta T_1} - \frac{1}{2}(\overline{\Delta T_2} + \overline{\Delta T_3} + \overline{\Delta T_4})$ .<sup>19, 20</sup> The thermal resistance values of the four Cr/Pt/SiN<sub>x</sub> beams ( $R_b$ ) are designed to be identical, and can be found from the heat conduction analysis of the heater line in conjunction with the thermal resistance circuit in Fig. 5.1 (h) as  $R_b = 2(\Delta T_1 + \Delta T_2 + \Delta T_3 + \Delta T_4)/Q$ , where  $Q$  is the rate of electrical heating in the U-shaped heater line. A similar analysis yields the equivalent thermal resistance of the suspended h-BN and the two underlying SiN<sub>x</sub> bars as  $R_m = R_b(\Delta T_2 - \Delta T_3)/(\Delta T_3 + \Delta T_4)$ . The accuracy of this analytical solution has been verified by a three-dimensional finite element simulation.<sup>20</sup> The corresponding thermal conductance of the suspended h-BN and the two SiN<sub>x</sub> bars is then obtained as  $G_m = 1/R_m$ . The thermal conductance of the two SiN<sub>x</sub> bars ( $G_n$ ) was measured using the same procedure when there was no h-BN on the device. The thermal conductance and thermal

resistance of the suspended h-BN alone were then obtained as  $G_s = G_m - G_n$  and  $R_s = 1/G_s$ , respectively. As shown in Fig. 5.3 (a), the thermal conductance contribution of the two SiN<sub>x</sub> bars increased at low temperatures and was found to be in the range of 3-7% and 25-41% of the measured  $G_s$  values for h-BN1 and h-BN4, respectively.

The obtained thermal resistance of the h-BN sample contains the diffusive thermal resistance ( $R_d$ ) and the contact thermal resistance ( $R_c$ ), i.e.,  $R_s = R_d + R_c$  and  $R_d = L/(\kappa t W)$ , where  $L$ ,  $t$ , and  $W$  are the length, thickness, and width of the suspended h-BN, as illustrated in Fig. 5.3 (b). The  $R_d$  value decreases with increasing  $t$  and decreasing  $L$  so that  $R_c$  can be appreciable for thick h-BN samples with a short suspended length. In this work,  $L$  varies from 3 to 7.5  $\mu\text{m}$  for the three 11-12 layer thick samples. Based on the assumption of the same contact resistance per unit contact width for all samples that have a similar contact length ( $L_c$ ) as well as the assumption of the same  $\kappa$  for the three samples with a similar layer thickness, we use the relation,  $R_s W = L/(\kappa t) + R_c W$ , to fit the  $R_s W$  versus  $L/t$  data of the three 11-12 layer samples, as shown in Fig. 5.3 (c). The as-obtained  $R_c W$  product, which corresponds to the intercept of the linear fitting at  $L = 0$ , is used to determine the  $R_c$  value for the two 7.5  $\mu\text{m}$  long samples with a thickness of 11 and 5 layers, respectively. The obtained  $R_c$  value increases from 20% to 33% of the measured  $R_s$  for the 11-layer sample when the temperature decreases from 300 K to 45 K. In comparison, the obtained  $R_c$  is only 8% and 11% of the measured  $R_s$  for the 5-layer sample at temperature 300 K and 45 K. In both cases, the obtained  $R_c$  is subtracted from the measured  $R_s$  to obtain the  $R_d$  and  $\kappa$  values of the two samples.

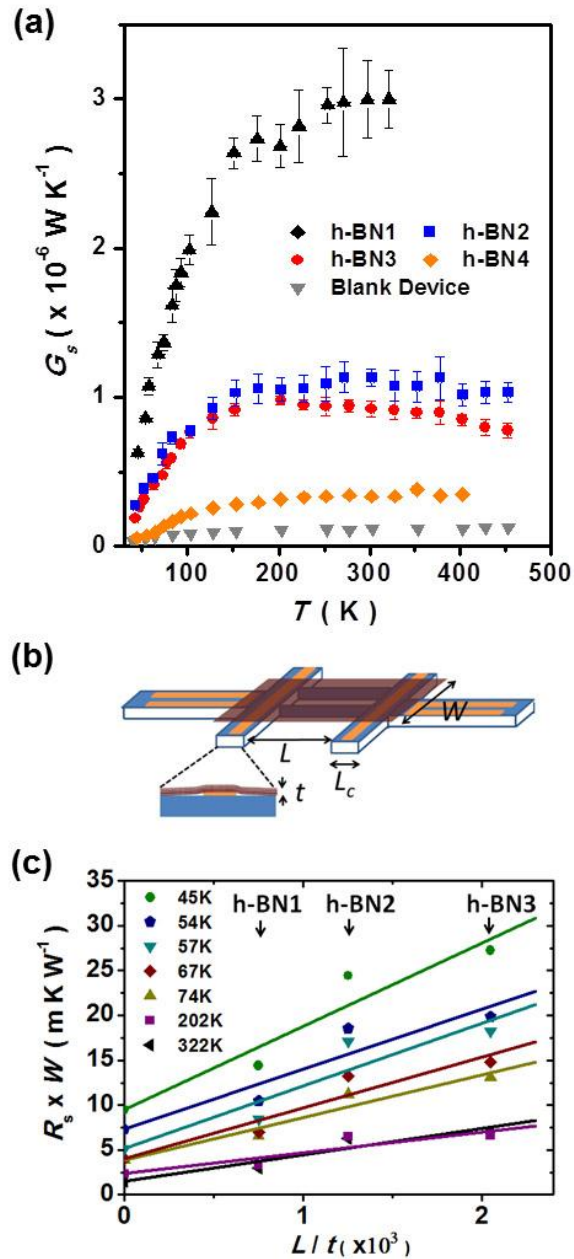


**Figure 5.3** (a) Measured thermal conductance values of four h-BN samples ( $G_s$ ) and of the two  $7.5 \mu\text{m}$  long  $\text{SiN}_x$  bars ( $G_n$ ) of one blank device. (b) Schematic showing the relevant dimensions of a h-BN sample suspended on the central frame of the micro-bridge device. (c) The  $R_s W$  product versus the  $L/t$  ratio for the three 11-12 layer thick samples at different temperatures indicated in the legend. The lines are linear fitting to the measurement values shown as symbols.

From the  $R_c$  value, the thermal interface conductance per unit area ( $g_i$ ) can be calculated, which increases from  $1.7 \times 10^5 \text{ Wm}^{-2}\text{K}^{-1}$  at 45 K to  $1.7 \times 10^6 \text{ Wm}^{-2}\text{K}^{-1}$  to 300 (See Appendix D). In general,  $g_i$  is expected to increase with increasing temperature because it is proportional to the specific heat that increases with temperature. However, the  $g_i$  values from our measurements are 1-2 orders of magnitude lower than those reported for graphene-SiO<sub>2</sub><sup>21</sup> and graphene-metal interfaces,<sup>21, 22</sup> likely because of roughness on the micro-bridge device and contamination left at the interface between the as-transferred few-layer h-BN and the device.

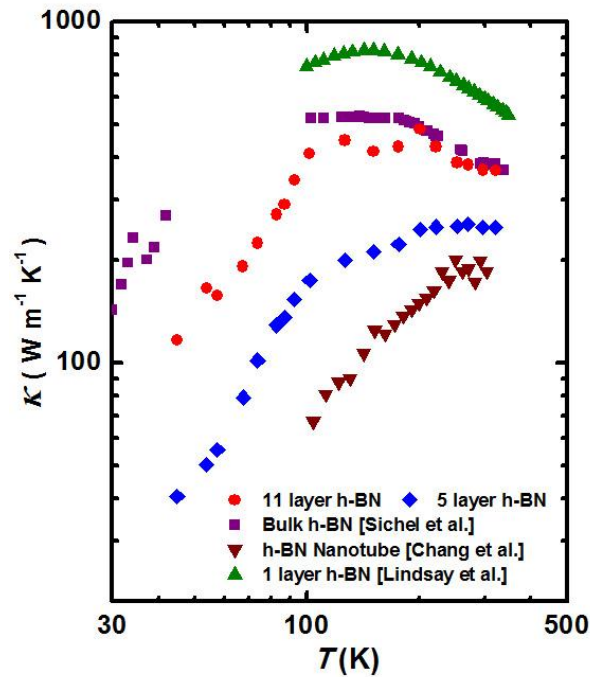


**Figure 5. 4**  $\kappa$  values of the two 7.5  $\mu\text{m}$  long, 11 and 5 layer thick suspended h-BN samples as a function of temperature. Shown in comparison are the measured basal plane  $\kappa$  reported by Sichel et al. for bulk h-BN<sup>4</sup> and by Chang et al. for a multi-walled h-BN nanotube,<sup>23</sup> and the calculation result reported by Lindsay et al. for a single-layer suspended h-BN.<sup>9</sup>

As shown in Fig. 5.4, the obtained room-temperature  $\kappa$  of the 11-layer sample is about  $360 \text{ Wm}^{-1}\text{K}^{-1}$ , which approaches the basal-plane value reported for bulk h-BN.<sup>4</sup> As the temperature decreases, the  $\kappa$  of this sample initially increases due to reduced Umklapp scattering, reaching its peak value between 100 K and 200 K, similar to bulk samples. At lower temperatures, the  $\kappa$  of the 11-layer sample becomes lower than the bulk values. A recent theoretical calculation has suggested that the  $\kappa$  of atomically-clean suspended few-layer h-BN increases as the number of layers decreases because of the reduction of interlayer phonon scattering.<sup>9</sup> Our results do not follow this trend as the  $\kappa$  of the 5-layer sample is lower than that of the 11-layer sample. In addition, the  $\kappa$  suppression in the thinner sample becomes more pronounced at lower temperatures with the peak value appearing at near room temperature. Interestingly, both samples measured here maintain higher  $\kappa$  than that reported for a multi-walled h-BN nanotube, which was measured with a different micro-bridge device without eliminating the contact thermal resistance.<sup>23</sup>

To understand the  $\kappa$  suppression at low temperatures, we first evaluate the impact of phonon scattering by the lateral edges of the h-BN ribbon and by point defects. We have calculated the  $\kappa$  of the suspended h-BN using the Eq. (4.13)

$$\kappa = \frac{1}{4\delta} \sum_p \int_{\omega=0}^{\omega_{\max}} v_p^2 \tau_p D_p(\omega) \hbar \omega \frac{d \langle n \rangle}{dT} d\omega$$

where  $\delta$  is the interlayer spacing,  $p$  is the phonon polarization,  $v_p$  is group velocity,  $\tau_p$  is the relaxation time,  $D_p(\omega)$  is the density of states per unit area, and  $\langle n \rangle$  is the Bose-

Einstein distribution. The phonon dispersion of bulk h-BN was obtained from an *ab initio* calculation based on local density approximation with the use of Quantum ESPRESSO.<sup>24</sup> The phonon scattering rate by the lateral edge of the few-layer h-BN samples was calculated as  $\tau_{B,p}^{-1} = v_p/l_b$ , where  $l_b$  is the edge scattering mean free path. The boron atoms in our samples consist of 19.9% <sup>10</sup>B and 80.1% <sup>11</sup>B. Phonon scattering by the isotopic impurities was considered in the calculation. Due to the high concentration of isotope impurities, other atomic impurities or structural defects such as point vacancies have been found to play a less important role even when the point vacancy concentration is as high as  $10^{20}$  cm<sup>-3</sup>. Without accounting for scattering by polymer residues and Umklapp scattering, the latter of which is negligible at low temperatures, the calculated  $\kappa$  shows good agreement with the measurement results at temperatures below 100 K when  $l_b$  is taken to be 550 nm and 180 nm for the 11 and 5 layer h-BN samples, respectively (See Appendix C). However, the values are much smaller than the 3–7.5  $\mu$ m length of the single-crystalline h-BN samples and the 3.5  $\mu$ m separation between the two SiN<sub>x</sub> bars below the h-BN. Hence, edge scattering and point defect scattering are not responsible for the considerably suppressed  $\kappa$  at low temperatures.

Several theoretical calculations have suggested that the presence of surface functional groups can result in large suppression of the  $\kappa$  of suspended graphene.<sup>25, 26</sup> Similarly, the presence of the polymer residue on the sample surfaces can lead to even stronger suppression. Such scenario has been suggested in our recent measurement of suspended bi-layer graphene.<sup>18</sup> Because the polymer residue was clearly observed from

the TEM images on the surfaces of the h-BN samples as a result of fabrication process, we attribute the trend of decreasing  $\kappa$  with decreasing layer thickness to phonon scattering by the polymer residue. Such scattering is expected to play an increasing role as the layer thickness decreases. In particular, because low-frequency phonons dominate the low-temperature  $\kappa$ , the larger suppression found in the thinner sample at lower temperatures suggests a higher scattering rate of low-frequency phonons by the polymer residue. At high temperatures, on the other hand, polymer-induced scattering becomes less important compared to Umklapp scattering, thus the suppression from bulk  $\kappa$  becomes smaller, especially in the thicker samples.

#### **5.4 SUMMARY**

Our measurement results show that the room-temperature  $\kappa$  of suspended h-BN can approach the basal-plane values of bulk h-BN crystals at room temperature when the thickness increases to more than 10 atomic layers in spite of the presence of polymer residue on the sample surface. As the sample thickness decreases, the  $\kappa$  decreases because of increasing phonon scattering by polymer residues, which is more pronounced at low temperatures or for low-frequency phonons. These new findings, especially the thickness needed to obtain the bulk  $\kappa$  values in these few-layer h-BN samples with polymer residues, provide new insight into the effect of polymer residues and surface functional groups on phonons and especially low-frequency phonons in two-dimensional layer materials. The result is of value for the exploration of few-layer h-BN as a heat

spreading layer in novel electronic devices made of flexible polymeric substrate, or as fillers to enhance the  $\kappa$  of polymeric composites.

## REFERENCES

1. Alem, N.; Erni, R.; Kisielowski, C.; Rossell, M. D.; Gannett, W.; Zettl, A., *Phys Rev B* **2009**, *80*, 155425.
2. Watanabe, K.; Taniguchi, T.; Kanda, H., *Nat Mater* **2004**, *3*, 404-409.
3. Dean, C. R.; Young, A. F.; Meric, I.; Lee, C.; Wang, L.; Sorgenfrei, S.; Watanabe, K.; Taniguchi, T.; Kim, P.; Shepard, K. L.; Hone, J., *Nat Nanotechnol* **2010**, *5*, 722-726.
4. Sichel, E. K.; Miller, R. E.; Abrahams, M. S.; Buiocchi, C. J., *Phys Rev B* **1976**, *13*, 4607-4611.
5. Simpson, A.; Stuckes, A. D., *J Phys Part C Solid* **1971**, *4*, 1710.
6. Mak, K. F.; He, K. L.; Shan, J.; Heinz, T. F., *Nat Nanotechnol* **2012**, *7*, 494-498.
7. Balandin, A. A., *Nat Mater* **2011**, *10*, 569-581.
8. Sadeghi, M. M.; Pettes, M. T.; Shi, L., *Solid State Commun* **2012**, *152*, 1321-1330.
9. Lindsay, L.; Broido, D. A., *Phys Rev B* **2011**, *84*, 155421.
10. Cai, W. W.; Moore, A. L.; Zhu, Y. W.; Li, X. S.; Chen, S. S.; Shi, L.; Ruoff, R. S., *Nano Lett* **2010**, *10*, 1645-1651.
11. Faugeras, C.; Faugeras, B.; Orlita, M.; Potemski, M.; Nair, R. R.; Geim, A. K., *Acs Nano* **2010**, *4*, 1889-1892.
12. Han, W. Q.; Wu, L. J.; Zhu, Y. M.; Watanabe, K.; Taniguchi, T., *Appl Phys Lett* **2008**, *93*, 223103.

13. Huang, P. Y.; Ruiz-Vargas, C. S.; van der Zande, A. M.; Whitney, W. S.; Levendorf, M. P.; Kevek, J. W.; Garg, S.; Alden, J. S.; Hustedt, C. J.; Zhu, Y.; Park, J.; McEuen, P. L.; Muller, D. A., *Nature* **2011**, *469*, 389.
14. Lin, Y. C.; Lu, C. C.; Yeh, C. H.; Jin, C. H.; Suenaga, K.; Chiu, P. W., *Nano Lett* **2012**, *12*, 414-419.
15. Lock, E. H.; Baraket, M.; Laskoski, M.; Mulvaney, S. P.; Lee, W. K.; Sheehan, P. E.; Hines, D. R.; Robinson, J. T.; Tosado, J.; Fuhrer, M. S.; Hernandez, S. C.; Waltont, S. G., *Nano Lett* **2012**, *12*, 102-107.
16. Goossens, A. M.; Calado, V. E.; Barreiro, A.; Watanabe, K.; Taniguchi, T.; Vandersypen, L. M. K., *Appl Phys Lett* **2012**, *100*, 073110.
17. Liang, X. L.; Sperling, B. A.; Calizo, I.; Cheng, G. J.; Hacker, C. A.; Zhang, Q.; Obeng, Y.; Yan, K.; Peng, H. L.; Li, Q. L.; Zhu, X. X.; Yuan, H.; Walker, A. R. H.; Liu, Z. F.; Peng, L. M.; Richter, C. A., *Acs Nano* **2011**, *5*, 9144-9153.
18. Pettes, M. T.; Jo, I. S.; Yao, Z.; Shi, L., *Nano Lett* **2011**, *11*, 1195-1200.
19. Seol, J. H.; Jo, I.; Moore, A. L.; Lindsay, L.; Aitken, Z. H.; Pettes, M. T.; Li, X. S.; Yao, Z.; Huang, R.; Broido, D.; Mingo, N.; Ruoff, R. S.; Shi, L., *Science* **2010**, *328*, 213-216.
20. Seol, J. H.; Moore, A. L.; Shi, L.; Jo, I.; Yao, Z., *J Heat Trans-T Asme* **2011**, *133*, 022403.
21. Mak, K. F.; Lui, C. H.; Heinz, T. F., *Appl Phys Lett* **2010**, *97*, 221904.
22. Koh, Y. K.; Bae, M. H.; Cahill, D. G.; Pop, E., *Nano Lett* **2010**, *10*, 4363-4368.

23. Chang, C. W.; Fennimore, A. M.; Afanasiev, A.; Okawa, D.; Ikuno, T.; Garcia, H.; Li, D. Y.; Majumdar, A.; Zettl, A., *Phys Rev Lett* **2006**, *97*, 085901.
24. Giannozzi, P.; Baroni, S.; Bonini, N.; Calandra, M.; Car, R.; Cavazzoni, C.; Ceresoli, D.; Chiarotti, G. L.; Cococcioni, M.; Dabo, I.; Dal Corso, A.; de Gironcoli, S.; Fabris, S.; Fratesi, G.; Gebauer, R.; Gerstmann, U.; Gougoussis, C.; Kokalj, A.; Lazzeri, M.; Martin-Samos, L.; Marzari, N.; Mauri, F.; Mazzarello, R.; Paolini, S.; Pasquarello, A.; Paulatto, L.; Sbraccia, C.; Scandolo, S.; Sclauzero, G.; Seitsonen, A. P.; Smogunov, A.; Umari, P.; Wentzcovitch, R. M., *J Phys-Condens Mat* **2009**, *21*, 395502.
25. Chien, S. K.; Yang, Y. T.; Chen, C. K., *Appl Phys Lett* **2011**, *98*, 033107.
26. Kim, J. Y.; Lee, J.-H.; Grossman, J. C., *Acs Nano* **2012**, *6*, 9050-9057.

## Chapter 6. Summary and Outlook

### 6.1 SUMMARY

In this thesis, we have presented experimental studies focused on the thermal transport properties of two dimensional materials, graphene and h-BN.

We first employed the scanning thermal microscopy (SThM) technique on graphene devices fabricated on oxidized silicon substrates. With sub-micrometer spatial resolution, the SThM revealed shifting of local hot spots in electrically biased graphene. The locations of the hot spots correspond to low-carrier concentration regions controlled by both the bias and gate voltages. After employing both contact and lift modes for temperature calibration, the low-frequency acoustic phonon temperature in the graphene channel was found to be in equilibrium with the anharmonic scattering temperature determined from the Raman 2D peak shift. The average temperature rise in the graphene channel scaled linearly with the applied electrical power divided by the thermal resistance of the underlying Si and SiO<sub>2</sub>, indicating vertical heat dissipation through the substrates.

In Chapter 4, the thermal conductivity  $\kappa$  of suspended graphene between 1 and 7 atomic layers thick was measured with micro-bridge devices, on which graphene samples were transferred using a PMMA carrier film. The room temperature  $\kappa$  was measured to be 670 and 725 Wm<sup>-1</sup>K<sup>-1</sup> for bi-layer and 7 layer samples, respectively. Transmission electron microscopy analysis on a 7 layer sample showed that the suspended sample was a high quality single crystal and it contained a thin layer of polymer residue on the surface even after annealing in air. Based on the measurements on 8 suspended graphene

samples with different thicknesses, the room-temperature  $\kappa$  values were found to increase with increasing layer thickness. This trend also suggested that the polymer residue was responsible for the phonon scattering at the surface of the suspended graphene samples.

In Chapter 5, we used the same micro-bridge device to measure the  $\kappa$  of suspended few-layer h-BN. Based on the measurements on three 11-12 atomic layer h-BN samples with suspended lengths ranging between 3 and 7.5  $\mu\text{m}$ , the contribution of the thermal contact resistance was extracted. The obtained room-temperature  $\kappa$  of an 11-layer h-BN was found to be about  $360 \text{ Wm}^{-1}\text{K}^{-1}$ , approaching the basal plane value reported for bulk h-BN. The presence of polymer residue on the sample surface of a 5-layer h-BN sample resulted in a room temperature  $\kappa$  of about  $250 \text{ Wm}^{-1}\text{K}^{-1}$ . Measured  $\kappa$  values for both 5 and 11 layer samples were suppressed at low temperatures, suggesting increased scattering of low frequency phonons in thin h-BN samples by polymer residue.

## 6.2 OUTLOOK

We have demonstrated in Chapter 3 that the hybrid lift-contact mode SThM can provide the quantitative temperature profiles, although scanning under vacuum is ideal in order to eliminate parasitic heat transfer mechanism due to the air. Very recently, Kim et al.<sup>1</sup> have implemented SThM operating in an ultrahigh vacuum chamber. In that experiment, contact mode scan alone without the need of lift mode was able to provide the quantitative temperature profiles, which also accelerated the measurements.

One of the results of SThM measurements on graphene devices is that the average temperature rise in the graphene device is proportional to the electrical power divided by

the thermal resistance of the underlying substrate. Depending on the choice of underlying substrate, the temperature rise in the graphene device will be determined by the  $\kappa$  value of dielectric material and bulk substrate. For example,  $\kappa$  of h-BN along the out-of-plane direction,  $2 \text{ Wm}^{-1}\text{K}^{-1}$ , is much lower than the basal plane value,  $360 \text{ Wm}^{-1}\text{K}^{-1}$ . Considering  $\kappa_{\text{SiO}_2} = 1.3 \text{ Wm}^{-1}\text{K}^{-1}$ , the temperature rise in a graphene device fabricated on h-BN can be compared with that in a device fabricated on a SiO<sub>2</sub> dielectric with the same thickness. Because thermal resistance is proportional to the thickness of the dielectric, temperature rises of the device on different thicknesses of dielectric can be determined by SThM as well as Raman-based thermometry.

We have observed that the average temperatures in the graphene channel measured by different thermometry methods were roughly the same except the observation by Chae et al.<sup>2</sup> In their experiment, the G-phonon temperature was much higher than the equilibrium temperature in a sample with a constriction width of  $0.6 \mu\text{m}$ . Other measurements using relatively large graphene channel suggested that the optical phonons were in equilibrium with electrons and lattices at sufficiently high temperatures. Thus, it would be interesting to study the non-equilibrium states between electrons, optical phonons, and acoustic phonons in samples with a constriction. In order to reach this non-equilibrium state, high temperature rise is required. The current SThM measurement in air restricts the measurement to below 500 K because air convection sometimes disengages the tip during the scan. However, measurement under vacuum can resolve this issue.

One way to investigate the non-equilibrium state of hot carriers is to use suspended graphene. It has been shown in supported graphene that surface polar phonons in SiO<sub>2</sub> limit the speed of high energy electrons.<sup>3,4</sup> Thus, absence of underlying substrate helps the suspended graphene reach high temperatures, where non-equilibrium state can be studied with different thermometry methods. Interestingly, we observed that mechanical strength of graphene and h-BN allowed for tapping mode AFM scanning on suspended samples. Hence it is very likely that contact mode SThM can work for suspended graphene and h-BN samples. Additionally, if the temperature distribution in the sample suspended over the micro-bridge device is resolved, both  $\kappa$  and the thermal contact resistance values can be directly obtained as discuss in Chapter 5.

In our experiments carried out in Chapters 4 and 5, the  $\kappa$  measurements showed the suppression due to the polymer residue from the transfer process. So far, there have been no successful low-temperature measurements of intrinsic  $\kappa$  of single layer graphene or h-BN. It is particularly important to obtain low temperature  $\kappa$  in clean samples because the intrinsic properties of the phonons are reflected in the temperature dependence.

There have been several experiments that suggest alternative methods to obtain clean suspended graphene. Bolotin et al.<sup>5</sup> demonstrated that current annealing in suspended graphene could remove the polymer residues, resulting in high electron mobility up to  $200,000 \text{ cm}^2\text{V}^{-1}\text{s}^{-1}$ . Remarkably, as-fabricated suspended graphene membranes before annealing were found to be more than 10 times greater than that of pristine graphene.<sup>6</sup> As the impact of polymer residue on electron mobility was shown in

their work, a similar effect on  $\kappa$  can be confirmed by comparing the  $\kappa$  measured before and after annealing.

Another approach is to use materials other than PMMA when transferring the sample. For example, as demonstrated by other groups,<sup>7, 8</sup> polycarbonate could be removed easily after transfer, although the mechanical rigidity of polycarbonate makes it difficult to apply for our transfer process.

The suppression of  $\kappa$  by polymer or surrounding medium suggests that  $\kappa$  reduction may be useful for thermoelectric applications by intentionally introducing alien materials on the surface of graphene. Moreover, guided thermal path can be engineered by controlling the  $\kappa$  in a planar geometry. For instance,  $\kappa$  of single layer graphene encased by SiO<sub>2</sub> shows more than 10-fold reduction, which can be used to limit the heat flow in a certain direction.

Lastly, the isotope effect on  $\kappa$  of graphene and h-BN is an interesting research topic. In nature, carbon is composed of 98.9% <sup>12</sup>C and 1.1% <sup>13</sup>C, and elemental boron is a mixture of 80.1% <sup>10</sup>B and 19.9% <sup>11</sup>B. With an isotope enriched single crystal diamond (99.999% <sup>12</sup>C), Wei et al.<sup>9</sup> measured the record high  $\kappa \sim 200,000 \text{ Wm}^{-1}\text{K}^{-1}$  at 80 K. Recently, by using the Raman technique, Chen et al.<sup>10</sup> measured the enhancement of  $\kappa$  at 320 K by a factor of 2 in a graphene sample grown using chemical vapor deposition using 99.99% <sup>12</sup>C, compared to graphene with a 50% <sup>12</sup>C composition. With h-BN, similar measurements have not been carried out yet. In both cases, the isotope effect will be more

pronounced at low temperatures. Hence, measurements using a resistance thermometer device can reveal more significant modification of  $\kappa$  due to the isotope concentration.

## REFERENCES

1. Kim, K.; Jeong, W. H.; Lee, W. C.; Reddy, P., *Acs Nano* **2012**, *6*, 4248-4257.
2. Chae, D. H.; Krauss, B.; von Klitzing, K.; Smet, J. H., *Nano Lett* **2010**, *10*, 466-471.
3. Freitag, M.; Steiner, M.; Martin, Y.; Perebeinos, V.; Chen, Z. H.; Tsang, J. C.; Avouris, P., *Nano Lett* **2009**, *9*, 1883-1888.
4. Meric, I.; Han, M. Y.; Young, A. F.; Ozyilmaz, B.; Kim, P.; Shepard, K. L., *Nat Nanotechnol* **2008**, *3*, 654-659.
5. Bolotin, K. I.; Sikes, K. J.; Jiang, Z.; Klima, M.; Fudenberg, G.; Hone, J.; Kim, P.; Stormer, H. L., *Solid State Commun* **2008**, *146*, 351-355.
6. Chen, C. Y.; Rosenblatt, S.; Bolotin, K. I.; Kalb, W.; Kim, P.; Kymissis, I.; Stormer, H. L.; Heinz, T. F.; Hone, J., *Nat Nanotechnol* **2009**, *4*, 861-867.
7. Lin, Y. C.; Jin, C. H.; Lee, J. C.; Jen, S. F.; Suenaga, K.; Chiu, P. W., *Acs Nano* **2011**, *5*, 2362-2368.
8. Park, H. J.; Meyer, J.; Roth, S.; Skakalova, V., *Carbon* **2010**, *48*, 1088-1094.
9. Wei, L. H.; Kuo, P. K.; Thomas, R. L.; Anthony, T. R.; Banholzer, W. F., *Phys Rev Lett* **1993**, *70*, 3764-3767.
10. Chen, S. S.; Wu, Q. Z.; Mishra, C.; Kang, J. Y.; Zhang, H. J.; Cho, K. J.; Cai, W. W.; Balandin, A. A.; Ruoff, R. S., *Nat Mater* **2012**, *11*, 203-207.

## **Appendices**

## **Appendix A. Temperature Calibration and Finite Element Method**

Temperature detection based on the thermovoltage signals is complicated as discussed in Sec. 3.2 due to the parasitic heat transfer by air and the radiation between the cantilever, the sample, and the substrate. The linear response of the thermovoltage signals during the contact and the lift modes were used to calibrate the temperatures. Because the temperature calibration was performed with the metallic thermometer made of gold, the temperature coefficients between the tip and the graphene may be different from that between the tip and the gold. To address this issue, we performed the finite element method analysis as described in A.2.

### **A.1 CONTACT MODE AND LIFT MODE STHM**

Figure A.1 (a) shows thermovoltage signals while the sample is approached and retracted from the tip. Due to the attractive Van der Waals force, the tip was still in contact with the sample after the sample was retracted by 320 nm from the sample position, whereas the tip jumped into contact with the sample during the approaching cycle. Hence, we used a lift height of 400 nm in the measurement to ensure that the tip was out of contact with the sample during the lift mode measurement.

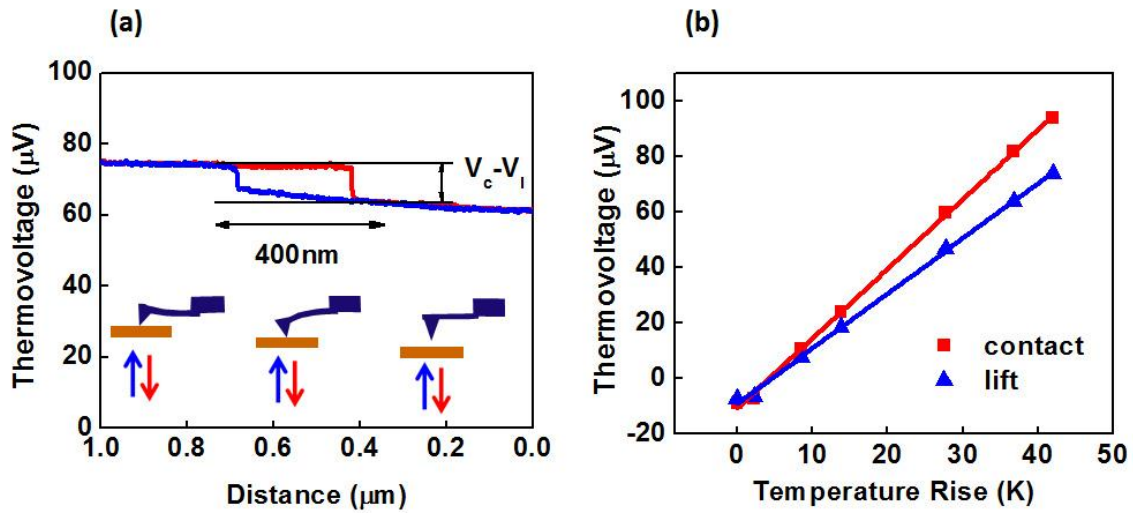


**Figure A.1** (a) Thermovoltage response of SThM probe as the sample is approached and retracted from the tip. (b) Thermovoltage signals of the SThM probe obtained at the center of the heater/thermometer line in the contact mode and lift mode with a 400 nm lift height as a function of the measured temperature rise of the heater/thermometer line.

A sudden jump or drop in the measured thermovoltage signal when the tip was out of contact was much larger than the gradual change when the tip-sample distance was increased by about 100 nm after the tip was already out of the contact. Hence, the difference in the thermovoltages measured in the contact mode and at 400 nm lift height was mainly attributed to heat transfer through the solid-solid contact and a small liquid meniscus surrounding the contact.<sup>4-6</sup> Because the  $\sim 8 \mu\text{m}$  cantilever-sample separation is much larger than the  $\sim 400 \text{ nm}$  lift height, heat transfer through the air gap remains approximately constant during the contact mode and the lift mode measurement. Therefore, the influence of non-local heat transfer through the cantilever-sample air gap

can be mostly eliminated by subtracting the thermovoltage measured in the lift mode from that in the contact mode as detailed below.

Our temperature calibration procedure is somewhat different from but still equivalent to that reported in Ref 1. Because of the presence of a finite thermal contact conductance ( $G_{ts}$ ) and heat flow ( $Q_{ts}$ ) between the tip and the sample, the sample surface temperature rise ( $\theta_s$ ) is higher than the thermocouple tip temperature rise, which is expressed in Ref 1 as

$$\theta_s = \theta_c + \varphi(\theta_c - \theta_l) \quad (\text{A.1})$$

$$Q_{ts} = G_{ts}(\theta_c - \theta_l) \quad (\text{A.2})$$

where  $\theta_c$  and  $\theta_l$  are the thermocouple tip temperature rise during the contact and lift mode measurements, respectively, and  $\varphi$  is a constant.

Because the contact-mode thermovoltage is approximately linearly proportional to the temperature rise of the sample, i.e.,  $\theta_c = \alpha\theta_s$  with  $\alpha < 1$ , equation (A.1) can be written as

$$\theta_s = \frac{\varphi}{1-\alpha}(\theta_c - \theta_l) = \beta(V_c - V_l) \quad (\text{A.3})$$

where  $\beta$  is a constant that depends on  $\varphi$ ,  $\alpha$  and the thermopower of the thermocouple, and  $V_c$  and  $V_l$  are the thermovoltages of the thermocouple measured during the contact mode and the lift mode, respectively. Therefore, the sample temperature rise is expected to be proportional to the difference of the tip temperature rises or the thermovoltage

signals measured during the contact mode and the lift mode. This relationship was confirmed in our measurement, and shown in Fig. A.1 (b).

The proportionality constant  $\beta$  can be obtained with a calibration with a sample of known temperature, without the need of knowing  $\varphi$ ,  $\alpha$  and the thermopower of the thermocouple. We used the 100  $\mu\text{m}$  long metal line heater and thermometer patterned on the graphene, as shown in Fig. 3.2 (a). During the calibration, the metal line was electrically heated and its temperature was converted from the resistance increase by using the measured temperature coefficient of resistance of the metal line as shown in Fig. A.2 (b). Figures A.2 (a) and (b) show the thermovoltage profiles obtained in the contact mode and the lift mode when the SThM probe was scanned across the center of the heater line in the perpendicular direction. At the same heating current in the heater line, the thermovoltage profile obtained in the contact mode is higher than that in the lift mode, with the difference shown in Fig. A.2 (c). At zero heating current, the small negative ( $V_c - V_l$ ) value is caused by the change in the heat transfer from the tip heated by the AFM laser to the sample. This baseline value was subtracted from the ( $V_c - V_l$ ) value measured at different heating currents at the same location to eliminate the error caused by the laser heating.

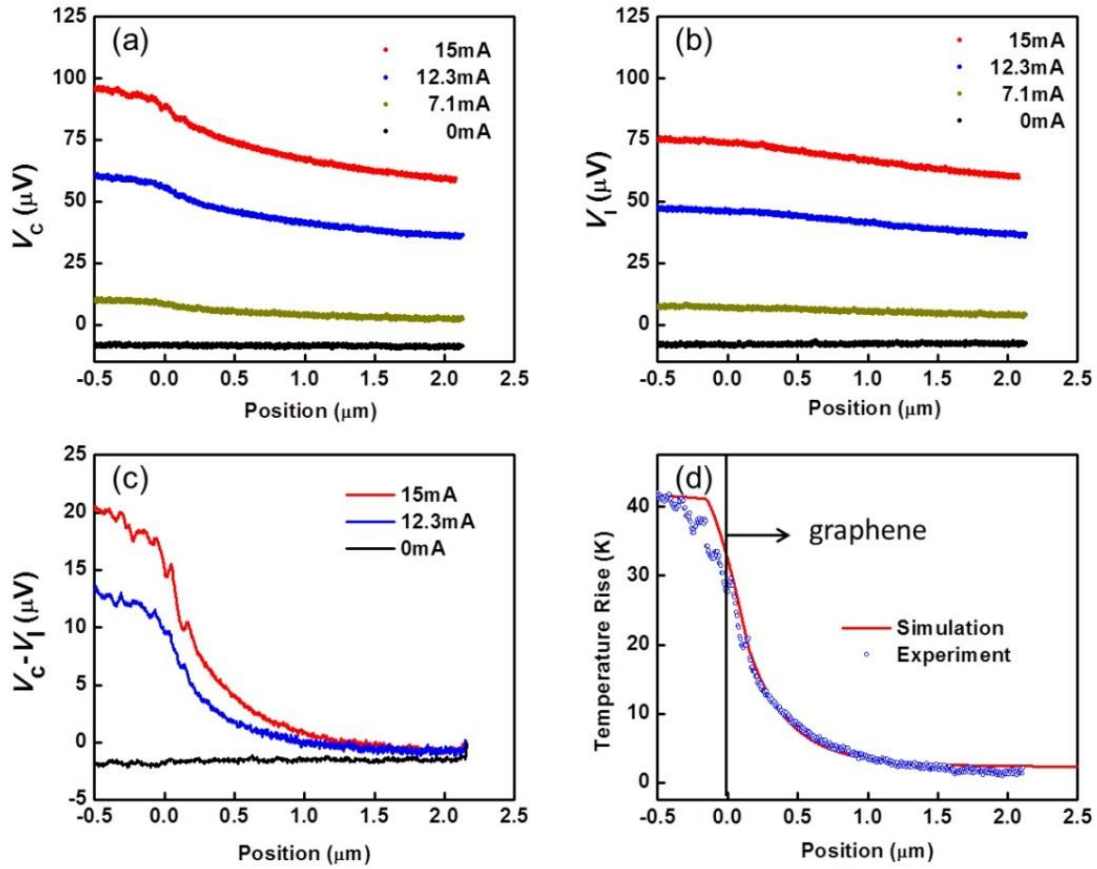


**Figure A. 2** (a) Contact-mode and (b) lift-mode thermovoltage profiles measured by the SThM probe scanned across the center of the metal heater line in the perpendicular direction at different heating currents indicated in the figure. (c) The difference between the contact-mode thermovoltage and lift-mode thermovoltage at different heating currents. (d) Calculated temperature profile across the heater line for a heating current of 15 mA. The thermovoltage difference between the contact mode and the lift mode is multiplied with a conversion factor of 1.9 K/ $\mu$ V and 1.5 K/ $\mu$ V to match the measurements on the metal line and graphene, respectively, to the calculated temperature profile. The metal line is located between 0 and -1  $\mu$ m. The graphene extends between 0 and 2.1  $\mu$ m.

## A.2 FINITE ELEMENT METHOD

Since the thermal contact resistance between the tip and the metal line and between the tip and graphene may be different, the temperature coefficient obtained from the metal line cannot be directly used for graphene. To this end, a finite element method (FEM) simulation was used to obtain the temperature distribution on the metal line as well as the graphene surface. In the model, the thermal conductivity of the heater line is obtained using the Wiedemann-Franz law based on the measured electrical resistivity of the heater line. The thermal conductivity values of SiO<sub>2</sub> and the supported graphene are taken to be 1.3 Wm<sup>-1</sup>K<sup>-1</sup> and 600 Wm<sup>-1</sup>K<sup>-1</sup>, respectively.<sup>2, 3</sup> The average calculated temperature of the metal line is made to match the measurement results using the resistance thermometry method by adjusting the interface resistance between the metal line and the SiO<sub>2</sub> surface, which is found to be  $1.0 \times 10^{-8} \text{ m}^2\text{KW}^{-1}$ . The value is consistent with the literature values for the metal-dielectric interface resistance and an order of magnitude larger than the interface resistance between SiO<sub>2</sub> and Si substrate.<sup>4-6</sup> We used interface resistance value of  $2.0 \times 10^{-8} \text{ m}^2\text{KW}^{-1}$  found at the Al-graphite interface for the metal-graphene interface resistance,<sup>7</sup> and  $1.0 \times 10^{-8} \text{ m}^2\text{KW}^{-1}$  for the interface resistance between the graphene and the SiO<sub>2</sub> film.<sup>8</sup> These two interface resistances affect the graphene temperature profile close to the metal line, and the temperature of the short metal line segment located on top of graphene, but has little effect on the average temperature of the long metal line.

The corrected ( $V_c - V_l$ ) value is then compared with the sample surface temperature profile obtained in a FEM simulation. The simulation box is  $6 \times 5.5 \times 5.3 \mu\text{m}^3$ , as shown in Fig. A.3 (a). The front surface of the simulation box is perpendicular to the metal heater line and passes through the center of the graphene, and is an adiabatic plane because of the symmetry between the two sides. The back surface is also perpendicular to the long heater line. Because it is sufficiently far away from the graphene compared to the  $\text{SiO}_2$  thickness, this surface is also assumed to be an adiabatic plane because of approximate symmetry between the two sides. The graphene flake is present on both sides of the metal heater line. Compared to the 300 nm  $\text{SiO}_2$  film thickness and the 1  $\mu\text{m}$  width of the heater line, the nearest metal electrode is sufficiently far away from the heater line so that it has little effect on the heat flow and temperature distribution near the heater line. Therefore, the left boundary plane, which passes through the centerline of the heater line, is assumed to be adiabatic because of the approximate left-right symmetry. In addition, the heat loss from the top surface through the air and via radiation is ignored. Because the dimension of the simulation box is much larger than the 300 nm thickness of the  $\text{SiO}_2$  film, the temperature rise at the two boundaries far away from the metal line, namely the bottom boundary and the right boundary, is much smaller than that near the heater line. Instead of assuming a zero temperature rise at the two boundaries, we estimate the small temperature rise there by simulating the two-dimensional (2D) temperature distribution in a  $50 \times 50 \mu\text{m}^2$  domain with the same heater line located at the top-left corner of the domain, as shown in Fig. A.3 (a). For the 2D simulation, the temperature rise at the right and bottom boundaries is taken to be zero, while the other

boundaries are adiabatic. The average temperature rise at a vertical line 5  $\mu\text{m}$  from the left boundary and that at a horizontal line 5  $\mu\text{m}$  below the top surface were determined, and used as the temperature rises at the left and bottom boundaries, respectively, of the 3D simulation domain with a  $6 \times 5.5 \times 5.3 \mu\text{m}^3$  size. Because of the small temperature rise at the two boundaries, this approximation imposes negligible error in the temperature profiles of the graphene flake and the metal line. In addition, very similar simulation result can be obtained when the size of the simulation box is reduced by a factor of 2 in each dimension, verifying that the approximation in the boundary conditions has little effect on the temperature in the regions of interest.

Figure A.2 (d) shows the calculated surface temperature profile perpendicular to and passing the center of the metal line for a heating current of 15 mA in the metal line. The ratio of the calculated surface temperature to the measured and corrected ( $V_C - V_I$ ) value was found to be 1.9 and 1.5 K/ $\mu\text{V}$  when the tip was on the heater line and graphene, respectively. For a lower heating current of 12.3 mA, the latter ratio was found to be 1.7 K/ $\mu\text{V}$ . Hence we have used the average value of  $1.6 \pm 0.1$  K/ $\mu\text{V}$  for this ratio measured on graphene. These calibration values are used to determine the temperature rise on the metal line and graphene when the sample was heated by a current flowing through the graphene. The calibration and measurement were conducted with the same contact pressure, lift height, and AFM laser position and power.

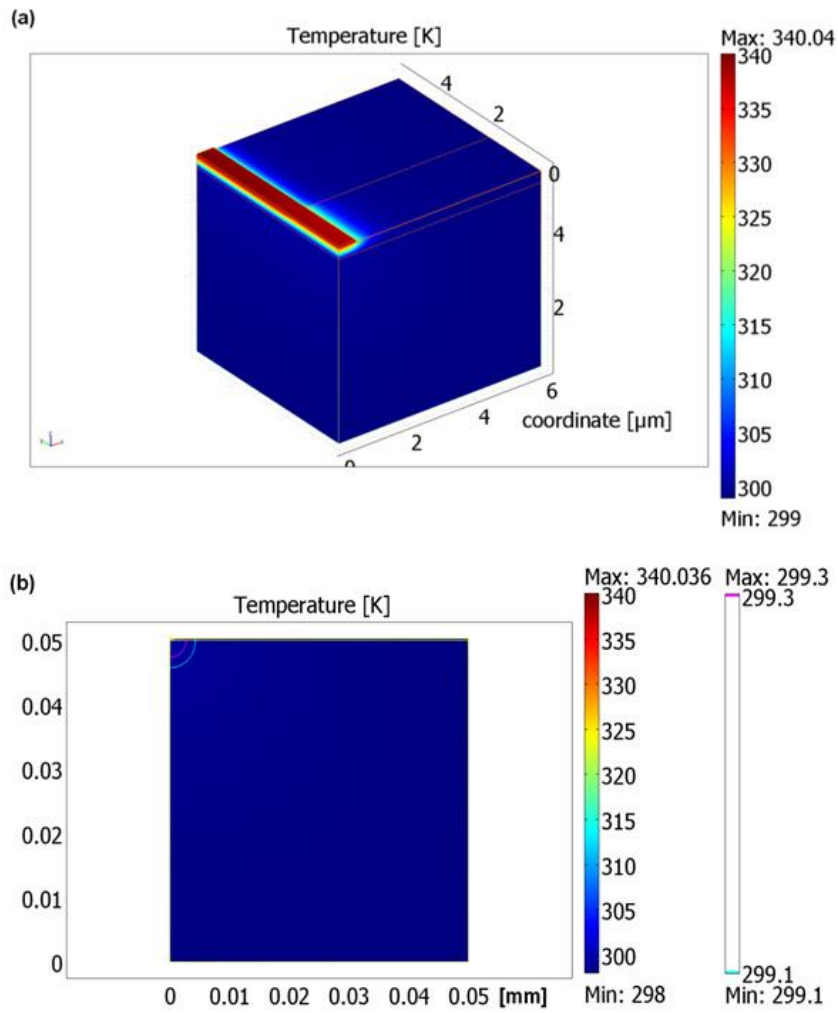


**Figure A. 3** FEM simulation results. (a) Temperature profile in a 3D domain of size  $6 \times 5.5 \times 5.3 \mu\text{m}^3$ . (b) Temperature profile in a 2D domain of size  $50 \times 50 \mu\text{m}^2$ . Two isotherms of 299.1 K and 299.3 K are shown as the pink and light blue curves.

## REFERENCES

1. Kim, K.; Chung, J.; Won, J.; Kwon, O.; Lee, J. S.; Park, S. H.; Choi, Y. K., *Appl Phys Lett* **2008**, *93*, 203115.
2. Cahill, D. G.; Bullen, A.; Lee, S. M., *High Temp-High Press* **2000**, *32*, 135-142.
3. Seol, J. H.; Jo, I.; Moore, A. L.; Lindsay, L.; Aitken, Z. H.; Pettes, M. T.; Li, X. S.; Yao, Z.; Huang, R.; Broido, D.; Mingo, N.; Ruoff, R. S.; Shi, L., *Science* **2010**, *328*, 213-216.
4. Kading, O. W.; Skurk, H.; Goodson, K. E., *Appl Phys Lett* **1994**, *65*, 1629-1631.
5. Kim, J. H.; Feldman, A.; Novotny, D., *J Appl Phys* **1999**, *86*, 3959-3963.
6. Yamane, T.; Nagai, N.; Katayama, S.; Todoki, M., *J Appl Phys* **2002**, *91*, 9772-9776.
7. Schmidt, A. J.; Chen, X. Y.; Chen, G., *Rev Sci Instrum* **2008**, *79*, 114902.
8. Chen, Z.; Jang, W.; Bao, W.; Lau, C. N.; Dames, C., *Appl Phys Lett* **2009**, *95*, 161910.

## Appendix B. Gate Stress Effect

Figure B.1 shows repeated  $R$  vs.  $V_g$  measurements on another device which exhibit the so-called bias stress effect. In Fig. B.1 (a), each  $R$  vs.  $V_g$  curve was obtained at low excitation current ( $\sim 5 \mu\text{A}$ ) using a lock-in amplifier, and  $V_g$  was swept from  $-50 \text{ V}$  to  $50 \text{ V}$  with a speed of  $5 \text{ Vs}^{-1}$  (forward sweep). The blue curve was recorded after 1 sec of holding time at  $V_g = -50 \text{ V}$ , and the red curve was recorded after 5000 seconds of holding time, while the black curves in between were obtained after 100, 500, 1000 seconds (right to left), respectively. The Dirac point measured with the forward sweep changed from  $22 \text{ V}$  at 1 sec holding time to  $8.5 \text{ V}$  at 5000 seconds of holding time. In Fig. B.1 (b), the  $R$  vs.  $V_g$  curves were obtained by changing  $V_g$  from  $50 \text{ V}$  to  $-50 \text{ V}$  (reverse sweep) after a certain period of holding time at  $V_g = 50 \text{ V}$ . The position of the Dirac point was observed to shift from  $17 \text{ V}$  after 1 second to  $40 \text{ V}$  after 5000 seconds of holding time. This gate-induced bias stress effect is attributed to impurity charges on the sample surface, dipolar adsorbates such as water molecules, or mobile/immobile charges at the graphene/ $\text{SiO}_2$  interface.<sup>1</sup> When a negative gate voltage ( $-50 \text{ V}$ ) was applied for a long time, positive charges were introduced to the vicinity of the channel, and acted as a local positively biased gate. As a result, the Fermi level of the graphene was increased as shown in Fig. B.1 (a). On the other hand, positive gate bias of  $50 \text{ V}$  gradually lowered the Fermi level because of the introduction of negative charges, as shown in Fig. B.1 (b).

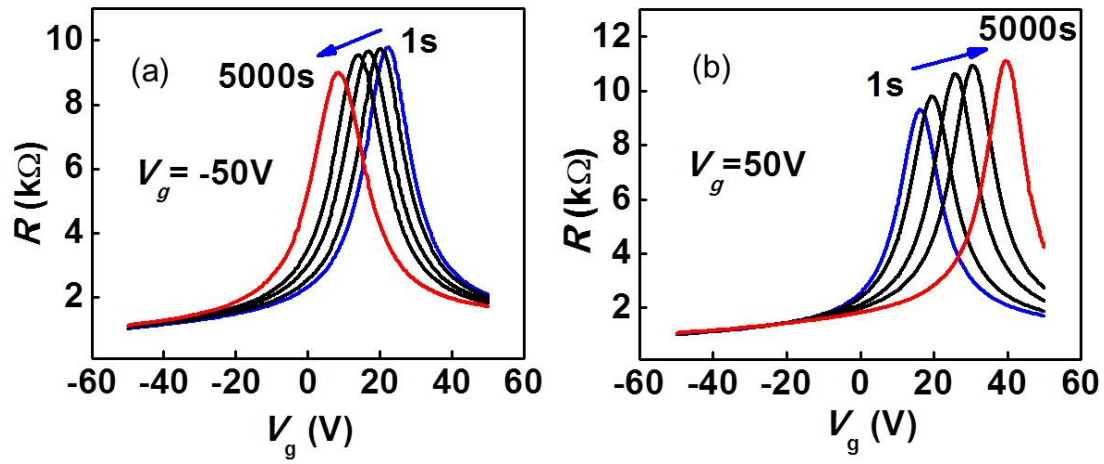


**Figure B. 1** (a)  $R$  vs.  $V_g$  measured at different times after  $V_g = -50V$  was applied to the back gate. (b)  $R$  vs.  $V_g$  measured at different times after  $V_g = 50V$  was applied to the back gate.

## Appendix C. Thermal Conductivity Modeling

In Eq. (4.13), both  $v_p$  and  $D_p(\omega)$  is obtained from the phonon dispersion and the scattering time  $\tau_p$  is calculated for isotope, boundary scattering. Total of 6 low frequency phonon modes are considered and their dispersion relations shown in Fig. C.1 are used. Similar to graphite, the interlayer coupling in multi-layer h-BN introduced the splitting of the low frequency phonon modes near the  $\Gamma$  point. The calculation was performed between  $\Gamma$  and M symmetric points and the thickness of  $2\delta$  was used for few-layer h-BN.

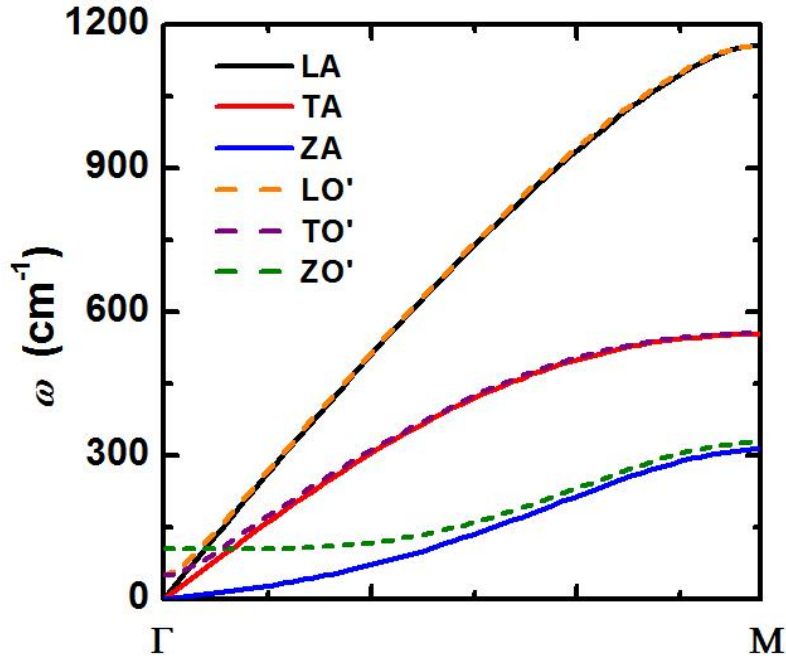


**Figure C. 1** Phonon dispersion of bulk h-BN along the high symmetric direction connecting between  $\Gamma$  and M.

Three types of phonon scattering mechanisms are considered in the calculation. The synthesized h-BN consists of 19.9%  $^{10}\text{B}$  and 80.1%  $^{11}\text{B}$ , whereas the isotopic variance of N is negligible. Phonon scattering by isotopic impurities is calculated as<sup>1</sup>

$$\tau_{D,p}^{-1} = \frac{S_0 \Gamma}{4} \frac{k_p}{v_p} \omega_p^2 \quad (C1)$$

where  $S_0$  is the cross-sectional area per atom and  $\Gamma$  is the strength of the point defect scattering, which is obtained as  $\Gamma = \sum_i f_i (1 - M_i / \bar{M})^2 = 0.00136$ ,<sup>2</sup> where  $f_i$  is the fractional concentration of the impurity atoms,  $M_i$  is the mass of the impurity, and  $\bar{M}$  is the average atomic mass of boron.

Phonon scattering by other point defects such as vacancies and impurities are also calculated from Eq. (C1). The phonon scattering rate by the lateral edges of the few-layer h-BN sample is calculated as  $\tau_{B,p}^{-1} = v_p / l_b$ , where  $l_b$  is the boundary scattering mean free path. Matthiessen's rule was used to account for the combined effects of different scattering mechanisms.

Figure C.2 shows the calculation results for different  $l_b$  values and different point defect concentrations. The calculation does not account for phonon scattering by polymer residues and Umklapp scattering, the latter of which is expected to be negligible at the low temperature limit. Because of the high isotopic impurity concentration, the calculation shows that isotope impurity scattering dominates over scattering by point vacancies at a concentration as high as  $10^{20} \text{ cm}^{-3}$ . An  $l_b$  value of 2  $\mu\text{m}$  can be used to fit the low-temperature experimental thermal conductivity values for bulk h-BN.<sup>2</sup> In comparison, without accounting for scattering by polymer residues, the  $l_b$  value needs to be as small as 550 nm and 180 nm in order to match the experimental thermal conductivity data for the 11-layer and 5-layer sample, respectively. These  $l_b$  values are

much smaller than the smallest geometrical boundary length of 3  $\mu\text{m}$  of the single crystalline few-layer h-BN flakes.

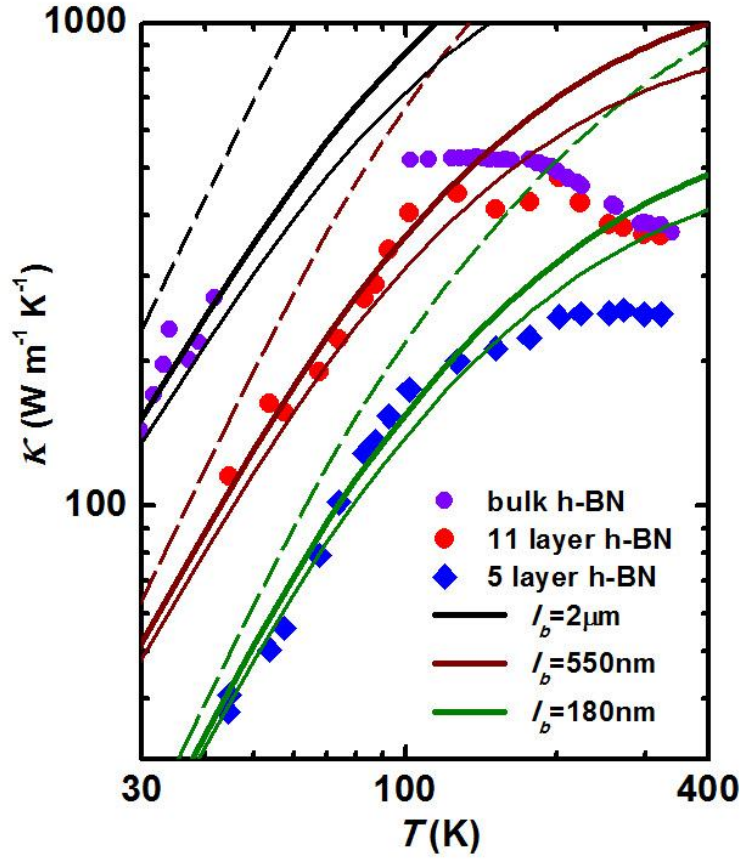


**Figure C. 2** Comparison between the experimental thermal conductivity and calculation results for different  $l_b$  values with no isotope impurities or point vacancies (thin dashed curves), with 19.9%  $^{10}\text{B}$  and 80.1%  $^{11}\text{B}$  and no point vacancies (thick solid curves), and with 19.9%  $^{10}\text{B}$  and 80.1%  $^{11}\text{B}$  and point vacancy concentration  $n_D = 10^{20} \text{ cm}^{-3}$  (thin solid curves). Phonon scattering by polymer residues and Umklapp scattering are not included in the calculation.

## REFERENCES

1. Nika, D. L.; Pokatilov, E. P.; Askerov, A. S.; Balandin, A. A., *Phys Rev B* **2009**, *79*, 155413.
2. Lindsay, L.; Broido, D. A., *Phys Rev B* **2011**, *84*, 155421.

## Appendix D. Thermal Contact Conductance

We have evaluated the thermal interface conductance between the h-BN sample and the micro-bridge device using two different models. In the first one, the lateral temperature distribution at the contact area is ignored, and the thermal interface conductance is calculated as

$$g_i = 1/(R_c A_c) \quad (\text{D1})$$

where  $R_c$  and  $A_c$  are the measured contact thermal resistance and contact area. In the second model, the lateral temperature distribution at the contact area is treated by a fin heat transfer model to obtain the contact thermal resistance according to<sup>1,2</sup>

$$R_c^{-1} = \sqrt{\kappa_s A w g_i} \tanh\left(L_c \sqrt{\frac{g_i}{\kappa_s t}}\right) \quad (\text{D2})$$

where  $\kappa_s$  is the thermal conductivity of the supported few-layer h-BN,  $g_i$  is the thermal interface conductance per unit area, and  $A$  and  $w$  are the cross section and width of the few-layer h-BN sample. Because of the additional phonon scattering by the interface between the h-BN and the micro-device, the thermal conductivity of the supported h-BN can be lower than that for the suspended h-BN, as shown by recent measurements in supported graphene<sup>3,4</sup> and encased graphene.<sup>5</sup> Nevertheless, the difference is expected to decrease with increasing thickness. For the 11-layer h-BN sample where the thermal conductivity of the suspended region approaches that for bulk h-BN, we assume that  $\kappa_s$  is the same as the thermal conductivity obtained for the suspended segment and use the obtained  $R_c$  and Eq. (D2) to determine the interface conductance  $g_i$ . The result is shown

in Fig. D.1, and is about 1–2 orders of magnitude lower than that measured for supported few-layer graphene.<sup>6</sup> The low  $g_i$  value for the h-BN sample can be caused by the assumption of the same thermal conductivity for the suspended and supported regions of the h-BN, and more likely caused by organic contamination left at the interface during the transfer process as well as the surface roughness of the micro-bridge device.

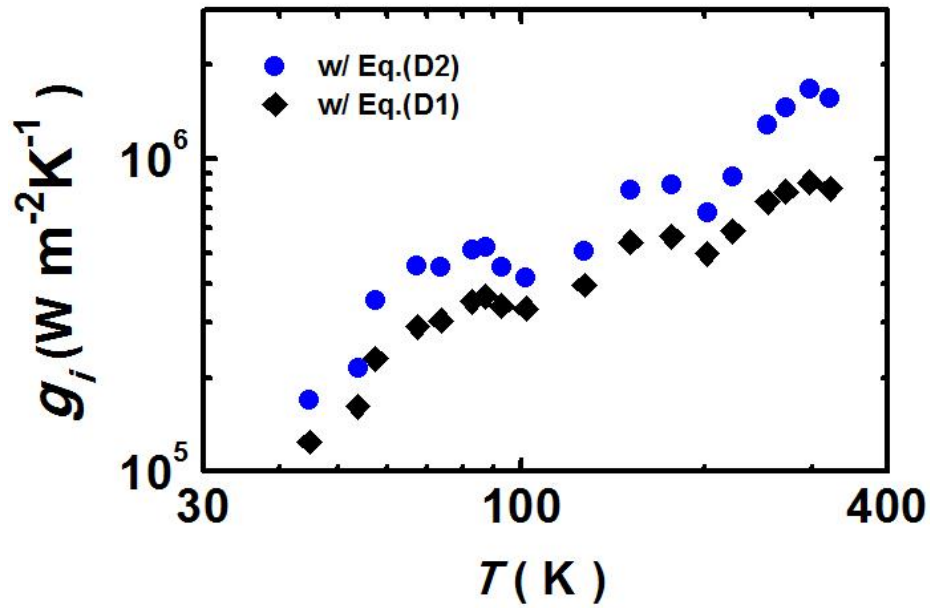


**Figure D. 1** The obtained thermal interface conductance between the h-BN sample and the micro-bridge device based on the fin model (blue circle) and without using fin model (black diamond).

## REFERENCES

1. Pettes, M. T.; Shi, L., *Adv Funct Mater* **2009**, *19*, 3918-3925.
2. Yu, C. H.; Saha, S.; Zhou, J. H.; Shi, L.; Cassell, A. M.; Cruden, B. A.; Ngo, Q.; Li, J., *J Heat Trans-T Asme* **2006**, *128*, 234-239.
3. Cai, W. W.; Moore, A. L.; Zhu, Y. W.; Li, X. S.; Chen, S. S.; Shi, L.; Ruoff, R. S., *Nano Lett* **2010**, *10*, 1645-1651.
4. Seol, J. H.; Jo, I.; Moore, A. L.; Lindsay, L.; Aitken, Z. H.; Pettes, M. T.; Li, X. S.; Yao, Z.; Huang, R.; Broido, D.; Mingo, N.; Ruoff, R. S.; Shi, L., *Science* **2010**, *328*, 213-216.
5. Jang, W. Y.; Chen, Z.; Bao, W. Z.; Lau, C. N.; Dames, C., *Nano Lett* **2010**, *10*, 3909-3913.
6. Mak, K. F.; Lui, C. H.; Heinz, T. F., *Appl Phys Lett* **2010**, *97*, 221904.

## Bibliography

Note: Each chapter has a reference section at the end. In this bibliography, reference materials are sorted in alphabetical order of the first author.

Alem, N.; Erni, R.; Kisielowski, C.; Rossell, M. D.; Gannett, W.; Zettl, A., *Phys Rev B* **2009**, *80*, 155425.

Asheghi, M.; Kurabayashi, K.; Kasnavi, R.; Goodson, K. E., *J Appl Phys* **2002**, *91*, 5079-5088.

Avouris, P., *Nano Lett* **2010**, *10*, 4285-4294.

Bae, M. H.; Ong, Z. Y.; Estrada, D.; Pop, E., *Nano Lett* **2010**, *10*, 4787-4793.

Balandin, A. A.; Ghosh, S.; Bao, W. Z.; Calizo, I.; Teweldebrhan, D.; Miao, F.; Lau, C. N., *Nano Lett* **2008**, *8*, 902-907.

Balandin, A. A., *Nat Mater* **2011**, *10*, 569-581.

Basko, D. M.; Piscanec, S.; Ferrari, A. C., *Phys Rev B* **2009**, *80*, 165413.

Benedict, L. X.; Louie, S. G.; Cohen, M. L., *Solid State Commun* **1996**, *100*, 177-180.

Berciaud, S.; Han, M. Y.; Mak, K. F.; Brus, L. E.; Kim, P.; Heinz, T. F., *Phys Rev Lett* **2010**, *104*, 227401. Wallace, P. R., *Phys Rev* **1947**, *71*, 476-476.

Berciaud, S.; Ryu, S.; Brus, L. E.; Heinz, T. F., *Nano Lett* **2009**, *9*, 346-352.

Bolotin, K. I.; Sikes, K. J.; Jiang, Z.; Klima, M.; Fudenberg, G.; Hone, J.; Kim, P.; Stormer, H. L., *Solid State Commun* **2008**, *146*, 351-355.

Bonini, N.; Lazzeri, M.; Marzari, N.; Mauri, F., *Phys Rev Lett* **2007**, *99*, 176802.

Cahill, D. G.; Bullen, A.; Lee, S. M., *High Temp-High Press* **2000**, *32*, 135-142.

Cai, W. W.; Moore, A. L.; Zhu, Y. W.; Li, X. S.; Chen, S. S.; Shi, L.; Ruoff, R. S., *Nano Lett* **2010**, *10*, 1645-1651.

Calizo, I.; Balandin, A. A.; Bao, W.; Miao, F.; Lau, C. N., *Nano Lett* **2007**, *7*, 2645-2649.

Calizo, I.; Miao, F.; Bao, W.; Lau, C. N.; Balandin, A. A., *Appl Phys Lett* **2007**, *91*, 071913.

Cancado, L. G.; Jorio, A.; Ferreira, E. H. M.; Stavale, F.; Achete, C. A.; Capaz, R. B.; Moutinho, M. V. O.; Lombardo, A.; Kulmala, T. S.; Ferrari, A. C., *Nano Lett* **2011**, *11*, 3190-3196.

Casiraghi, C.; Hartschuh, A.; Qian, H.; Piscanec, S.; Georgi, C.; Fasoli, A.; Novoselov, K. S.; Basko, D. M.; Ferrari, A. C., *Nano Lett* **2009**, *9*, 1433-1441.

Castro Neto, A. H.; Guinea, F.; Peres, N. M. R.; Novoselov, K. S.; Geim, A. K., *Rev Mod Phys* **2009**, *81*, 109-162.

Catellani, A.; Posternak, M.; Baldereschi, A.; Freeman, A. J., *Phys Rev B* **1987**, *36*, 6105-6111.

Chae, D. H.; Krauss, B.; von Klitzing, K.; Smet, J. H., *Nano Lett* **2010**, *10*, 466-471.

Chang, C. W.; Fennimore, A. M.; Afanasiev, A.; Okawa, D.; Ikuno, T.; Garcia, H.; Li, D. Y.; Majumdar, A.; Zettl, A., *Phys Rev Lett* **2006**, *97*, 085901.

Chen, C. Y.; Rosenblatt, S.; Bolotin, K. I.; Kalb, W.; Kim, P.; Kymissis, I.; Stormer, H. L.; Heinz, T. F.; Hone, J., *Nat Nanotechnol* **2009**, *4*, 861-867.

Chen, J. H.; Jang, C.; Xiao, S. D.; Ishigami, M.; Fuhrer, M. S., *Nat Nanotechnol* **2008**, *3*, 206-209.

Chen, S. S.; Wu, Q. Z.; Mishra, C.; Kang, J. Y.; Zhang, H. J.; Cho, K. J.; Cai, W. W.; Balandin, A. A.; Ruoff, R. S., *Nat Mater* **2012**, *11*, 203-207.

Chen, Z.; Jang, W.; Bao, W.; Lau, C. N.; Dames, C., *Appl Phys Lett* **2009**, *95*, 161910.

Chien, S. K.; Yang, Y. T.; Chen, C. K., *Appl Phys Lett* **2011**, *98*, 033107.

Connolly, M. R.; Chiou, K. L.; Smith, C. G.; Anderson, D.; Jones, G. A. C.; Lombardo, A.; Fasoli, A.; Ferrari, A. C., *Appl Phys Lett* **2010**, *96*, 113501.

Das, A.; Pisana, S.; Chakraborty, B.; Piscanec, S.; Saha, S. K.; Waghmare, U. V.; Novoselov, K. S.; Krishnamurthy, H. R.; Geim, A. K.; Ferrari, A. C.; Sood, A. K., *Nat Nanotechnol* **2008**, *3*, 210-215.

Das Sarma, S.; Adam, S.; Hwang, E. H.; Rossi, E., *Rev Mod Phys* **2011**, *83*, 407-470.

Dean, C. R.; Young, A. F.; Meric, I.; Lee, C.; Wang, L.; Sorgenfrei, S.; Watanabe, K.; Taniguchi, T.; Kim, P.; Shepard, K. L.; Hone, J., *Nat Nanotechnol* **2010**, *5*, 722-726.

Faugeras, C.; Faugeras, B.; Orlita, M.; Potemski, M.; Nair, R. R.; Geim, A. K., *Acs Nano* **2010**, *4*, 1889-1892.

Ferrari, A. C.; Meyer, J. C.; Scardaci, V.; Casiraghi, C.; Lazzeri, M.; Mauri, F.; Piscanec, S.; Jiang, D.; Novoselov, K. S.; Roth, S.; Geim, A. K., *Phys Rev Lett* **2006**, *97*, 187401.

Freitag, M.; Chiu, H. Y.; Steiner, M.; Perebeinos, V.; Avouris, P., *Nat Nanotechnol* **2010**, *5*, 497-501.

Freitag, M.; Steiner, M.; Martin, Y.; Perebeinos, V.; Chen, Z. H.; Tsang, J. C.; Avouris, P., *Nano Lett* **2009**, *9*, 1883-1888.

Geick, R.; Perry, C. H.; Rupprecht, G., *Phys Rev* **1966**, *146*, 543.

Giannozzi, P.; Baroni, S.; Bonini, N.; Calandra, M.; Car, R.; Cavazzoni, C.; Ceresoli, D.; Chiarotti, G. L.; Cococcioni, M.; Dabo, I.; Dal Corso, A.; de Gironcoli, S.; Fabris, S.; Fratesi, G.; Gebauer, R.; Gerstmann, U.; Gougoussis, C.; Kokalj, A.; Lazzeri, M.; Martin-Samos, L.; Marzari, N.; Mauri, F.; Mazzarello, R.; Paolini, S.; Pasquarello, A.; Paulatto, L.; Sbraccia, C.; Scandolo, S.; Sclauzero, G.; Seitsonen, A. P.; Smogunov, A.; Umari, P.; Wentzcovitch, R. M., *J Phys-Condens Mat* **2009**, *21*, 395502.

Goossens, A. M.; Calado, V. E.; Barreiro, A.; Watanabe, K.; Taniguchi, T.; Vandersypen, L. M. K., *Appl Phys Lett* **2012**, *100*, 073110.

Graf, D.; Molitor, F.; Ensslin, K.; Stampfer, C.; Jungen, A.; Hierold, C.; Wirtz, L., *Nano Lett* **2007**, *7*, 238-242.

Han, W. Q.; Wu, L. J.; Zhu, Y. M.; Watanabe, K.; Taniguchi, T., *Appl Phys Lett* **2008**, *93*, 223103.

Hone, J., *Top Appl Phys* **2001**, *80*, 273-286.

Huang, P. Y.; Ruiz-Vargas, C. S.; van der Zande, A. M.; Whitney, W. S.; Levendorf, M. P.; Kevek, J. W.; Garg, S.; Alden, J. S.; Hustedt, C. J.; Zhu, Y.; Park, J.; McEuen, P. L.; Muller, D. A., *Nature* **2011**, *469*, 389.

Ishigami, M.; Chen, J. H.; Cullen, W. G.; Fuhrer, M. S.; Williams, E. D., *Nano Lett* **2007**, *7*, 1643-1648.

Jalilian, R.; Jauregui, L. A.; Lopez, G.; Tian, J. F.; Roecker, C.; Yazdanpanah, M. M.; Cohn, R. W.; Jovanovic, I.; Chen, Y. P., *Nanotechnology* **2011**, *22*, 295705.

Jang, W. Y.; Chen, Z.; Bao, W. Z.; Lau, C. N.; Dames, C., *Nano Lett* **2010**, *10*, 3909-3913.

Jo, I.; Hsu, I. K.; Lee, Y. J.; Sadeghi, M. M.; Kim, S.; Cronin, S.; Tutuc, E.; Banerjee, S. K.; Yao, Z.; Shi, L., *Nano Lett* **2011**, *11*, 85-90.

Jorio, A.; Pimenta, M. A.; Souza, A. G.; Saito, R.; Dresselhaus, G.; Dresselhaus, M. S., *New J Phys* **2003**, *5*, 139.

Kading, O. W.; Skurk, H.; Goodson, K. E., *Appl Phys Lett* **1994**, *65*, 1629-1631.

Kim, J. H.; Feldman, A.; Novotny, D., *J Appl Phys* **1999**, *86*, 3959-3963.

Kim, J. Y.; Lee, J.-H.; Grossman, J. C., *Acs Nano* **2012**, *6*, 9050-9057.

Kim, K.; Jeong, W. H.; Lee, W. C.; Reddy, P., *Acs Nano* **2012**, *6*, 4248-4257

Kim, K. S.; Zhao, Y.; Jang, H.; Lee, S. Y.; Kim, J. M.; Kim, K. S.; Ahn, J. H.; Kim, P.; Choi, J. Y.; Hong, B. H., *Nature* **2009**, *457*, 706-710.

Kim, S.; Jo, I.; Nah, J.; Yao, Z.; Banerjee, S. K.; Tutuc, E., *Phys Rev B* **2011**, *83*, 161401.

Kim, S.; Nah, J.; Jo, I.; Shahrjerdi, D.; Colombo, L.; Yao, Z.; Tutuc, E.; Banerjee, S. K., *Appl Phys Lett* **2009**, *94*, 062107.

Klein, C. A.; Holland, M. G., *Phys Rev a-Gen Phys* **1964**, *136*, A575.

Koh, Y. K.; Bae, M. H.; Cahill, D. G.; Pop, E., *Acs Nano* **2011**, *5*, 269-274.

Koh, Y. K.; Bae, M. H.; Cahill, D. G.; Pop, E., *Nano Lett* **2010**, *10*, 4363-4368.

Kudin, K. N.; Ozbas, B.; Schniepp, H. C.; Prud'homme, R. K.; Aksay, I. A.; Car, R., *Nano Lett* **2008**, *8*, 36-41.

Lafkioti, M.; Krauss, B.; Lohmann, T.; Zschieschang, U.; Klauk, H.; von Klitzing, K.; Smet, J. H., *Nano Lett* **2010**, *10*, 1149-1153.

Lee, C.; Wei, X. D.; Kysar, J. W.; Hone, J., *Science* **2008**, *321*, 385-388.

Li, X. S.; Cai, W. W.; An, J. H.; Kim, S.; Nah, J.; Yang, D. X.; Piner, R.; Velamakanni, A.; Jung, I.; Tutuc, E.; Banerjee, S. K.; Colombo, L.; Ruoff, R. S., *Science* **2009**, *324*, 1312-1314.

Liang, X. L.; Sperling, B. A.; Calizo, I.; Cheng, G. J.; Hacker, C. A.; Zhang, Q.; Obeng, Y.; Yan, K.; Peng, H. L.; Li, Q. L.; Zhu, X. X.; Yuan, H.; Walker, A. R. H.; Liu, Z. F.; Peng, L. M.; Richter, C. A., *Acs Nano* **2011**, *5*, 9144-9153.

Lin, Y. C.; Jin, C. H.; Lee, J. C.; Jen, S. F.; Suenaga, K.; Chiu, P. W., *Acs Nano* **2011**, *5*, 2362-2368.

Lin, Y. C.; Lu, C. C.; Yeh, C. H.; Jin, C. H.; Suenaga, K.; Chiu, P. W., *Nano Lett* **2012**, *12*, 414-419.

Lin, Y. M.; Dimitrakopoulos, C.; Jenkins, K. A.; Farmer, D. B.; Chiu, H. Y.; Grill, A.; Avouris, P., *Science* **2010**, *327*, 662-662.

Lindsay, L.; Broido, D. A.; Mingo, N., *Phys Rev B* **2010**, *82*, 115427.

Lindsay, L.; Broido, D. A., *Phys Rev B* **2011**, *84*, 155421.

Lock, E. H.; Baraket, M.; Laskoski, M.; Mulvaney, S. P.; Lee, W. K.; Sheehan, P. E.; Hines, D. R.; Robinson, J. T.; Tosado, J.; Fuhrer, M. S.; Hernandez, S. C.; Waltont, S. G., *Nano Lett* **2012**, *12*, 102-107.

Lucchese, M. M.; Stavale, F.; Ferreira, E. H. M.; Vilani, C.; Moutinho, M. V. O.; Capaz, R. B.; Achete, C. A.; Jorio, A., *Carbon* **2010**, *48*, 1592-1597.

Lui, C. H.; Li, Z. Q.; Chen, Z. Y.; Klimov, P. V.; Brus, L. E.; Heinz, T. F., *Nano Lett* **2011**, *11*, 164-169.

Luryi, S., *Appl Phys Lett* **1988**, *52*, 501-503.

Mak, K. F.; He, K. L.; Shan, J.; Heinz, T. F., *Nat Nanotechnol* **2012**, *7*, 494-498.

Mak, K. F.; Lui, C. H.; Heinz, T. F., *Appl Phys Lett* **2010**, *97*, 221904.

Malard, L. M.; Pimenta, M. A.; Dresselhaus, G.; Dresselhaus, M. S., *Phys Rep* **2009**, *473*, 51-87.

Martin, J.; Akerman, N.; Ulbricht, G.; Lohmann, T.; Smet, J. H.; Von Klitzing, K.; Yacoby, A., *Nat Phys* **2008**, *4*, 144-148.

Maultzsch, J.; Reich, S.; Thomsen, C.; Requardt, H.; Ordejon, P., *Phys Rev Lett* **2004**, *92*, 075501

Meric, I.; Han, M. Y.; Young, A. F.; Ozyilmaz, B.; Kim, P.; Shepard, K. L., *Nat Nanotechnol* **2008**, *3*, 654-659.

Meric, I.; Dean, C. R.; Young, A. F.; Baklitskaya, N.; Tremblay, N. J.; Nuckolls, C.; Kim, P.; Shepard, K. L., *Nano Lett* **2011**, *11*, 1093-1097.

Meyer, J. C.; Geim, A. K.; Katsnelson, M. I.; Novoselov, K. S.; Booth, T. J.; Roth, S., *Nature* **2007**, *446*, 60-63.

Mohr, M.; Maultzsch, J.; Dobardzic, E.; Reich, S.; Milosevic, I.; Damnjanovic, M.; Bosak, A.; Krisch, M.; Thomsen, C., *Phys Rev B* **2007**, *76*, 035439.

Nam, S. G.; Ki, D. K.; Lee, H. J., *Phys Rev B* **2010**, *82*, 245416.

Nemanich, R. J.; Solin, S. A.; Martin, R. M., *Phys Rev B* **1981**, *23*, 6348-6356.

Ni, Z. H.; Yu, T.; Lu, Y. H.; Wang, Y. Y.; Feng, Y. P.; Shen, Z. X., *Acs Nano* **2008**, *2*, 2301-2305.

Ni, Z. H.; Wang, H. M.; Luo, Z. Q.; Wang, Y. Y.; Yu, T.; Wu, Y. H.; Shen, Z. X., *J Raman Spectrosc* **2010**, *41*, 479-483.

Nika, D. L.; Pokatilov, E. P.; Askerov, A. S.; Balandin, A. A., *Phys Rev B* **2009**, *79*, 155413.

Novoselov, K. S.; Geim, A. K.; Morozov, S. V.; Jiang, D.; Zhang, Y.; Dubonos, S. V.; Grigorieva, I. V.; Firsov, A. A., *Science* **2004**, *306*, 666-669.

Novoselov, K. S.; Geim, A. K.; Morozov, S. V.; Jiang, D.; Katsnelson, M. I.; Grigorieva, I. V.; Dubonos, S. V.; Firsov, A. A., *Nature* **2005**, *438*, 197-200.

Oshima, C.; Aizawa, T.; Souda, R.; Ishizawa, Y.; Sumiyoshi, Y., *Solid State Commun* **1988**, *65*, 1601-1604.

Park, J. S.; Reina, A.; Saito, R.; Kong, J.; Dresselhaus, G.; Dresselhaus, M. S., *Carbon* **2009**, *47*, 1303-1310.

Park, H. J.; Meyer, J.; Roth, S.; Skakalova, V., *Carbon* **2010**, *48*, 1088-1094.

Pettes, M. T.; Jo, I. S.; Yao, Z.; Shi, L., *Nano Lett* **2011**, *11*, 1195-1200.

Pettes, M. T.; Shi, L., *Adv Funct Mater* **2009**, *19*, 3918-3925.

Popov, V. N., *Phys Rev B* **2002**, *66*, 153408.

Prasher, R., *Appl Phys Lett* **2009**, *94*, 041905

Qin, S. Y.; Kim, J.; Niu, Q.; Shih, C. K., *Science* **2009**, *324*, 1314-1317.

Rao, A. M.; Eklund, P. C.; Bandow, S.; Thess, A.; Smalley, R. E., *Nature* **1997**, *388*, 257-259.

Reich, S.; Ferrari, A. C.; Arenal, R.; Loiseau, A.; Bello, I.; Robertson, J., *Phys Rev B* **2005**, *71*, 205201.

Robertson, J., *Phys Rev B* **1984**, *29*, 2131-2137.

Ryu, S.; Liu, L.; Berciaud, S.; Yu, Y. J.; Liu, H. T.; Kim, P.; Flynn, G. W.; Brus, L. E., *Nano Lett* **2010**, *10*, 4944-4951.

Sadeghi, M. M.; Pettes, M. T.; Shi, L., *Solid State Commun* **2012**, *152*, 1321-1330.

Schmidt, A. J.; Chen, X. Y.; Chen, G., *Rev Sci Instrum* **2008**, *79*, 114902.

Seol, J. H.; Jo, I.; Moore, A. L.; Lindsay, L.; Aitken, Z. H.; Pettes, M. T.; Li, X. S.; Yao, Z.; Huang, R.; Broido, D.; Mingo, N.; Ruoff, R. S.; Shi, L., *Science* **2010**, *328*, 213-216.

Seol, J. H.; Moore, A. L.; Shi, L.; Jo, I.; Yao, Z., *J Heat Trans-T Asme* **2011**, *133*, 022403.

Serrano, J.; Bosak, A.; Arenal, R.; Krisch, M.; Watanabe, K.; Taniguchi, T.; Kanda, H.; Rubio, A.; Wirtz, L., *Phys Rev Lett* **2007**, *98*, 095503.

Shi, L.; Majumdar, A., *J Heat Trans-T Asme* **2002**, *124*, 329-337.

Shi, L.; Zhou, J. H.; Kim, P.; Bachtold, A.; Majumdar, A.; McEuen, P. L., *J Appl Phys* **2009**, *105*, 104306.

Sichel, E. K.; Miller, R. E.; Abrahams, M. S.; Buiocchi, C. J., *Phys Rev B* **1976**, *13*, 4607-4611.

Simpson, A.; Stuckes, A. D., *J Phys Part C Solid* **1971**, *4*, 1710.

Slack, G. A., *Phys Rev* **1962**, *127*, 694.

Touloukian, Y. S.; Powell, R. W.; Ho, C. Y.; Klemens, P. G., *New York, IFI/Plenum* **1970**.

Wallace, P. R., *Phys Rev* **1947**, *71*, 476-476.

Wang, F.; Zhang, Y. B.; Tian, C. S.; Girit, C.; Zettl, A.; Crommie, M.; Shen, Y. R., *Science* **2008**, *320*, 206-209.

Watanabe, K.; Taniguchi, T.; Kanda, H., *Nat Mater* **2004**, *3*, 404-409.

Wei, L. H.; Kuo, P. K.; Thomas, R. L.; Anthony, T. R.; Banholzer, W. F., *Phys Rev Lett* **1993**, *70*, 3764-3767.

Xia, Y.; Qian, D.; Hsieh, D.; Wray, L.; Pal, A.; Lin, H.; Bansil, A.; Grauer, D.; Hor, Y. S.; Cava, R. J.; Hasan, M. Z., *Nat Phys* **2009**, *5*, 398-402.

Yamane, T.; Nagai, N.; Katayama, S.; Todoki, M., *J Appl Phys* **2002**, *91*, 9772-9776.

Yao, Z.; Kane, C. L.; Dekker, C., *Phys Rev Lett* **2000**, *84*, 2941-2944.

Yu, C. H.; Saha, S.; Zhou, J. H.; Shi, L.; Cassell, A. M.; Cruden, B. A.; Ngo, Q.; Li, J., *J Heat Trans-T Asme* **2006**, *128*, 234-239.

Zhang, Y. B.; Tan, Y. W.; Stormer, H. L.; Kim, P., *Nature* **2005**, *438*, 201-204.

Zhang, H. J.; Liu, C. X.; Qi, X. L.; Dai, X.; Fang, Z.; Zhang, S. C., *Nat Phys* **2009**, *5*, 438-442.

Zhi, C. Y.; Bando, Y.; Tang, C. C.; Kuwahara, H.; Golberg, D., *Adv Mater* **2009**, *21*, 2889.

Zilker, S. J.; Detcherry, C.; Cantatore, E.; de Leeuw, D. M., *Appl Phys Lett* **2001**, *79*, 1124-1126.